Coulomb Excitation of ^{66}Ge

UNIVERSITY *of the*
WESTERN CAPE

by

Kenzo Abrahams

A thesis submitted in conformity with the requirements for the
degree of Doctor of Philosophy

in the
Faculty of Science
Department of Physics

Supervisor: Prof. Nico Orce

April 2021

Declaration

I, Kenzo Abrahams, declare that this thesis "Coulomb Excitation of ^{66}Ge" is my own work, that it has not been submitted before for any degree or assessment at any other university, and that all the sources I have used or quoted have been indicated and acknowledged by means of complete references.

Signature:.......................... Date: 31 January 2021

"The distance between insanity and genius is measured only by success.'"

Bruce Feirstein

Abstract

The Coulomb excitation of ^{66}Ge has been performed for the first time using "safe" bombarding energies at the HIE-ISOLDE facility at CERN in July 2017. A particle-γ coincidence experiment using the MINIBALL array and double-sided silicon detectors has allowed the determination of transitional and diagonal matrix elements in ^{66}Ge, yielding new measurements of the reduced transition probability connecting the ground state, 0_1^+, and the first excited state, 2_1^+, or $B(E2; 2_1^+ \rightarrow 0_1^+)$ value, and the spectroscopic quadrupole moment of the 2_1^+ state, $Q_s(2_1^+)$. A relatively large $B(E2) = 29.4(30)$ W.u. has been extracted using beam-gated data at forward angles – less sensitive to second-order effects – as compared with the adopted value of 16.9(7) W.u., but in closer agreement with modern large-scale shell-model calculations using a variety of effective interactions and beyond-mean field calculations presented in the current work. A spectroscopic quadrupole moment of $Q_s(2_1^+) = +0.41(12)$ eb has been determined using the reorientation effect from the target-gated data at projectile backward angles – more sensitive to the reorientation effect. Such an oblate shape is in agreement with the corresponding collective wavefunction calculated using beyond mean-field calculations and its magnitude agrees with the rotational model, assuming $B(E2) = 29.4(30)$ W.u. In addition, high-lying effects have been investigated and considered negligible ($\leq 1\%$). This work solves a long-standing puzzle regarding the loss of quadrupole collectivity in ^{66}Ge and provides a deeper insight into how oblate nuclei rotate.

Keywords

Coulomb Excitation, Reorientation Effect, Shape Coexistence, Neutron-deficient Nuclei.

Acknowledgements

I would thank the Almighty for blessing me with the health and time on this earth to pursue and complete my Ph.D. I am truly grateful for the opportunities, with which my life's path is aligned.

I would also like to thank my parents for the never-ending support that was provided during the past 12 years of my life. I love you and appreciate both of you tremendously. It brings me sadness to know that my mother is no longer with us in the physical to experience and celebrate this milestone in my life. I take comfort in knowing that within me, her spirit lives on and will forever be with me no matter where the journey of life may take me.

I would also like to thank my favourite person in the world and best friend, my wife, Charlize Abrahams. The support you have given me during this journey from undergrad to Ph.D. is indescribable using words. You have been my pillar of strength when things were going tough after Mom passed. I really appreciate the times you listened to me ramble about nuclear physics and spectroscopic quadrupole moments, knowing that you do not understand what I am talking about, just so that I could vent and relieve some stress to continue with what is important to complete the task at hand. I love and appreciate you always and forever.

I would especially like to thank my supervisor Prof. Nico Orce for his outstanding guidance, inspiration and encouragement. The fact that you better your students as individuals and not just our understanding of physics really says a lot about your character as a person. I always said I wanted to become a computational physicist one day and your belief in me has made that dream a very reachable possibility. Your vast guidance on the topics of physics and other more sensitive topics of life is greatly appreciated.

I would like to thank Liam Gaffney for the guidance and knowledge that he shared with me during my stay at CERN. Your help with the sorting code as well as the patience you had with me while learning how to setup MINIBALL is greatly appreciated. Without you even knowing, you have shifted my paradigm of thinking regarding computer science techniques applied to nuclear physics and for that, I am truly grateful. I would also like to thank Nikita Bernier for helping with the analysis of the beta-decay study to determine the beam composition. I would like to thank the University of the Western Cape for the opportunity to study here. Lastly, I would like to thank the SA-CERN collaboration and ISOLDE (CERN) for funding my multiple trips to Switzerland and back.

Contents

List of Figures

UNIVERSITY *of the*

WESTERN CAPE

List of Tables

Abbreviations

CE	**C**oulomb **E**xcitation
RE	**R**eorientation **E**ffect
RDM	**R**ecoil **D**istance **M**ethod
NNDC	**N**ational **N**uclear **D**ata **C**enter
CM	**C**enter of **M**ass
ISOL	**I**sotope **S**eperation **O**n-Line
PS	**P**roton **S**ynchrotron
GPS	**G**eneral **P**urpose **S**eperator
HRS	**H**igh **R**esolution **S**eperator
REX	**R**adioactive beam **EX**periment
EBIS	**E**lectron **B**eam **I**on **S**ource
RFQ	**R**adio-**F**requency **Q**uadrupole accelerator
IH	**I**nterdigital **H** structure
MCP	**M**ulti-**C**hannel **P**late
DSSSD	**D**ouble **S**ided **S**ilicone **S**trip **D**etector
HPGe	**H**igh-**P**urity **Ge**rmanium
DAQ	**D**ata **AQ**uisition system
DGF	**D**igital **G**amma **F**inder
ADC	**A**nalog-to-**D**igital **C**onverter
MBS	**M**ulti **B**ranch **S**ystem
PPQ	**P**airing **P**lus **Q**uadrupole
HFB	**H**artree-**F**ock-**B**ogoluibov
GCM	**G**enerator **C**ordinate **M**ethod
GOA	**G**uassian **O**verlap **A**pproximation
5DCH	**5**-**D**imentional **C**ollective **H**amiltonian
PN-VAP	**P**artical **N**umber **V**ariation **A**fter **P**rojection
SCCM	**S**ymmetry-**C**onserving **C**onfiguration **M**ixing

Chapter 1

Introduction

To date, nuclear interactions between nucleons (protons or neutrons) at different levels (two-nucleon forces, three-nucleons forces, etc.) are not completely understood and there is not a unique nuclear potential to carry out ab initio calculations from first principles as required in the Schrödinger equation. It is therefore our approach to excite the nucleus via the well-known Coulomb interaction and investigate the corresponding nuclear structure. The study of nuclei and their properties based on their proton-neutron configurations is known as nuclear structure. Coulomb excitation (CE) experiments have played an important role in our understanding of fundamental properties of nuclei such as nuclear shapes and nuclear collectivity. Coulomb excitation at bombarding energies well below the Coulomb barrier is the study of nuclei interacting solely through the electromagnetic interaction. Experimental precautions have to be taken with CE measurements to ensure that contributions from the nuclear interaction are negligible.

The electric quadrupole moment of the ground state in even-even nuclei is the simplest nuclear shape property studied in the laboratory frame. The electric quadrupole moment is a measurement of how much the nuclear charge acquires an ellipsoidal shape [17]. The electric quadrupole moment $\hat{Q}$ is classically defined as

$$\hat{Q} = \frac{1}{e}\sqrt{\frac{16\pi}{5}} \int r^2 Y_{20}(\theta, \phi)\rho(r)dV, \tag{1.1}$$

where e denotes the elementary charge, (r, θ, ϕ) the spherical coordinates, $\rho(r)$ the nuclear charge density and Y_{20} is a spherical harmonic. The intrinsic quadrupole moment Q_0 of a nuclear state in the body-fixed frame is given by the expectation value of $\hat{Q}$, whereas the spectroscopic quadrupole moment Q_S is the expectation value of $\hat{Q}$ with respect to the laboratory frame. The intrinsic quadrupole moment is defined as

$$Q_0 = \int \rho(r)(3z^2 - r^2)dV, \tag{1.2}$$

where $\rho(r)$ is the charge density of the infinitesimal volume dV, $r^2 = x^2 + y^2 + z^2$ is the distance to the volume dV, and z is the projection of r on the symmetry axis of the particle. If the charge density is concentrated along the z-direction, the term proportional to $3z^2$ dominates, Q_0 is positive and the nucleus has a prolate deformation. If the charge density is concentrated in the equatorial plane perpendicular to z, the term proportional to r^2 dominates, Q_0 is negative and the nucleus has an oblate deformation. The intrinsic quadrupole moment Q_0 must be distinguished from the spectroscopic quadrupole moment Q_S in the laboratory frame. Because of the vanishing Wigner $3j$ symbol [18], a nuclear state with spin $J = 0$ or $1/2$ does not have a spectroscopic quadrupole moment; however, it may have an intrinsic quadrupole moment as it was realised more than 50 years ago [19].

The reorientation effect (RE) provides a model-independent way to determine Q_S values of excited states with $J \neq 0$ and $1/2$. The RE generates a hyperfine splitting of the nuclear levels which depends on the shape of the nuclear state and allows the determination of Q_S. To convert Q_S to Q_0, we have to make use of the corresponding $3j$ symbols arising from the rotational model [18], where the nucleus is assumed to be an axially symmetric rotor [19]. The relation between the intrinsic and spectroscopic quadrupole moments within the rotational model is given by

$$Q_S = \frac{3K^2 - J(J+1)}{(2J+3)(J+1)} Q_0, \tag{1.3}$$

where K is the projection of the total angular momentum onto the symmetry axis z and reduces to

$$Q_S(2_1^+) = -\frac{2}{7} Q_0(2_1^+) \tag{1.4}$$

for $K = 0$ (ground-state band) and $J = 2$. The rotor model also relates the intrinsic quadrupole moment to the reduced transition probability $B(E2; 0_1^+ \rightarrow 2_1^+)$ (also called $B(E2)\uparrow$) for an electric excitation of multipole order 2 as follows [20]:

$$Q_0 = \left(\frac{16\pi}{5} B(E2; 0_1^+ \rightarrow 2_1^+)\right)^{1/2}. \tag{1.5}$$

More generally, Equation 1.5 is written as [21],

$$\langle J_f||E\lambda||J_i\rangle = (2J_i+1)^{\frac{1}{2}}\langle J_iK_i\lambda\Delta K|J_fK_f\rangle Q_\lambda a_\lambda, \tag{1.6}$$

where $\langle J_iK_i\lambda\Delta K|J_fK_f\rangle$ is a Clebsh-Gordan coefficient, Q_λ is the intrinsic quadrupole moment for an electric transition of multipole order λ, and $a_1 = \sqrt{\frac{3}{4\pi}}$ and $a_\lambda = \sqrt{\frac{2\lambda+1}{16\pi}}$.

Combining Equations 1.4 and 1.5 results in an absolute value for the spectroscopic quadrupole moment extracted from the rotational model given by

$$\left|Q_S(2_1^+)_{B(E2)}\right| = 0.9059B(E2; 0_1^+ \to 2_1^+)^{1/2}. \tag{1.7}$$

The reorientation effect in CE measurements provides a spectroscopic probe to extracting $\langle 2_1^+||E2||2_1^+\rangle$ diagonal matrix elements, which can be related to $Q_S(2_1^+)$ [22] by

$$Q_S(2_1^+) = \sqrt{\frac{16\pi}{5}}\frac{1}{\sqrt{2J+1}}\langle JJ20|JJ\rangle\langle 2_1^+||E2||2_1^+\rangle, \tag{1.8}$$

where $\langle JJ20|JJ\rangle$ is a Clebsh-Gordan coefficient. For $J = 2$, Equation 1.8 reduces to

$$Q_S(2_1^+) = 0.75793\langle 2_1^+||E2||2_1^+\rangle. \tag{1.9}$$

1.1   Scientific Motivation

The macroscopic properties of the atomic nucleus can drastically change when adding or removing a few nucleons. One such feature is the rapid evolution of the nuclear shape. Competing oblate and prolate shapes close to the ground state have been predicted and reported in a few regions of the nuclear chart [23, 24]. The region of neutron-deficient krypton and selenium isotopes with $N \sim Z$ is a region that displays rapid evolution of nuclear shapes, highlighting the importance of the triaxial degree of freedom. Along the krypton isotopic chain between $N = 32$ and $N = 34 - 36$, the shape changes from prolate to oblate [25, 26]. The same trend is observed along the selenium isotopic chain between $N = 34 - 36$ and $N = 38$ [27–29]. Shape coexistence is associated with the shape transition for the krypton isotopes [26, 30, 31]. A comparison of detailed experimental data obtained in CE studies of ^{74,76}Kr with beyond mean-field calculations has demonstrated that a proper description of the structure of these nuclei is not possible without accounting for the triaxial degree of freedom [26, 32]. There are indications of collective and non-collective modes in the low-energy spectra of the germanium isotopes. A systematic study of CE measurements for even-even germanium isotopes suggests that

two deformed shapes coexist in one nucleus and reach maximum shape mixing at ^{72}Ge [33]. The authors of Reference [33] states that it is appropriate to interpret the 0^+ state in ^{70}Ge as a deformed intruder state. Recent experiments on ^{72,76}Ge at Argon National Laboratory [34, 35] provide an extraordinary level of detail on the shape of low-lying states in these nuclei resulting from the model-independent quadrupole sum rules approach. Their conclusion is that both shape-coexisting states in ^{72}Ge exhibit a significant triaxial deformation and that the ground state of ^{76}Ge has a rigid triaxial shape. The rigid triaxial shape for the ground state in ^{76}Ge is further supported by the staggering of the levels in the γ-band reported by [36]. For ^{64}Ge, the measured level energies [37] and the transition probabilities [3] were interpreted in the context of γ-softness, which is further supported by theoretical studies performed by [38].

A view of γ-softness in collective nuclei is provided by the Wilets-Jean (WJ) solvable limit of the Bohr collective model [39, 40]. A test of the γ-soft model would be the measurement of the quadrupole moment of the 2_1^+ state, which would be zero for states of good $SO(5)$ seniority, υ. A vanishing quadrupole moment does not necessarily imply a spherical shape, but equal probabilities of being oblate and prolate. The WJ limit yields a ratio $E(4_1^+)/E(2_1^+) = 2.5$ following the $SO(5)$ energy spectrum dependence of υ, $\Lambda = \upsilon(\upsilon + 3)$ for $\upsilon = (0, 1, 2, ...)$.

The isotope ^{66}Ge exhibits a very small $B(E2; 2_1^+ \to 0_1^+)$ value when compared to neighbouring nuclei. The systematics of $E(2_1^+)$ excitation energies and $B(E2; 2_1^+ \to 0_1^+)$ values in the germanium isotopes is given in Figure 1.1.

The adjacent even-even nuclei, ^{64}Ge and ^{68}Ge, have been reported to be quite collective with transition strengths of $B(E2; 2_1^+ \to 0_1^+) \sim 20$ Weisskopf units (W.u.) [41], whereas ^{66}Ge presents a $B(E2; 2_1^+ \to 0_1^+)$ value similar to the one determined in ^{80}Ge, close to $N = 50$. This decrease in collectivity for ^{66}Ge is also not reflected in the smooth behaviour of $E(2_1^+)$ from $A = 64$ to $A = 70$, as can be seen in the top panel of Figure 1.1.

Furthermore, Figure 1.2 shows the rotational parameter of neutron-deficient Ge isotopes compared to Sr, Se and Kr isotopes. It is clear that ^{66}Ge exhibits an anomalously high 2_1^+ rotational parameter – as compared to the smooth behaviour expected for a rigid rotor – similar to the other Ge isotopes the neutron-deficient Se isotopes. The anomalous rise at $J = 2$ in $^{74-78}$Kr has been attributed to the mixing of coexisting shapes. This is explained by a typical two-state mixing between 0^+ states, which pushes the ground state 0_1^+ and the first excited 0_2^+ state apart, lowering the ground-state energy; hence, $E(2_1^+)$ looks anomalously high. Low-lying excited 0^+ states have been observed in Se [42–44] and Kr [25, 26, 45] isotopes, which could be a signature of shape coexistence [24, 46]. A tentative 0_2^+ state has been predicted by shell-model calculations at approximately 1.2 MeV in ^{66}Ge [12], but was never observed before.
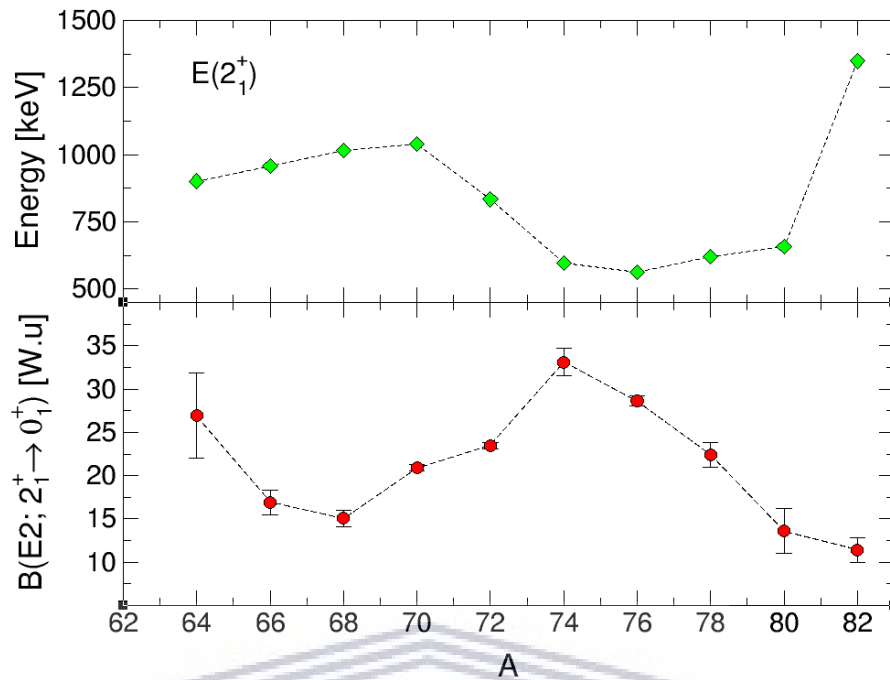
FIGURE 1.1: The top panel shows 2_1^+ excitation energies in keV for even-even germanium isotopes from ^{64}Ge to ^{82}Ge. The bottom panel shows $B(E2; 2_1^+ \to 0_1^+)$ values for the same range of even-even germanium isotopes. The 2_1^+ excitation energies are taken from the NNDC [1]. Adopted $B(E2; 2_1^+ \to 0_1^+)$ values for even-even germanium isotopes taken from the NNDC [2]. The $B(E2; 2_1^+ \to 0_1^+)$ for ^{64}Ge is taken from Ref. [3].
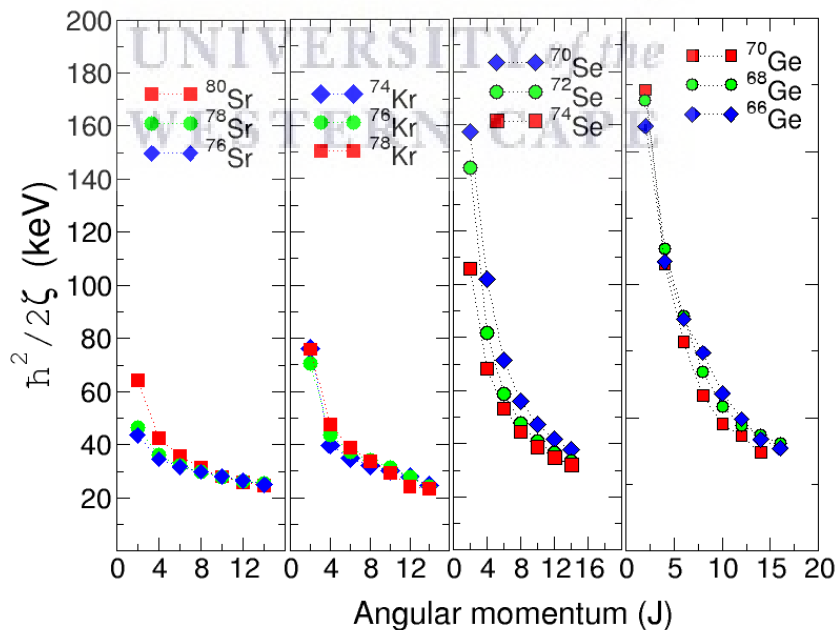
FIGURE 1.2: Comparison of the rotational parameter, $\hbar^2/2\zeta$, for neutron-deficient Sr, Kr, Se isotopes and ^{66}Ge showing an anomalously large rotational parameter for the 2_1^+ states, especially in ^{68,70}Se and ^{66}Ge.

To date, three measurements to determine the $B(E2; 2_1^+ \rightarrow 0_1^+)$ for ^{66}Ge have been carried out. The first one was done by Wadsworth and co-workers in 1979 using the Recoil Distance Method (RDM) [47]. For this experiment, the levels of ^{66}Ge were populated via the ^{58}Ni(^{10}B,$pn\gamma$)^{66}Ge reaction at a beam energy of 29 MeV. A mean lifetime of $\tau = 5.3(10)$ ps was determined for the first 2_1^+ state at 956 keV resulting in $B(E2; 2_1^+ \rightarrow 0_1^+) = 12_{-2}^{+3}$ W.u. The second measurement was performed in 2012 by Lüttke *et al.* using the RDM with the new Yale plunger device [48]. Excited states in ^{66}Ge were populated by using the ^{58}Ni(^{10}B,$p2n$) reaction at a beam energy of 28 MeV. The lifetime of the first 2^+ state in ^{66}Ge was determined through a direct gate on the 1217-keV $4_1^+ \rightarrow 2_1^+$ transition. A relatively shorter mean lifetime of $\tau(2_1^+) = 3.8(5)$ ps was determined, with a resulting $B(E2; 2_1^+ \rightarrow 0_1^+) = 16.9(22)$ W.u. The latest measurement was performed by Corsi *et al.* using intermediate-energy CE in 2013 [49]. A cocktail beam consisting of ^{68}Se (12%), ^{67}As (41%) and ^{66}Ge (30%) was produced by fragmentation of a ^{78}Kr primary beam at 150 MeV/u onto a 329 mg/cm^2 thick ^{9}Be production target. The secondary beam was bombarded onto a 257 mg/cm^2 thick ^{197}Au target with a beam energy of 79 MeV for CE in the middle of the target. A value of $B(E2; 2_1^+ \rightarrow 0_1^+) = 17.7(9)$ W.u. was determined from this experiment, consistent with the result by Lüttke and collaborators.

In 2016, Pritychenko *et al.* compiled experimental $B(E2; 2_1^+ \rightarrow 0_1^+)$ values for 447 even-even nuclei [50]. The previously mentioned $B(E2; 2_1^+ \rightarrow 0_1^+)$ values were used to perform a weighted average resulting in a value of $B(E2; 0_1^+ \rightarrow 2_1^+) = 16.9(14)$ W.u. This new weighted average is currently the accepted value for ^{66}Ge in the National Nuclear Data Center (NNDC) [2]. These $B(E2)$ values can be used to calculate the magnitude of Q_s using the rotor model, but in order to determine the sign of the quadrupole moment, the RE technique is required.

Chapter 2

Coulomb Excitation Theory

Since Coulomb excitation theory was introduced in the late 1950s [22], it has allowed collective quadrupole properties of many stable nuclei to be measured. CE has also allowed many of the known transition probabilities and deformation properties of atomic nuclei to be determined. This technique is especially favoured for exotic radioactive isotopes because it provides a tool to probe the $B(\sigma\lambda)$ value and potentially the quadrupole moments. CE is the excitation of a nucleus via the time-dependent electromagnetic field induced by a collision with another nucleus. If this interaction takes place well below the Coulomb barrier, the distance between the interacting nuclei is larger than the range of the nuclear force. This safety condition ensures that effects from the nuclear force are negligible and the interaction takes place only via the well-understood electromagnetic force [51]. If this condition is met, multipole matrix elements which characterise the electromagnetic decay of the states involved can also be used to express the CE reaction cross section. A determination of the CE reaction cross section allows for the study of electromagnetic properties of low-lying states as well as extracting fundamental nuclear structure information, including the spectroscopic quadrupole moment $Q_s(J^\pi)$ of an excited state. The spectroscopic quadrupole moment provides a way to measure the nuclear charge distribution of a nucleus in the laboratory frame. One of the important aspects of this technique is the population of magnetic substates depending on the quadrupole shape of the state. This is known as the "reorientation effect". The angular distribution of the de-excited γ rays as a function of scattering angle may be enhanced $(Q_s(2_1^+) < 0)$ or inhibited $(Q_s(2_1^+) > 0)$, hence providing a probe for the spectroscopic quadrupole moment Q_s. The difference in the magnetic substate population depends on whether the nuclear shape is prolate, oblate or spherical. An illustration of these shapes is depicted in Figure 2.1.
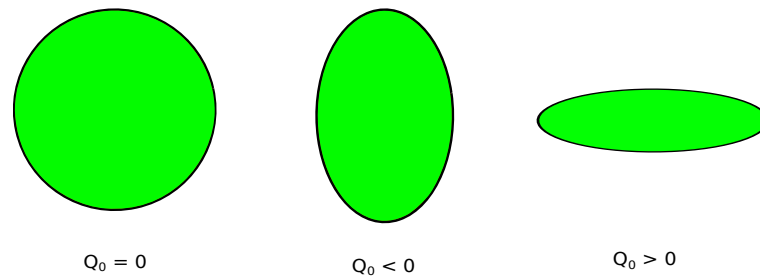
FIGURE 2.1: Nuclear shapes based on the value of the spectroscopic quadrupole moment Q_0.

This dependence on the shape of the nucleus provides a means to determine Q_0 by measuring the CE reaction cross section or integrated γ rays as a function of scattering angle [51]. The theory of CE is discussed extensively in References [22, 51, 52]. This chapter provides a brief description of the relevant theory to determine the spectroscopic quadrupole moment in Section 2.1 and is followed by a description of the CE analysis code GOSIA in Section 2.2.

2.1   Theory Description

A projectile nucleus with atomic mass Z_p is guided onto a target nucleus with atomic mass Z_t. If the energy of the projectile nucleus E_p is well below the Coulomb barrier, the distance of closest approach $b(\theta)$ will be large enough to ensure no nuclear contributions are present in the interaction. This is illustrated using a picture of a classical Rutherford scattering experiment shown in Figure 2.2.
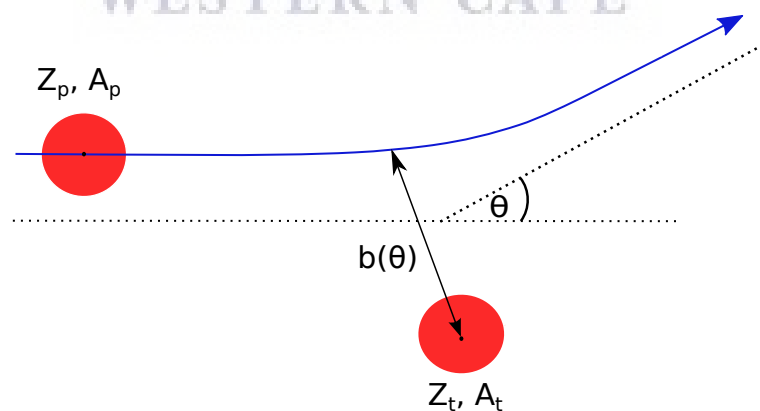
FIGURE 2.2: Coulomb excitation scattering event in the laboratory frame. At the point of closest approach b, the interaction potential is the strongest. The hyperbolic path which the projectile follows is illustrated by the blue arrow.

The strongest point of interaction is reached at the distance of closest approach $b(\theta)$, where the excitation probability is the highest. To obtain the total excitation probability,

the complete particle trajectory has to be included in the calculation as the Coulomb force is a long-range force. This boundary condition and the fact that the theory of electromagnetism is well understood allow for an accurate calculation of both single- and multiple-step excitations. Studies on the effects of Coulomb and nuclear interference have been carried out to estimate the maximum "safe" bombarding energy E_{max} using the masses and charges of the interacting nuclei [22]. The safe bombarding energy for any projectile and target combination can be determined using the classical expression of the minimum distance separating the nuclear surfaces $S(\vartheta)_{min}$ (in fm) given by

$$S(\vartheta)_{min} = \frac{0.72 Z_p Z_t}{E_{max}}(1 + \frac{A_p}{A_t})[1 + \csc(\frac{\vartheta}{2})] - R_0(A_p^{1/3} + A_t^{1/3}), \qquad (2.1)$$

where $R_0 = 1.25$ fm is the average nucleon radius, $A_{p/t}$ and $Z_{p/t}$ is the mass and charge respectively of the projectile nucleus (p) and the target (t) and E_{max} is the maximum bombarding energy of the projectile. This minimum distance has been shown to be 5 fm to ensure that only 0.1% of the total interactions are due to the nuclear force [53]. This gives rise to an expression for the distance of closest approach in a head-on collision:

$$R_0(A_p^{\frac{1}{3}} + A_t^{\frac{1}{3}}) + 5 > b = \frac{Z_p Z_t e^2}{E_p}, \qquad (2.2)$$

where E_p is the kinetic energy of the projectile. The theory may rely upon first- and second-order perturbation theory to describe a one- or two-step process, making it relatively easy to study properties in light-ion beams. The study of heavier beams with many states presents a complex problem that has to be solved using a numerical method. This complexity gave rise to GOSIA, the CE code which will be discussed in Section 2.2.

2.1.1 Semiclassical Approximation

Coulomb excitation theory can be treated in two ways. The first is a fully quantum mechanical approach as discussed in Reference [51]. It can also be treated using a semiclassical approximation in which the whole scattering and excitation processes follow the classical Rutherford trajectories. The electromagnetic excitation has a negligible effect on the trajectories and is treated fully quantum mechanically. The semiclassical picture is justified if two conditions are met. First, the particle has to be described by a wave packet with dimensions that are small compared to the distance of closest approach. This condition is satisfied when the Sommerfeld parameter η is much greater than unity:

$$\eta = \frac{2\pi a}{\lambda} = \frac{Z_p Z_t e^2}{\hbar v_p} \gg 1, \tag{2.3}$$

where $a = b/2$, half the distance of closest approach, λ is the de Broglie wavelength of the projectile with a velocity of v_p, and $Z_p e$ and $Z_t e$ are the charges of the projectile and target nucleus, respectively. The strong repulsive Coulomb interaction between the projectile and target nucleus implied by $\lambda \gg 1$ guarantees that the projectile will not penetrate the target nucleus. Second, the energy loss of the impinging particle has to be small when compared to the bombarding energy. The hyperbolic trajectory that the projectile follows in the semiclassical approximation can only be true if the incoming energy and outgoing energy are similar. This implies that the elastic scattering can be used to approximate inelastic scattering with the energy loss being negligible. Since the energy transfer between the projectile and target can occur at any point along the path of the trajectory, the energy loss of the impinging particle has to be small relative to the center-of-mass (CM) energy. This condition can be expressed as [22]

$$\frac{\triangle E}{E} \ll 1, \tag{2.4}$$

where the CM energy is given by $E = \frac{1}{2} m_0 v_b^2$ and m_0 is the reduced mass. It is also useful to define the adiabaticity parameter ξ as the difference between the incoming η_i and outgoing η_f:

$$\xi = \eta_i - \eta_f = \frac{Z_p Z_t A_p^{1/2} \triangle E}{12.65 E^{3/2}} = \frac{\eta \triangle E}{2 E_p}. \tag{2.5}$$

For $\xi \leq 1$, we have a "sudden impact" collision, and the large torque yields a large excitation probability; whereas for $\xi \gg 1$, the collision is adiabatic and the excitation cross section vanishes, in concordance with the exponential behaviour of the orbital integrals ($\propto e^{-\xi \epsilon}$), where ϵ is the eccentricity of the orbit [22]. Furthermore, ξ can also be interpreted as the ratio of the collision time relative to the lifetime of the nuclear state being excited:

$$\xi = \frac{t_{collision}}{\tau_{nuclear}} = \frac{a}{v} \frac{1}{\omega_{if}}, \tag{2.6}$$

where the lifetime of the excited nuclear state $\tau_{nuclear}$, can be calculated at an excitation energy ΔE using the uncertainty principle:

$$\tau_{nuclear} = \frac{\hbar}{\Delta E}. \tag{2.7}$$

With both the conditions justifying the semiclassical approximation satisfied, it is valid for the analysis of heavy ion CE. In this approach, the Rutherford cross section σ_R associated with the projectile's motion is described by

$$d\sigma_R = \frac{1}{4}a^2 \sin^{-4}\left(\frac{\vartheta}{2}\right)d\Omega, \tag{2.8}$$

where ϑ is the CM scattering angle and a is half the distance of closest approach in a head-on collision. If, during the collision, the nucleus undergoes a transition from an initial state $|i\rangle$ to a final state $|f\rangle$, the CE cross section may be related to the Rutherford cross section by

$$d\sigma_f = P_{if}d\sigma_R, \tag{2.9}$$

where P_{if} is the excitation probability that the nucleus is excited in the collision and scatters into the solid angle $d\Omega$. The excitation probability P_{if} is expressed as

$$P_{if} = \frac{1}{2I_i + 1}\sum_{M_i M_f}|a_{if}|^2, \tag{2.10}$$

where a_{if} are the excitation amplitudes for exciting a nucleus from the ground state with spin I_i to a final state with spin I_f, and M_i and M_f are the magnetic substates quantum numbers of the initial and final states, respectively. The perturbation treatment of the semiclassical approximation provides a way to understand the excitation process. For CE involving light ions, first-order perturbation treatment for the excitation process may be adequate. Heavier targets in scattering experiments enhance second- and higher-order terms in the perturbation expansion of the CE cross section and hence, higher-order perturbation theory is necessary. Magnetic transitions are hindered by a factor of v/c when compared to electric transitions of the same multipole order and can therefore be disregarded in the perturbation treatment.

2.1.2   First-order Perturbation Theory

First-order perturbation may be used to evaluate the excitation amplitudes of the Coulomb-excited states given that higher-order contributions or couplings are negligible. The first-order perturbation treatment of the cross-sections describes the interaction

taking place between the electromagnetic field, created by one collision partner acting on the other, and the system of nuclear charges of the collision partners involved. This approach yields reasonable estimates for the excitation amplitude and cross sections of nuclei with final state $|f\rangle$ which are strongly coupled to the initial state $|i\rangle$ through a large matrix element, where $|f\rangle$ is not strongly coupled to any other high-lying states. This is illustrated in Figure 2.3.
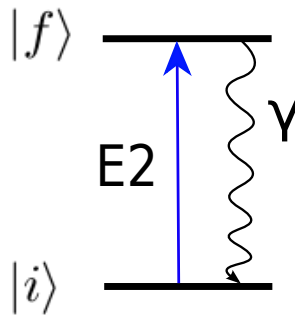
FIGURE 2.3: One-step excitation from an initial state $|i\rangle$ to a final state $|f\rangle$, with the excitation and de-excitation clearly shown. This approximation can be used for example the 2_1^+ state in an even-even nucleus.

A simple way to express the excitation process for CE is to treat it as a first-order perturbation [51] of the time-dependent Schrödinger equation of the form:

$$i\hbar\frac{\partial}{\partial t}|\psi(t)\rangle = H(t)|\psi(t)\rangle, \tag{2.11}$$

where the Hamiltonian $H(t)$ can be separated into three parts of the electromagnetic interaction. The first is the monopole-monopole term $H_0(t)$, which treats the Rutherford scattering and the classical trajectories. The second term is the monopole-multipole term $V(r(t,\theta,\phi))$, which is responsible for the excitation of either collision partner. The third term is the multipole-multipole term which is responsible for the excitation of both the target and projectile nuclei simultaneously. The probability of exciting both the projectile and target is negligible compared to the excitation of a single collision partner and can therefore be excluded from the Hamiltonian. The Hamiltonian can then be expressed as

$$H(r(t)) = H_0(r(t)) + V(r(t)). \tag{2.12}$$

The time-dependent interaction potential $V(r(t))$ originating from one collision partner influencing the second is used to calculate the excitation probabilities along the whole

trajectory [54]. From first-order time-dependent perturbation theory, the excitation amplitudes may be expressed as

$$a_{if} = \frac{1}{\hbar} \int_{-\infty}^{\infty} \langle f|V(r(t))|i\rangle e^{i\omega_{if}t}dt, \tag{2.13}$$

where $\omega = \Delta E/\hbar$ and $\Delta E = E_f - E_i$ is the excitation energy for a transition from an initial state with energy E_i to a final state with an energy E_f. Performing a multipole expansion on the monopole-multipole term allows the excitation amplitudes a_{if} to be evaluated. The interaction responsible for electric multipole transitions is defined in Reference [51] as

$$V(r(t)) = 4\pi Z'e \sum_{\lambda=1}^{\infty} \sum_{\mu=-\lambda}^{\lambda} \frac{(-1)^{\mu}}{2\lambda+1} M(E\lambda, \mu) Y_{\lambda\mu}(\theta, \phi) r^{-\lambda-1}, \tag{2.14}$$

where λ and μ are the multipole order of the excitation, Z' is the atomic number of the other collision partner, $Y_{\lambda\mu}(\theta, \phi)$ are the spherical harmonics with angles θ and ϕ given in the center of mass frame, and $M(E\lambda, \mu)$ is the electric multipole operator which is defined as

$$M(E\lambda, \mu) = \int r^{\lambda} Y_{\lambda\mu}(\theta, \phi)\rho(r)d\tau, \tag{2.15}$$

where $\rho(r)$ is the nuclear charge density. At this point, the magnetic multipoles can be neglected since the magnetic excitations scale with a factor of $(v/c)^2$ and are much smaller than their electric counterparts in the non-relativistic case. The transition amplitudes can be evaluated by substituting Equation 2.14 into Equation 2.13, yielding

$$a_{if} = \frac{4\pi Z'e}{i\hbar} (-1)^{\mu} S_{\mu\lambda} \langle I_i M_i|M(E\lambda, \mu)|I_f M_f\rangle, \tag{2.16}$$

where $S_{\mu\lambda}$ denotes the orbital integral along the classical trajectory r given by

$$S_{\mu\lambda} = \int_{-\infty}^{\infty} e^{i\omega t} Y_{\lambda\mu}(\theta(t), \phi(t))[r(t)]^{-\lambda-1}dt. \tag{2.17}$$

The reduced matrix elements of the electric multipole operators can be given by the Wigner-Eckart theorem:

$$\langle I_i M_i | M(E\lambda, \mu) | I_f M_f \rangle = (-1)^{I_i - M_i} \begin{pmatrix} I_i & \lambda & I_f \\ -M_i & \mu & M_f \end{pmatrix} \langle I_f || M(E\lambda) || I_i \rangle. \qquad (2.18)$$

These reduced transition elements are related to the transition strengths $B(E\lambda)$, such that the reduced transition probability may be written as

$$B(E\lambda; I_i \rightarrow I_f) = (2I_i + 1)^{-1} |\langle I_i || M(E\lambda) || I_f |^2. \qquad (2.19)$$

The CE cross section for electric excitations may then be expressed as

$$\sigma_{E\lambda} = \frac{Z' e^2}{\hbar v} a^{-2\lambda + 2} B(E\lambda) f_{E\lambda}(\xi), \qquad (2.20)$$

where $f_{E\lambda}(\xi)$ is the dimensionless CE function containing all the information about the classical trajectory of the scattered particles. The values for $f_{E\lambda}(\xi)$ are tabulated in Reference [51]. The total CE cross section expressed in Equation 2.20 is directly proportional to the reduced transition probabilities expressed in Equation 2.19.

2.1.3 Second-order Pertubation Theory

In the framework of first-order perturbation theory, excitation amplitudes are typically quite small: $a_{if} \ll 1$. For heavy-ion collisions, the transition probability increases with ion energy and thus, the condition $a_{if} \ll 1$ may no longer be satisfied and second-order effects have to be considered. Two consequences arise from this condition: first-order transition probabilities may be affected by second-order terms, and states which were previously not accessible may be populated using multi-step excitations [51]. To account for second-order effects, the excitation has to be treated using second-order perturbation theory while still maintaining the classical trajectories. A second excited state $|f\rangle$ may be reached through the excitation of an intermediate state $|m\rangle$ from an initial state $|i\rangle$ given by

$$a_{if}^{(2)} = a_{if}^{(1)} + a_{imf}^{(1,2)}, \qquad (2.21)$$

where $a_{if}^{(1)}$ is defined in Equation 2.13 and $a_{imf}^{(1,2)}$ is the amplitude of the transition from the intermediate state to the final state given by

$$a_{imf}^{(1,2)} = \frac{1}{i\hbar} \int_{-\infty}^{\infty} \langle f|V(r(t))|m\rangle e^{i\omega_{mf}t} \times \langle m|V(r(t))|i\rangle e^{i\omega_{im}t} dt. \tag{2.22}$$

These first- and second-order processes interfere with each other and therefore have to be included in the calculation regardless of how small the probability of the multi-step excitation may be. This interference leads to a phenomenon known as the Reorientation Effect (RE). This effect, which is typically observed in $E2$ transitions of even-even nuclei, occurs when the intermediate state $|m\rangle$ and the final state $|f\rangle$ in a multi-step excitation are magnetic substates of the same excited state. The RE is illustrated in Figure 2.4.
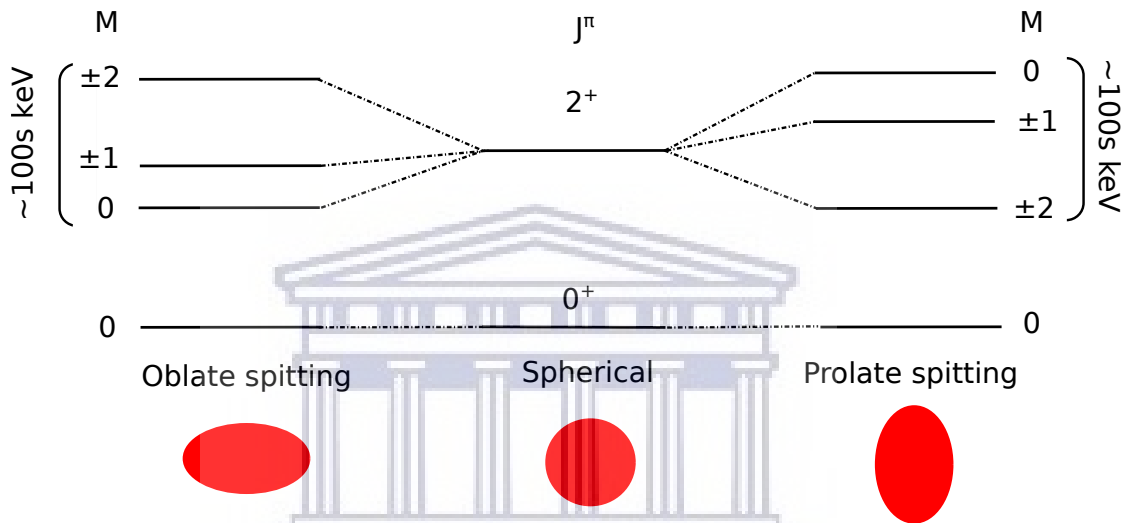
FIGURE 2.4: Schematic representation of the reorientation effect. The final state $|f\rangle$ can be reached via an intermediate state $|m\rangle$. The final state can be one of the magnetic substates of the excited state. The splitting of the energy levels which the magnetic substates can take is dependent on the static quadrupole moment by the relation $E(t) \sim eQ_s Z/r^3(t)$.

From Equation 2.21, it can be seen that the excitation amplitude of a state k depends on the coupling of all n states. This, in turn, means that the reduced matrix elements defined in Equation 2.18 are coupled for all n states. A numerical approach is required to solve this complex system of coupled differential equations.

2.2 GOSIA

Advances in the semiclassical theory for multiple CE have led to the development of computer programs that can solve the vast amount of coupled differential equations numerically. The first of these numerical minimisation programs is known as COULEX, developed by Winther and de Boer [55]. The input of this code is a set of initial matrix elements, level schemes of the nuclei involved in the collision and the experimental

details, such as the beam energy to computes the statistical tensors. A separate code known as CEGRY [], accepted the statistical tensors calculated by COULEX as input, to predict the subsequent γ-ray decay properties. The calculations have to be corrected for the transfer of energy to excite the nucleus as well as for systematic errors. This correction is achieved by introducing symmetrised orbits in the semiclassical calculations. The calculated and measured yields can be made to agree with each other by manually varying the model-dependent parameters. This model-dependency proved to be of concern for semiclassical multiple CE calculations where a large number of reduced matrix elements could contribute significantly to the excitation of a single state. The introduction of GOSIA [56], in 1980, overcame this model-dependency.

GOSIA accepts a set of electric ($E1$ to $E6$) and magnetic ($M1$ and $M2$) multipole matrix elements and calculates the excitation cross section for multiple excitations. It can be used for simulating an experiment by determining optimum angles and beam/target combinations to use in an experiment. GOSIA can also be used to analyse real data by fitting matrix elements independently to a number of data. The γ-ray yield of a given transition, following the de-excitation of a state populated during the collision, is the most important observable. It allows the excitation and decay to be compared since the matrix elements that govern the decay of these populated states are the same matrix elements that determine the excitation. GOSIA also allows for independent data, such as lifetimes of excited states, known matrix elements, branching ratios and $E2/M1$ mixing ratios, to be included in the fit. Numerical integration of the coupled-channel differential equations is performed to calculate the cross-section and consequently, the γ-ray yields [56].

The calculation is done at a single value for energy and angle and is referred to as the "point yield", given by

$$Y_{point}((I \to I_f), \theta_p, E) = \sin(\theta_p) \int_{\phi_p} \frac{d^2\sigma(I \to I_f)}{d\Omega_\gamma d\Omega_p} d\phi_p. \tag{2.23}$$

The integrated yields are calculated by integrating over the entire solid angle and the range of bombarding energies resulting from the energy loss in the target given by

$$Y_{int}(I \to I_f) = \int_{E_{min}}^{E_{max}} dE \frac{1}{\left(\frac{dE}{dx}\right)} \int_{\theta_{p,min}}^{\theta_{p,max}} Y_{point}(I \to I_f) d\theta_p, \tag{2.24}$$

where $\frac{dE}{dx}$ is the stopping power of the target material obtained using SRIM [57]. Equation 2.24 includes the Rutherford cross-section and the solid angle factor $\sin(\theta_p)$.

Computing Equations 2.23 and 2.24 for many angles and energies can be time consuming. To speed up this process, GOSIA makes use of yields calculated over an average bombarding energy and an average scattering angle. These average point yields are corrected by a constant factor calculated along with the integration. The integration along with the recalculation of the correction factor has to take place again only if the matrix elements diverge significantly. The correction constant is given by

$$Y_{exp}^c(I \rightarrow I_f) = Y_{exp}(I \rightarrow I_f) \frac{Y_{point}(I \rightarrow I_f)}{Y_{int}(I \rightarrow I_f)}, \qquad (2.25)$$

where $Y_{exp}(I \rightarrow I_f)$ is the experimental yield. The fitting of the matrix elements is performed by locating a χ^2 minimum in Equation 2.24 given by

$$\chi^2 = \frac{1}{N} \sum_i \left(\frac{Y_{calc}(i) - Y_{exp}^c(i)}{\Delta Y_{exp}^c(i)} \right)^2, \qquad (2.26)$$

where $Y_{calc}(i)$ are the calculated yields, $Y_{exp}^c(i)$ are the "corrected" experiment yields, $\Delta Y_{exp}^c(i)$ are the errors in the "corrected" experiment yields and N is the number of data points in the fit.
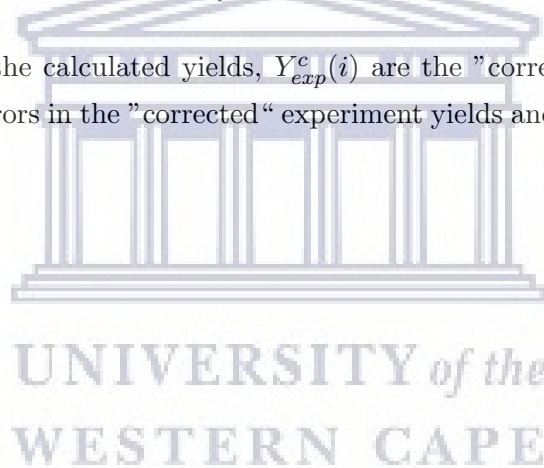
Chapter 3

Experimental Methodology

The CE of the unstable nucleus ^{66}Ge was performed in 2017 at the ISOLDE facility at CERN in Switzerland. This chapter details the experimental methodology used to obtain the necessary beam parameters as well as the equipment used to successfully perform the CE experiment. Section 3.1 discusses the beam production process at the HIE-ISOLDE facility and Section 3.2 discusses MINIBALL, the array of High Purity Germanium (HPGe) detectors used to perform the measurement.

3.1 ISOLDE Facility

The ISOLDE facility, based at CERN in Geneva, Switzerland, is a rare isotope production facility. The ISOLDE facility utilises the "Isotope Separation On-Line" (ISOL) technique, one of the commonly used methods used to study low-energy properties of exotic nuclei. This method allows for the production of both neutron-rich and neutron-deficient nuclei with very low recoil velocity. To produce the necessary beam, the following steps associated with the ISOL method must be taken: (i) the bombardment of a thick heavy target with protons, (ii) the diffusion of nuclei out the primary target into an ion source, and (iii) the ionisation, extraction and mass separation of the desired beam. The following sections discuss the beam production and post-acceleration process in detail. Figure 3.1 shows an illustration of the layout of the ISOLDE facility as it stands to date.

3.1.1 Isotope Production

The beam production at ISOLDE starts with a beam of high energy protons received from the Proton Synchrotron (PS) Booster with an energy of 1.4 GeV. The protons
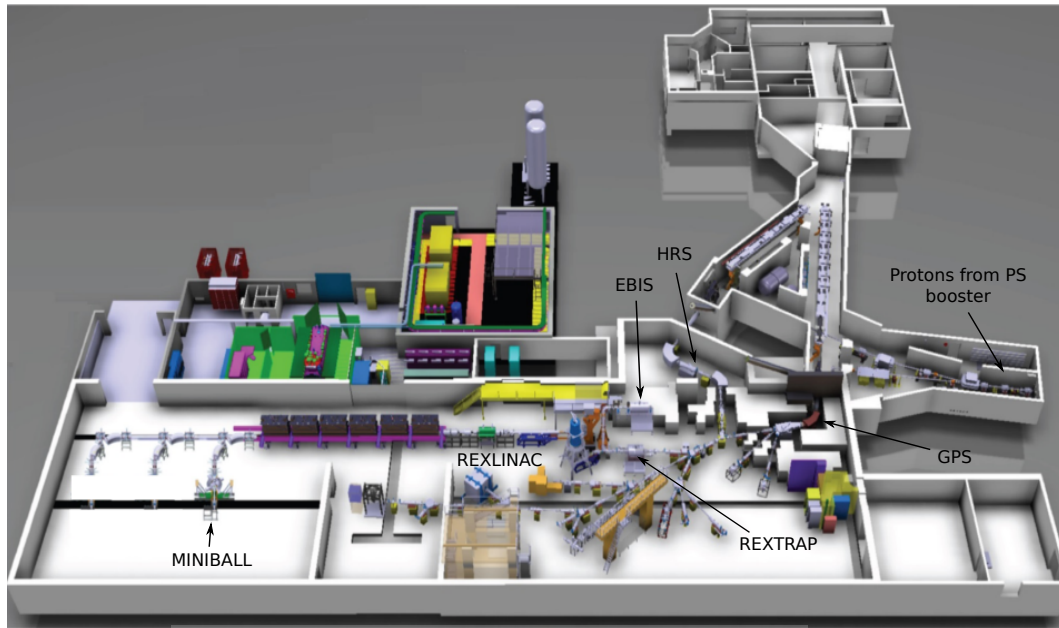
FIGURE 3.1: Schematic overview of the ISOLDE facility after the HIE-ISOLDE upgrades. There are many experimental setups in the ISOLDE hall, only those used during this experiment are labelled.

are guided from the PS-Booster to ISOLDE in pulses with a minimum spacing of 1.2 s between pulses. Each pulse can reach a maximum intensity of 3.2×10^{13} ions/s, which would result in a maximum integrated intensity of 4 μA. However, due to safety regulations, the spacing between pulses is increased to 2.4 s, such that the average integrated intensity amounts to 2 μA [58]. It is possible to take consecutive pulses from the PS booster as long as the number of proton pulses hitting an ISOLDE production target does not exceed 50% of the total number of pulses in the PS booster supercycle. These proton beams are then guided to one of two primary targets, each coupled to a different mass separator. The target can be stored inside the target chamber, usually consisting of graphite or tantalum, in one of the following forms: powder, metal, molten metal or pills of carbon fibers. Many parameters have to be considered when choosing the target material to ensure that the maximum beam intensity of the requested isotope may be delivered. These properties are the production cross section, release characteristics, density, mechanical and thermal resistance, melting point, target structure and electrical conductance, to name a few.

The impingement of the high energy proton beam onto the thick primary target produces a variety of radioactive isotopes via fission, fragmentation and spallation processes. In approximately 70% of the cases, $^{238}UC_x$ is used as a primary target. The beam intensity may be increased by heating the target which enhances effusion and diffusion processes. The heating of the target also increases the contaminants, thus there is an optimum

heating to get the best ratio between the element of interest and the contaminants for any given beam. Another consideration is the extraction of the required isotope as a molecular beam. The molecular beam approach allows for purer beams of the required isotope. Knowledge of the chemical properties of the desired isotope is required, such that a molecule consisting predominately of the desired isotope may be created. This approach also reduces possible contaminants as the production of a chemical compound with the remaining isotopes should be suppressed. The primary target used in this experiment was ZrO_2. The [70] beam was to be produced with the $^{70}SeCO$ molecules. However, the sulphur in the primary target allowed for the production of ^{66}GeS molecules in excess to that of the $^{70}SeCO$ molecules. This ratio kept increasing in favour of ^{66}GeS inevitably resulting in a beam of ^{66}Ge. The ionisation of the molecules was done using surface ionisation, whereby the transfer line, usually made of tungsten or tantalum, was heated to strip electrons from the desired molecules. This is possible since germanium has a lower thermionic work function than tungsten or tantalum. The ionised molecules (1^+ charge state) are then extracted from the target-ion source by applying a 30 to 60-kV external electrostatic potential. After this extraction process, the desired molecules have to be selected and guided to the experimental setup. This selectivity is achieved using the mass-over-charge ratio (A/q) with the use of two different mass separators: the General Purpose Separator (GPS) and the High Resolution Separator (HRS). Figure 3.2 depicts the beamline layout in the ISOLDE hall, showing the HRS and GPS mass separators.
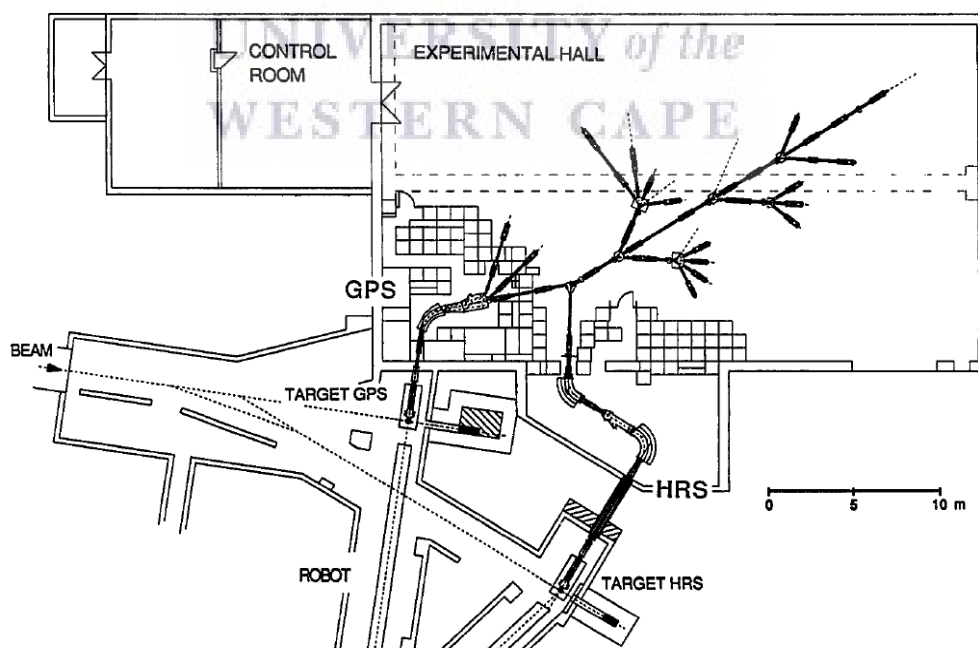
FIGURE 3.2: Schematic overview of the beamline layout in the ISOLDE hall. Both the HRS and GPS mass separators are illustrated [4].

Each mass separator is connected to its own target station, allowing for flexible beam delivery. These mass separators feed one common beamline which delivers the beam to the majority of the available experimental setups in the ISOLDE facility. The following subsection gives more detail about GPS since it was the mass separator used for this experiment. One can refer to [58] for a more detailed description of HRS.

3.1.1.1 GPS

The General Purpose Separator is the smaller of the two isotope separators available at the ISOLDE facility. It is comprised of two electrostatic quadrupole lenses followed by a double-focusing $70°$ magnet with a mean bending radius of 1.5 m. The analysing magnet is followed by the switchyard, which is located in the focal plane and allows for the selection of three ion beams within a mass range of $\pm 15\%$ from the central mass [58]. The switchyard is made of pairs of electrostatic cylinder-shaped deflector plates, one on either side of the central mass. The selection of the mass is achieved by moving the deflector plates parallel to the focal plane. Figure 3.3 shows a picture of the switchyard used in GPS. The ^{70}SeCO and ^{66}GeS molecules were selected using an $A/q = 98$ with a charge state of $q = 1$.
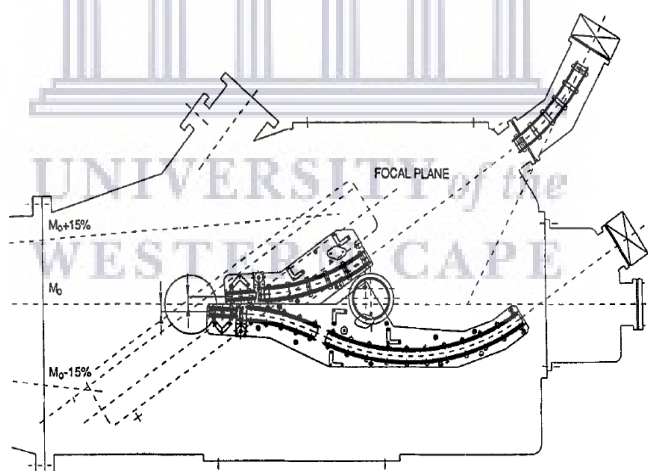
FIGURE 3.3: GPS switchyard [4].

3.1.2 Post-acceleration

The radioactive ion beam is delivered with an initial beam energy of 30 to 60 keV to the various low energy experimental setups in the ISOLDE experimental hall. The Radioactive beam EXperiment (REX) was designed to further accelerate beams from ISOLDE to beam energies of up to 3.0 MeV/u. The post-acceleration unit comprises

of a penning trap for de-acceleration and bunching of the beam, followed by a charge breeding system. This process allows for a compact accelerator to be used to accelerate beams to moderate energies without the need for a large-scale accelerator. Figure 3.4 shows a schematic overview of HIE-ISOLDE after the installation of the upgrade. The following sections describe in more detail each of the components that make up the post-acceleration process.
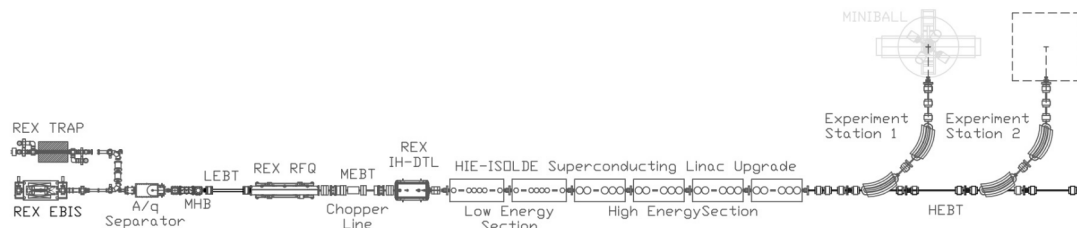
FIGURE 3.4: A Detailed layout of HIE-ISOLDE [5]

3.1.2.1 REXTRAP

The singly-charge ion beam from GPS is injected into REXTRAP, a penning trap designed to cool and bunch the ions. REXTRAP is shown on the left in Figure 3.5. REXTRAP consists of two regions: one for stopping the ions and the other to trap them. Both these regions are typically filled with neon or argon as a buffer gas [59]. Incoming ions are cooled by collisions with the buffer gas and trapped in an applied High-Voltage (HV) field. To further increase the energy loss of the ions, the pressure in the trapping region is an order of magnitude lower than in the stopping region. In addition, the 3-T magnetic field allows for the confinement of the ions in the center of the trap. Within the applied electric and magnetic fields, the ions are forced into a magnetron motion around the trap center, a reduced cyclotron motion and an axial motion (harmonic oscillation). The collisions with the buffer gas disrupt the magnetron motion of the ions and increase their orbit. Recentering of the ions of interest is achieved by applying a radio-frequency field with a cyclotron frequency that matches the desired ion's mass.

3.1.2.2 REXEBIS

At this point of the post-acceleration, the beam has been deaccelerated and bunched. It then gets injected into the Electron Beam Ion Source (EBIS) for charge breeding [60]. REXEBIS is shown on the right in Figure 3.5. The charge breeding process is essential to achieve a beam energy of 5.5 MeV/u with the subsequent compact linear accelerator.
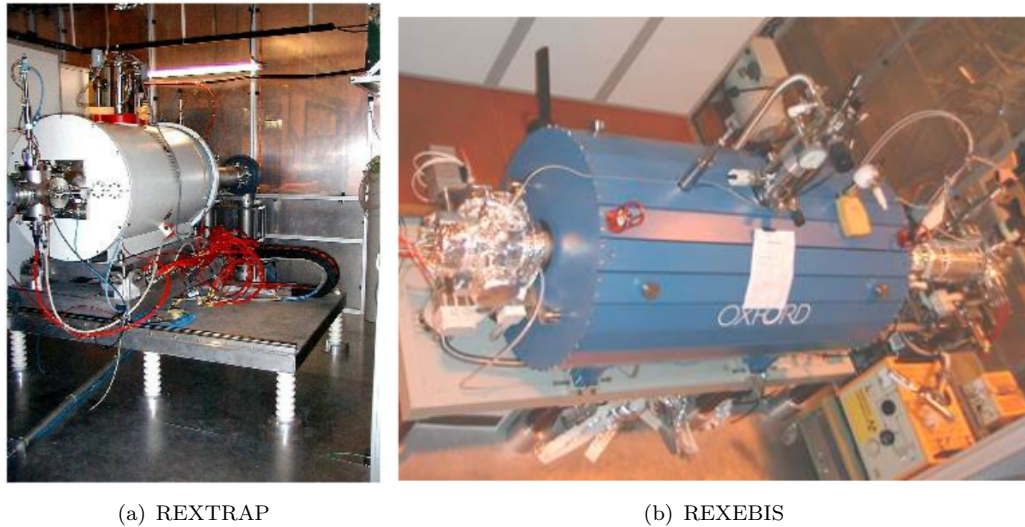
(a) REXTRAP   (b) REXEBIS

FIGURE 3.5: Images of REXTRAP (left) and REXEBIS (right) at ISOLDE, CERN.

The charge breeding in EBIS is achieved through electron impact. The incoming ions are confined within a trapping region and bombarded with an electron beam. The electron beam, typically 3 to 6 keV with a current of 200 mA, is provided by an electron gun (cathode) which is focused by employing a 2-T magnetic field within a superconducting solenoid. The ions are confined within the negative space charge of the electron gun inside the magnetic field and the electric field generated by the electrodes at the front and back side of the EBIS. The breeding time is dependent on the A/q ratio for the isotope of interest [61]. For this experiment, a charge state of $q = 16$ was selected resulting in $A/q = 4.125$ for ^{66}Ge. A charge state of $q = 15$ resulting in $A/q = 4.4$ would allow for a shorter breeding time in EBIS but would also allow one of the major contaminants in EBIS through the selection. A $A/q = 66/15$ would select ^{22}Ne^{5+} from the buffer gas used in REXTRAP would be selected with a third of the mass and third of the charge. The Neon from the buffer gas is used in the determination of the detector angles discussed in Section 4.2. Following the beam extraction from REXEBIS, it has to be separated with respect to the A/q ratio since contaminants may overweigh the desired radioactive isotope. Most contaminants are due to residual gas inside REXEBIS. A high vacuum of 10^{-11} mbar is maintained within the EBIS to improve charge breeding as well as to suppress the production of contaminants.

3.1.2.3 A/q Separator

The mass separator that connects REXEBIS to REXLINAC is mounted vertically in an S-shaped structure. The selection of the correct A/q ratio is achieved with the use of a 90° electrostatic deflector which is followed by a 90° magnetic bender. The electrostatic

deflector is used to minimise the energy spread from REXEBIS while the magnetic bender selects the correct A/q and eliminates most of the contaminants. Contaminants with similar energy and similar A/q pass the mass separator and reach the final experimental setup. The most common contaminants are carbon, oxygen, nitrogen, neon and argon which are residual gases ionized in REXEBIS.

3.1.2.4 REXLINAC

The bunched and separated ions are injected into REXLINAC, the compact linear accelerator stationed in the ISOLDE facility. REXLINAC is a room temperature accelerator designed to post-accelerate radioactive ion beams with $A/q < 4.5$. REXLINAC is comprised of a radio-frequency quadrupole accelerator (RFQ), an interdigital H structure (IH), three 7-gap resonators and a 9-gap resonator; each of which increases the beam energy in the subsequent steps. Figure 3.6 shows a schematic overview of REXLINAC.
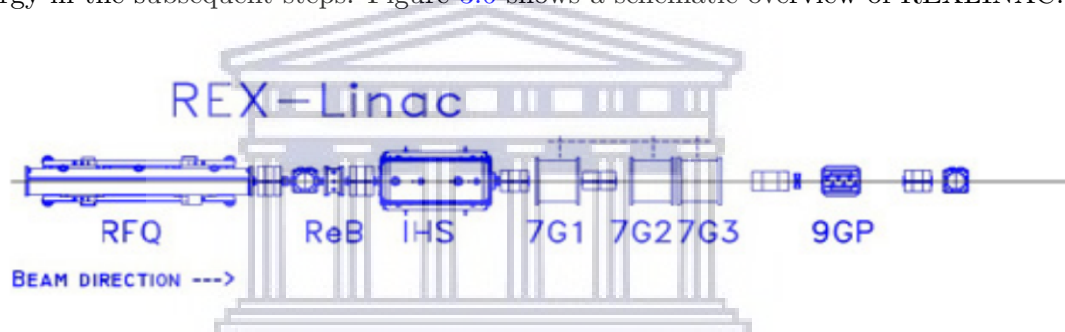
FIGURE 3.6: REXLINAC at ISOLDE, CERN. A breakdown of the components that make up the LINAC is shown. [6]

The ion beams are injected into the RFQ with an energy of 5 keV/u. The RFQ accelerates the beam to 300 keV/u and injects it into the IH structure. The 20-gap IH cavity operates at a frequency of 101.28 MHz and increases the beam energy to 1.2 MeV/u [62]. The subsequent 7-gap resonators operate at the same frequency as the IH structure and allow the beam energy to be tuned in the range of 0.8 to 2.0 MeV/u. The final boost of energy is achieved with the 9-gap resonator. This 9-gap IH unit operates at twice the frequency of the 7-gap resonators and allows the beam energy to be increased to 3.0 MeV/u. The beam intensity may vary between a few 100 to 10^7 ions/s, which is measured using Faraday cups, multi-channel plates (MCP) and phosphor screens [61]. At beam intensities below 0.1 pA, the measurement devices are not able to detect the beam. For this reason, a stable beam with enough intensity and a similar A/q ratio is used to obtain the set of accelerator parameters [61].

3.1.2.5 HIELINAC

To further increase the science opportunities at ISOLDE, it was evident that a beam energy upgrade was needed. In 2006, it was commissioned to expand the existing REXLINAC with an additional superconducting linear accelerator, high energy beam transfer lines and three additional experimental beamlines [61]. With these upgrades, the superconducting post-accelerator at ISOLDE is known as HIELINAC and consists of six cryomodules with a total of 32 radiofrequency cavities. The upgrade to REXLINAC happened in three phases. The first phase was the design and installation of two of the cryomodules. Each of these cryomodules consists of five high-beta cavities operating at 101.28 MHz and a superconducting solenoid magnet. Figure 3.7 shows the complete assembly of one of the cryomodules.

FIGURE 3.7: One of the cryomodules being installed in the ISOLDE hall. [7]

The experiment that this work is based on was performed in 2017 after the first phase was completed, which allowed the beam energy to be enhanced to 5.5 MeV/u for nuclei with $A/q < 4.5$. The resulting beam energy of the unstable ^{66}Ge isotope was 4.395 MeV/u with an $A/q = 4.125$. The second phase, which was completed in 2018, comprised of the installation of an additional cryomodule with similar specifications as previously mentioned. The final phase of the upgrade, which took place in 2020, is to replace the 7-gap and 9-gap resonator structures from REXLINAC with two more cryomodules. Each of these cryomodules consists of six low-beta cavities and two superconducting solenoid

magnets. After the completion of the final phase, HIELINAC will provide radioactive ion beams with energies up to 10.0 MeV/u without the beam quality degrading.

3.1.3   Beam Time Structure

The radioactive ion beams at ISOLDE are bunched. To ensure that the beam is delivered in an efficient manner, ISOLDE employs a timing structure. Figure 3.8 illustrates a typical time structure at ISOLDE.
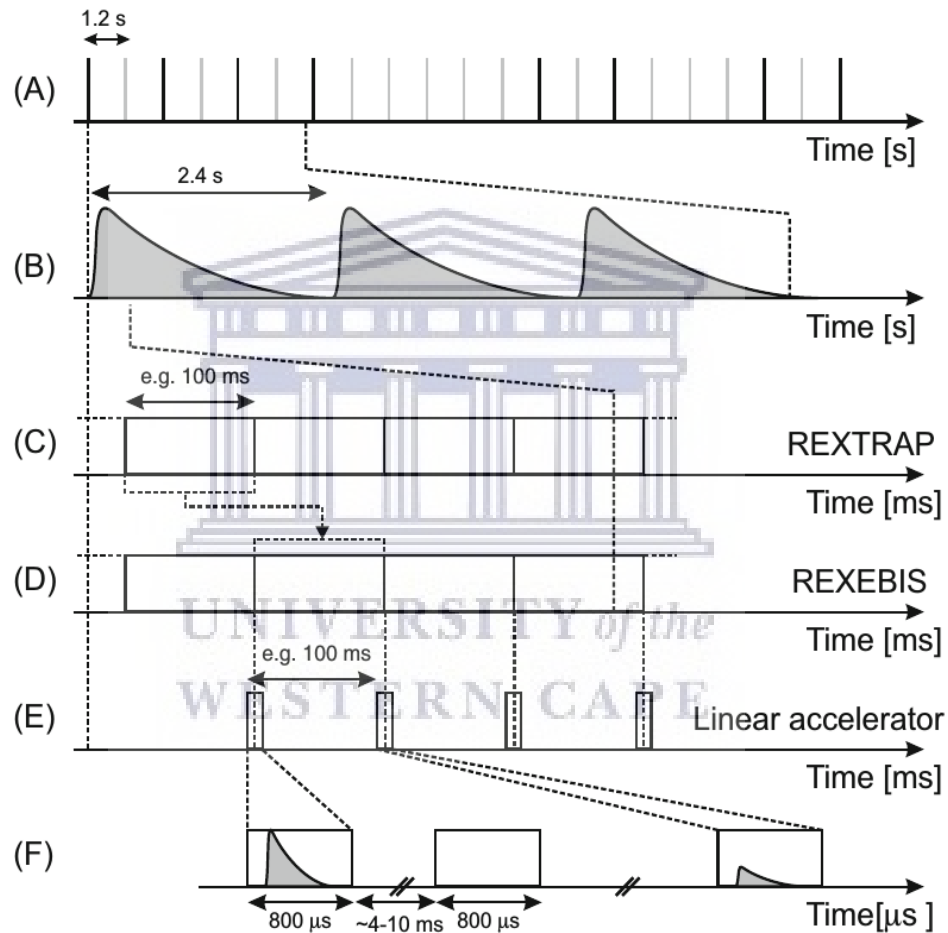
FIGURE 3.8: Time structure for the radioactive ion beam at CERN. See text for more details.

There are many factors that impact the time structure: the time of the delivered proton beam, the characteristic release of the target and ion source, the decay of the desired radioactive ions and the duty cycle of the bunching, breeding and accelerating devices. Timing signals are used to keep control over the entire sequence from proton impact to beam delivery at the experimental setup. The first signal (A) is available at the beginning of each super-cycle of the PSB. A super-cycle consists of a sequence of a

preset number of individual cycles of 1.2 s each. This signal is also used as a trigger for a shutter that blocks the laser if laser ionisation is used. In laser "on/off" mode the laser status is changed at each supercycle. In the supercycles with the shutter closed, only contaminants are detected and with the shutter open both contaminants and laser-ionised beam are detected. The shutter status is acquired in the data acquisition system and is used to sort data to determine the ratio of contaminants to the laser-ionised beam. The second signal (B) is sent when the proton beam makes impact with the ISOLDE primary target. The time difference between this signal and the detection of the beam at the experimental setup can be used to discriminate background or to identify contaminants. This is due to the fact that nuclei have characteristic lifetimes and release times. The third signal (C, D) is sent at the point when the ions are injected from REXEBIS into the REXLINAC. This signal is used to synchronise injection into the REXLINAC which ensures proper acceleration and transmission (E). This signal also facilitates a 1-ms long "ON beam" window used by the data acquisition system (DAQ) of the MINIBALL detection system (F).

3.2 MINIBALL

The MINIBALL array is comprised of eight triple cluster detectors which are mounted within the MINIBALL frame coupled with a target chamber. Figure 3.9 shows the MINIBALL clusters surrounding the target chamber used in this experiment. The target chamber houses the 4-mg/cm^2 ^{196}Pt target used in the CE experiment as well as the Double Sided Silicon Strip Detector (DSSSD) used to detect scattered particles.

The frame was designed to ensure maximum flexibility for positioning the MINIBALL clusters around the target chamber. The MINIBALL frame was built in two halves which can slide apart on rails to give access to the target chamber. The clusters are mounted on arms which allow for four degrees of freedom. The clusters are mounted on three toothed arcs which can be rotated about a vertical axis. These mountings are interlocked with the teeth of the arcs, allowing each cluster to be moved up and down in a controlled manner. The cluster mountings also consist of rods that enable the clusters to be moved in and out relative to the target. The clusters can also be rotated around their own axis on the mount. The degrees of freedom are illustrated in Figure 3.10.

Section 3.2.1 discusses the high-purity germanium detectors used for detecting γ rays. Section 3.2.2 details the particle detector used to detect scattered particles. Section 3.2.3 expands on the data acquisition system used to process the data collected during the experiment.
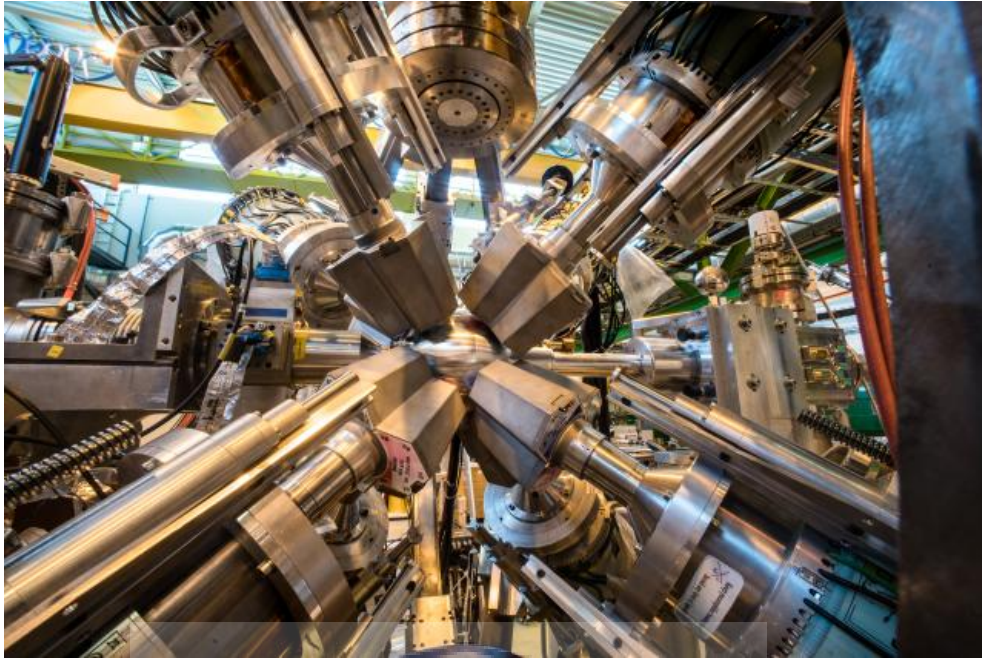
FIGURE 3.9: Target chamber used in the CE of ^{66}Ge surrounded by the triple cluster germanium detectors. Figure taken during the experiment in July 2017 [8].

3.2.1 High-Purity Germanium Detectors

The development of high-purity germanium (HPGe) detectors has allowed tremendous advances in nuclear physics and other fields. Germanium is an intrinsic semiconductor and can be made n- or p-type with the introduction of donor (lithium) or acceptor (boron) impurities. The removal of impurities allows the germanium to be almost completely depleted of charge carriers to allow the creation of large charge-sensitive regions. Each triple cluster detector contains three individually encapsulated six-fold segmented HPGe crystals. The germanium crystals are 78 mm long and have a diameter of 70 mm. The left panel of Figure 3.11 shows one of the triple cluster detectors. A total of 144 individual segment signals and an additional 24 signals from the central electrodes are measured. The high granularity of the system reduces the opening angle of the detection and therefore, enhances the position sensitivity [9]. This sensitivity to the interaction point is used to correct for Doppler shift of the detected γ rays. The energy resolution of the MINIBALL spectrometer after addback, measured with a ^{60}Co source, amounts to 2 to 3 keV at 1.332 MeV. This good energy resolution is achieved by operating the detector system at liquid nitrogen temperature. The signals from the detector system are processed using XIA digital gamma finders to enable high count rates and allow for proper event building [9].
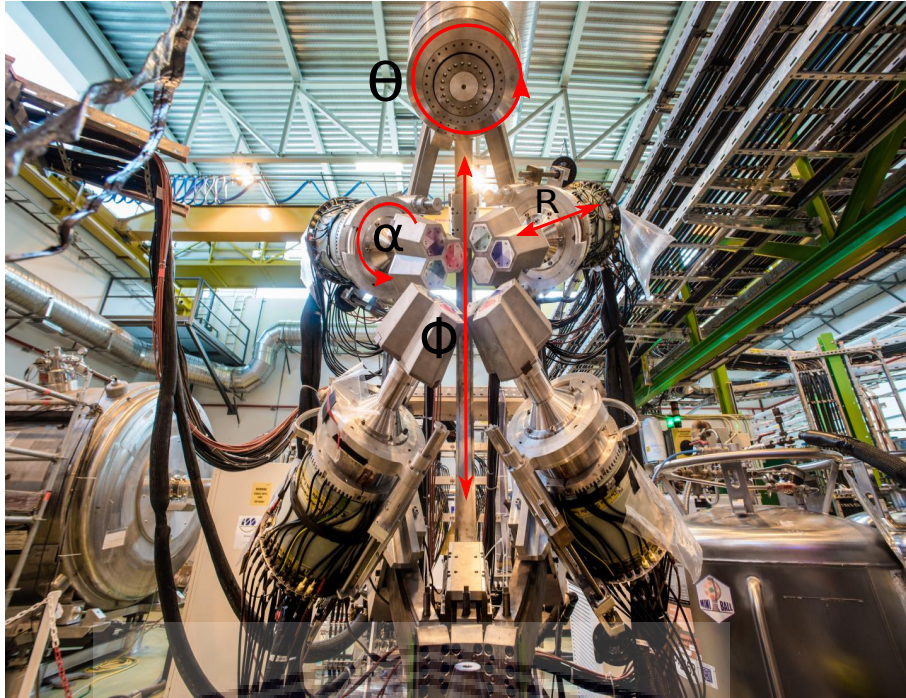
FIGURE 3.10: Four triple cluster detectors mounted on one half of the MINIBALL frame. The four degrees of freedom are marked. Figure adapted from [8].

3.2.2 Particle Detector

The angle of emission of the γ ray have to be combined with the momentum vector of the de-exciting emitting particle to perform Doppler correction. To measure the ion energy and position, a Double-Sided Silicon Strip Detector (DSSSD) was employed along with the eight triple cluster detectors. The DSSSD is composed of four identical quadrants that make up the CD-like structure. Figure 3.12 illustrates both sides of the DSSSD.

The thickness of each quadrant is 138 μm with a typical dead layer of 200 nm sufficient to stop heavy ion beams. The DSSSD has an inner diameter of 9 mm and an outer diameter of 40.9 mm. The front side is divided into 16 annular strips (p+n junction) and the back side is divided into 24 radial strips (n+n ohmic). The 16 rings on the front side have a pitch of 2.0 mm, while the 24 sectors on the back are arranged in 3.5° sectors with a 3.6° opening angle [63]. The 24 strips have been shorted allowing two consecutive strips to operate as one and thus resulting in 12 strips on the back. The azimuthal symmetry of the DSSSD allows for a simple relation with scattering angle, while the high granularity aids in the angular correlation of coincident γ rays allowing for a well-determined Doppler correction. The DSSSD was placed 27.34 mm downstream from the target with respect to the incoming beam and covered forward scattering angles between 19° to 56° in the laboratory frame. Figure 3.13 shows the DSSSD mounted in the target chamber.
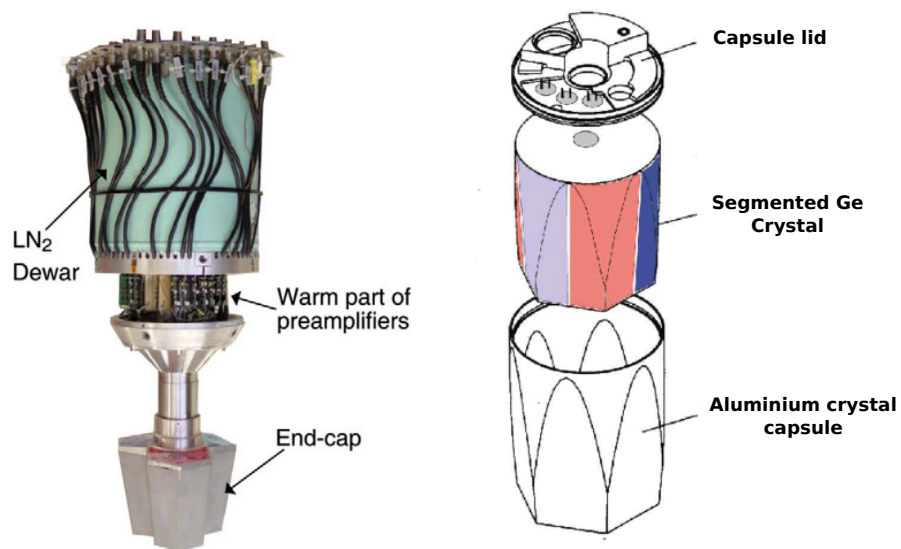
FIGURE 3.11: Single MINIBALL triple cluster detector connected to the liquid nitrogen dewar for cooling purposes (left) [9]. Exploded view of one of the segmented germanium crystals (right) [10].
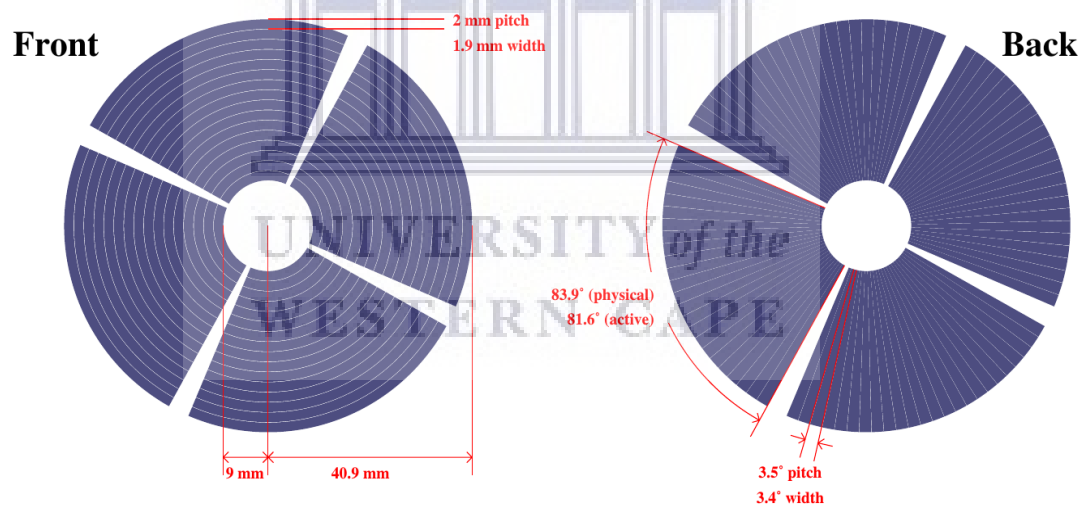
FIGURE 3.12: Schematic drawing of the double-sided strip detector. The front side has 0.1-mm inactive regions between the rings and the back side consists of 0.1° inactive regions between the strips.

3.2.3 Data Acquisition

The data acquisition system (DAQ) used to record events during the CE experiment is responsible for the collection and sorting of data. The DAQ is made up of both hardware and software elements. The hardware elements consist of Digital Gamma Finders 4C
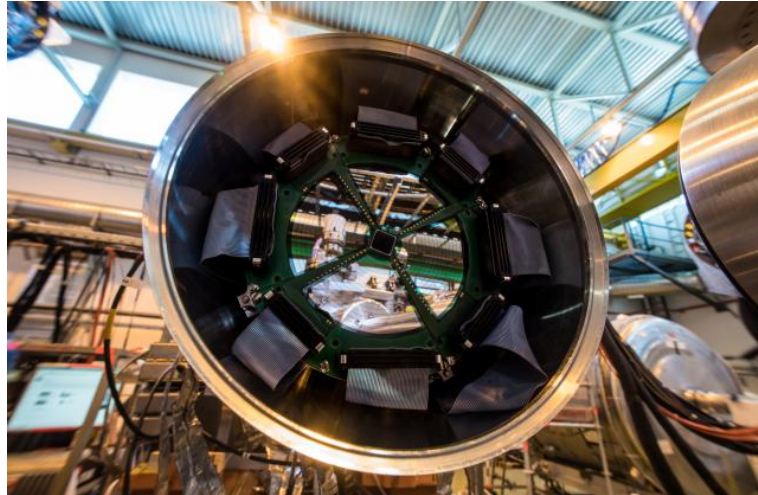
FIGURE 3.13: Picture of the DSSSD mounted in the target chamber showing the four quadrants and their 16 annular rings [8].

(DGF-4C), Mesytec 32 channel multiplexers (MUX-32) and peak sensing Analog-to-Digital Converters (ADC) used to collect the data from both γ rays and particles. The software element of the DAQ is called MAR_aBO_OU [11], which consists of the front end of Multi Branch System (MBS) readout, developed at GSI, Darmstadt, and the backend framework ROOT [64]. The data processing of MAR_aBO_OU is illustrated in Figure 3.14.
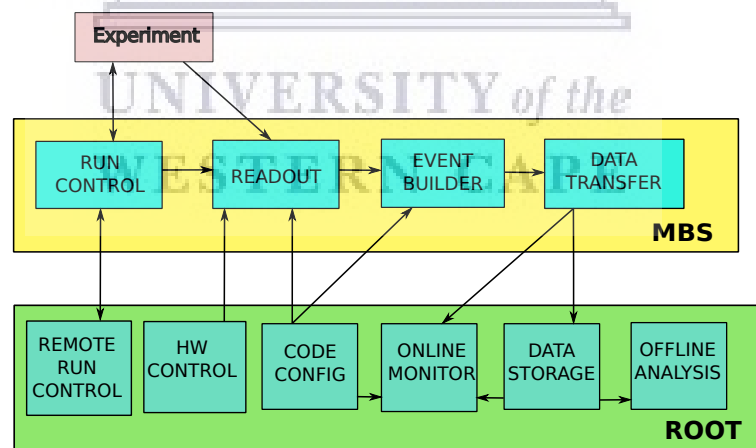
FIGURE 3.14: Schematic illustration of the data processing of MAR_aBO_OU. [11].

The MBS front end facilitates the data readout, event building and data transfer, whereas ROOT provides an environment to do setup configuration, run and hardware control, online/offline data visualisation using histograms, data analysis and data storage. The following tasks were handled by the DAQ during the experiment:

- Recording of the experimental data,

- Conversion of MBS events into Miniball Event Data (MED) format,

- Assign energy, position and timing information for each event,

- Online and offline visualisation of the physical data, and

- Store the event data into ROOT format for further post-processing.

Chapter 4

Data Analysis and Results

This chapter gives details about the calibration of the equipment used to record the data as well as post-processing of the data to determine the spectroscopic quadrupole moment for ^{66}Ge. The chapter starts by describing the detector calibration for both the DSSSD and HPGe triple cluster detectors in Section 4.1. Section 4.2 discusses Doppler correction, which is followed by details on particle-γ coincidence in Section 4.3. The chapter concludes with a discussion on the determination of the beam composition for the investigated beam produced at the ISOLDE facility in Section 4.4.

4.1 Detector Calibration

To accurately determine the spectroscopic quadrupole moment from the data, both the DSSSD and the HPGe triple cluster detectors have to be calibrated. Energy and efficiency calibrations for the HPGe crystals are performed using well-known calibration sources, whereas the DSSSD is calibrated using in-beam data since an alpha source does not sufficiently cover the energy range of the beam. The following sections discuss each of these in more detail.

4.1.1 HPGe Cluster Calibration

The calibration for the HPGe cluster crystals was performed using a combination of two calibration sources, namely ^{152}Eu and ^{133}Ba. The ^{133}Ba source provides low energy γ rays ranging from 80 to 384 keV whereas ^{152}Eu provides γ-ray transitions ranging from 122 keV up to 1.408 MeV. These proved sufficient to obtain an accurate calibration for the first 2^+ transition of ^{66}Ge at 956 keV. The two sources were mounted at the target position ensuring all the crystals of MINIBALL could detect the γ rays being emitted.

The energy calibration using the ^{152}Eu transitions only was found to be sufficient as it already provided lower energy γ rays. The recorded γ-ray spectrum is shown in Figure 4.1.
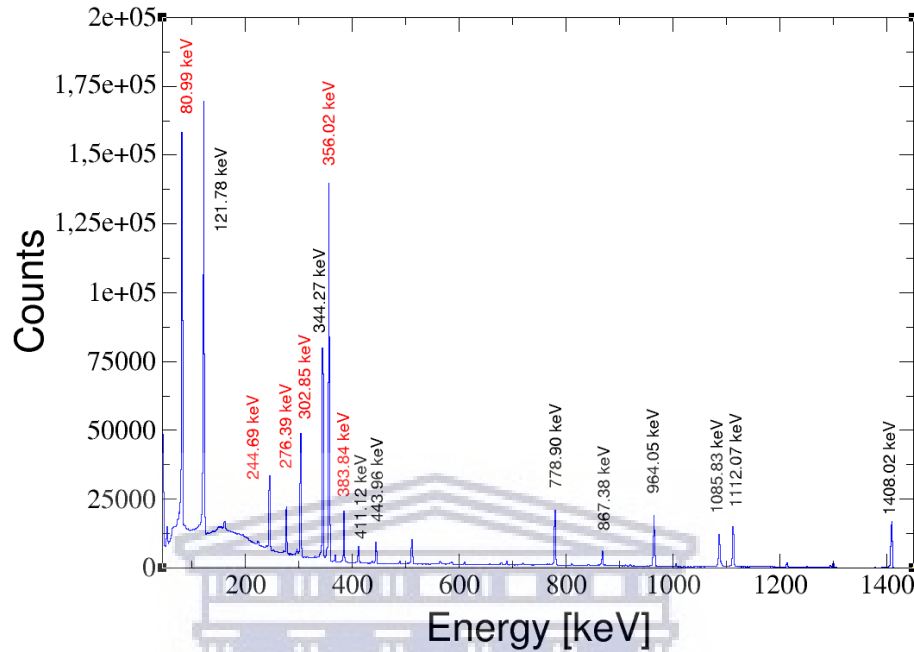
FIGURE 4.1: Spectrum of the ^{152}Eu and ^{133}Ba calibration sources used to calibrate the cluster detectors. Peaks with red labels belong to ^{133}Ba and those with black labels belong to ^{152}Eu.

A total of 16 dominant transitions were identified and are shown labelled in Figure 4.1. The energy calibration was performed for each of the 24 detectors of MINIBALL by fitting the 16 transitions in the core spectrum. A linear fit was performed to determine the calibration coefficients for that crystal. A fit for a single core along with the gain and offset obtained are presented in Figure 4.2.

In addition to the energy calibration, a detection efficiency calibration was also performed using the ^{152}Eu source. The efficiency fit was performed using the $gf3$ program that is part of the RadWare package [65]. $gf3$ takes as input the centroids, peak areas and peak energies as well as the errors of each of the strong transitions of ^{152}Eu and calculates their relative intensities before saving them to file. This new input file is used with EFFIT, another program in the RadWare package, to obtain the efficiency curve. EFFIT fits this data using the following expression:

$$\ln(\epsilon) = [\epsilon_l + \epsilon_h]^{-\frac{1}{G}}, \tag{4.1}$$
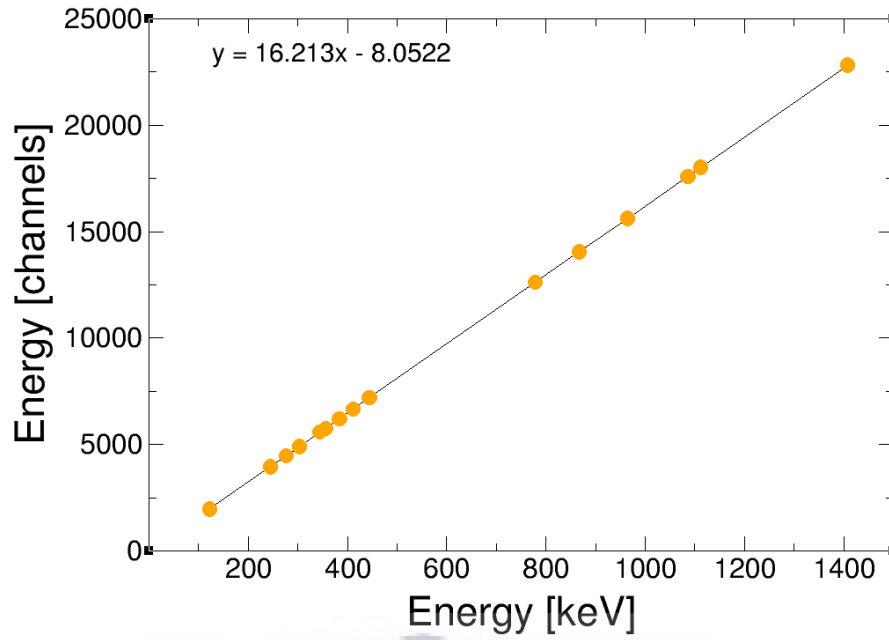
FIGURE 4.2: Linear fit to the ^{152}Eu data for one of the core of a cluster detector. The gain and offset are given in the equation of the linear fit.

where ϵ_l and ϵ_h denote the efficiencies of the low and high energy regions, respectively, and G is the interaction parameter between the two regions. The lower region ϵ_l is calculated as follows:

$$\epsilon_l = (A + Bx + Cx^2)^{-G}, \tag{4.2}$$

where A, B and C are the fitting parameters for the lower region of the γ-ray spectrum and $x = \log(\frac{E_\gamma}{E_1})$ with $E_1 = 100$ keV. Similarly, the higher region is calculated using

$$\epsilon_h = (D + Ey + Fy^2)^{-G}, \tag{4.3}$$

where D, E and F are the fitting parameters for the higher region and $y = \log(\frac{E_\gamma}{E_2})$ with $E_2 = 1$ MeV. The resulting efficiency curve and the fitting parameter values for EFFIT are shown in Figure 4.3.

4.1.2   DSSSD Energy Calibration

As aforementioned, the DSSSD is made up of four identical quadrants with 16 annular segments on the front side and 12 strips, perpendicular to the rings on the back side. This results in 768 individual pixels which are used to detect the scattering particles
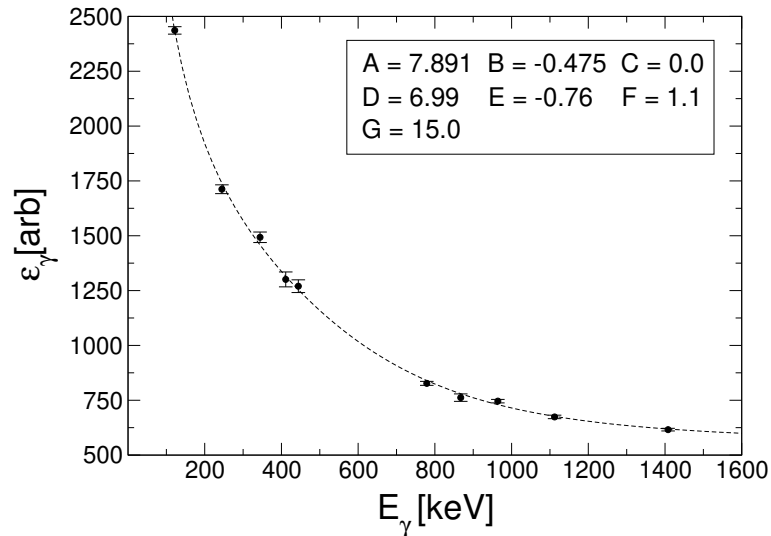
FIGURE 4.3: Relative detection efficiency of MINIBALL measured with ^{152}Eu at the target position. The fit was performed using EFFIT and the resulting fit parameters are shown.

with high position sensitivity. Each hit on a ring is recorded with a corresponding hit on a sector. Events on the front side of the DSSSD are subjected to energy shifts due to the kinematics and energy losses through the target, while events on the back side are recorded at the same energy. The beam energy amounts to 290 MeV in the laboratory frame, thus making a calibration with a typical alpha source insufficient due to large deviations resulting from extrapolation. The DSSSD was therefore calibrated using a cocktail beam, consisting of ^{12}C, ^{16}O, ^{20}Ne and ^{40}Ar, mass separated using $A/q = 4$ and bombarded onto a ^{196}Pt target. A spectrum of the cocktail beam is shown in Figure 4.4.

The target had a thickness of 1.4 mg/cm^2 and the beam energy was 5.54 MeV/u. For each of the nuclei in the cocktail beam, a kinematics calculation was done using the simulation program LISE++ [66]. LISE++ calculates the energy of the scattering nucleus after a scattering event with the target in question as well as the energy of the recoil for each ring in the DSSSD. The in-beam data for the cocktail beam give the channel number for the peaks of interest for each ring and thus, a calibration can be done. Figure 4.5 illustrates the kinematics curve for ^{16}O as it interacts with the ^{196}Pt target.

The calibrated spectra of each quadrant is shown in Figure 4.6, where an overlap of the peaks is seen at 240 MeV.
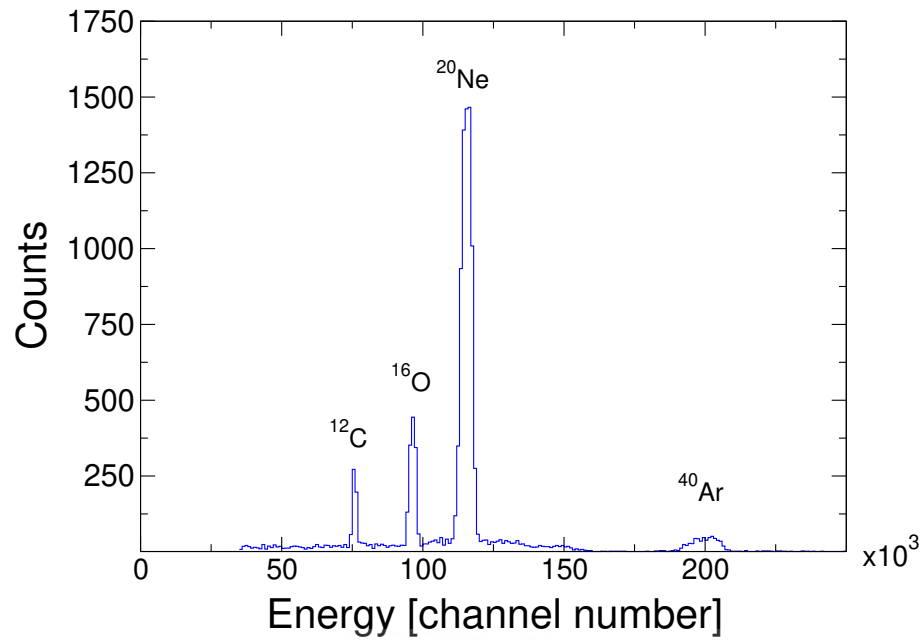
FIGURE 4.4: Spectrum of the cocktail beam used in the calibration of the DSSSD. Each of the components of the cocktail beam is labelled.
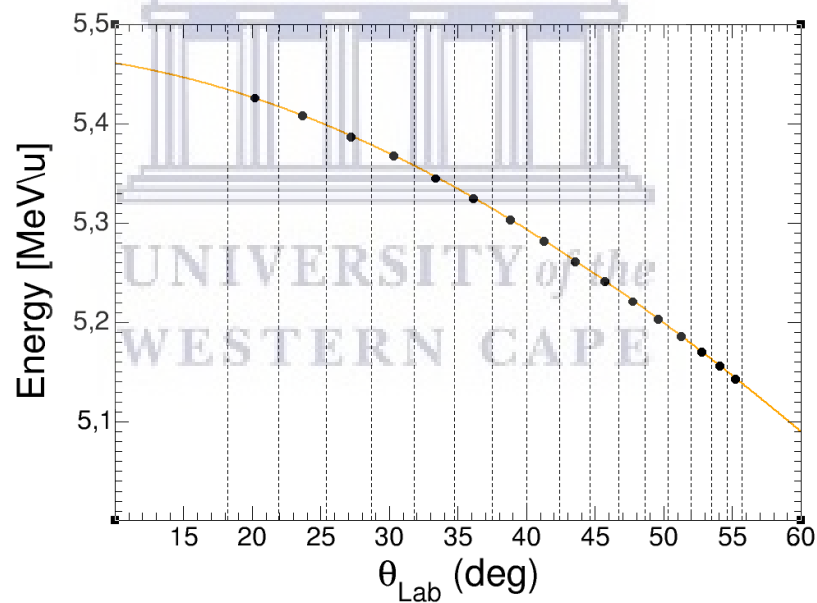
FIGURE 4.5: Kinematics curve obtained with LISE++ for ^{16}O onto ^{196}Pt as a function of scattering angle. The dashed line represents the angles that the different rings cover in the lab frame.

4.2 Doppler Correction

When performing CE experiments using high energy beams, the γ-ray energies have to be corrected due to the Doppler effect. For this experiment, a recoil velocity of $\beta \sim 10\%$
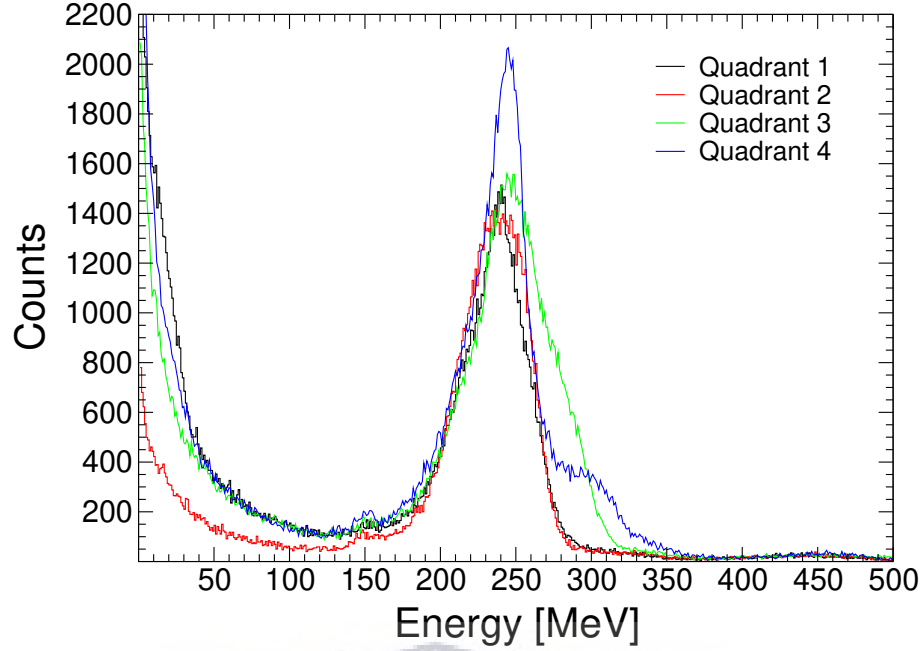
FIGURE 4.6: Calibrated ^{66}Ge spectra for each of the quadrants of the DSSSD at a beam energy of 290 MeV.

is observed. The γ rays are detected with a large Doppler broadening due to the high recoil velocity and the close configuration of the HPGe detectors of MINIBALL. The interaction position of the γ ray inside the HPGe crystals and the particle position within the DSSSD have to be known precisely to perform a proper correction. The correction of the γ-ray energies is given by

$$E_{\gamma,0} = \frac{E_{\gamma,lab}(1 + \beta\cos(\theta_{p\gamma}))}{\sqrt{1 - \beta^2}}, \tag{4.4}$$

where $E_{\gamma,lab}$ is the energy measured in the laboratory frame, $E_{\gamma,0}$ is the energy of the emitted γ ray in the rest frame and $\theta_{p\gamma}$ is the angle between the particle momentum vector and the direction of the emitted γ ray with

$$\cos(\theta_{p\gamma}) = \sin(\theta_{lab,\gamma})\sin(\theta_{lab,\gamma})\cos(\phi_{lab,p} - \phi_{lab,\gamma}) + \cos(\theta_{lab,\gamma})\cos(\theta_{lab,p}). \tag{4.5}$$

The observables $\theta_{lab,\gamma}$ and $\phi_{lab,\gamma}$ are the detected angles of the MINIBALL crystals and $\theta_{lab,p}$ and $\phi_{lab,p}$ are the detected angles of the DSSSD detectors. A high position sensitivity is achieved with MINIBALL using the granularity of the six-fold segmented triple cluster detectors which ensures an improved assignment of the interaction position within each HPGe.

In order to use the position sensitivity of MINIBALL, a position calibration measurement had to be performed. An independent experiment with a stable ^{22}Ne beam was performed which employs $d(^{22}\text{Ne},^{23}\text{Ne})p$ and $d(^{22}\text{Ne},^{23}\text{Na})n$ transfer reactions. The approach is as follows:

1. The position of each triple cluster detector can be described by a set of four parameters R_i, ϕ_i, θ_i and α_i as illustrated in Figure 4.7.

2. After the transfer reactions, the excited ^{22}Ne and ^{23}Na decay in flight by emitting γ rays which are collected by the HPGe detectors with a Doppler broadening. From the kinematics of the reaction, the scattering angles of the recoiling nuclei are small and negligible and thus, the energy shift depends solely on the position where the γ-ray was detected. For each segment, a set of the aforementioned parameters are determined to correct the γ-ray energies according to Equation 4.4.

3. To help facilitate this process, an algorithm that implements neural networks, written in ROOT by Nigel Warr was used. This algorithm uses the Doppler-shifted 440-keV γ-ray of the $d(^{22}\text{Ne},^{23}\text{Na})n$ reaction and minimises the width of the 440-keV γ-ray resulting in a set of the four parameters. These parameters are then used to compare the calculated γ-ray energies with the measured ones. A χ^2 minimisation fit is employed for this purpose.
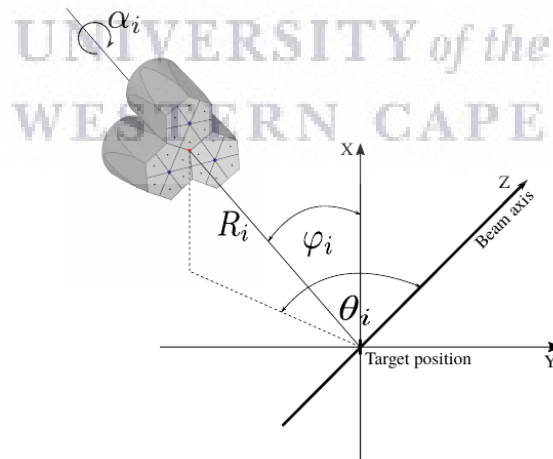
FIGURE 4.7: Parameters used to define the position of each triple cluster detectors with respect to the beam line.

The resulting parameter sets for each core is used to perform the final Doppler correction of the ^{66}Ge data. Table 4.1 shows the best fit parameters from the χ^2 minimisation.

TABLE 4.1: Position parameters used for the center of each MINIBALL triple cluster detector for the Doppler correction.

MB Cluster	R_i [mm]	θ_i [°]	ϕ_i [°]	α_i [°]
MB17	97.8	144.6	132.4	321.6
MB12	94.2	49.4	63.1	47.9
MB16	97.9	46.3	134.5	52.7
MB13	99.6	144.2	54.8	48.0
MB22	98.4	134.4	231.9	73.6
MB18	95.5	41.7	235.0	110.3
MB14	97.0	131.1	299.7	267.3
MB23	93.8	36.3	260.9	260.9

4.3 Particle-γ Coincidence

Due to the vast number of γ rays resulting from radioactive ion beam experiments, it is necessary to employ a particle-γ coincidence condition. This is especially important for Coulomb excitation experiments with radioactive ion beams, as the rare γ-ray transition of interest may be hidden behind the background. This background could result from the β decay of the radioactive ions implanted in the target chamber and along the beamline as well as bremsstrahlung from the accelerator. Figure 4.8 illustrates a raw γ-ray singles spectrum with the energy of the first 2^+ transition of ^{66}Ge marked. As can be seen, the transition of interest cannot be identified.
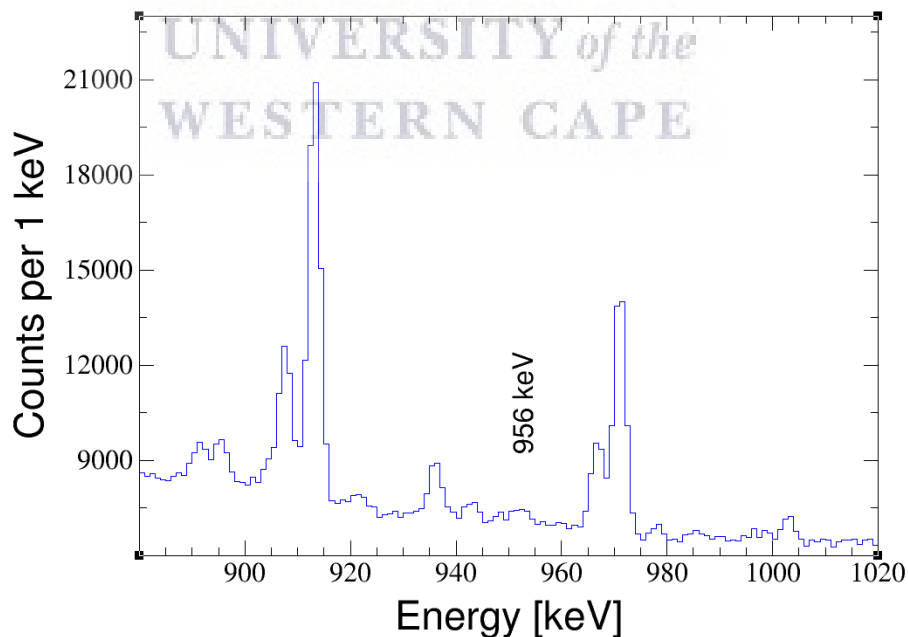
FIGURE 4.8: γ-ray singles spectrum for ^{66}Ge on ^{196}Pt with no particle-γ coincidence condition applied. The energy of the first 2^+ transition at 956 keV is marked.
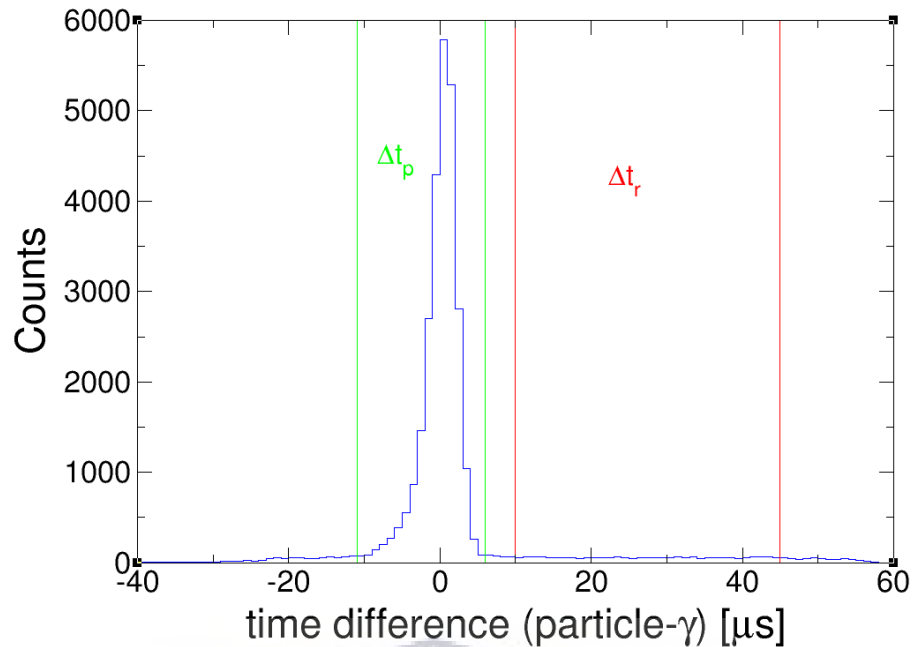
FIGURE 4.9: Time difference between the cluster detectors and the DSSSD. Prompt and random time windows are marked, which are used to generate the final γ-ray spectrum.

The particle-γ condition was set up by requiring a single detection in one of the HPGe cluster segments followed by a hit in both a ring and a sector of the DSSSD within an acceptance time window. The particle-γ condition also improves the peak-to-background ratio as any γ ray detected outside of the acceptance window is subtracted from the resulting particle spectrum. Only prompt γ rays which are detected within a $\Delta t_p = 160$ ns time window relative to the particle in the DSSSD are selected for the final γ-ray spectrum. A time window for the random γ rays Δt_r is also selected such that background can be determined and subtracted from the final γ-ray spectrum. Figure 4.9 shows the time difference acceptance windows for prompt and random γ rays used to generate the final particle-γ coincidences.

The resulting γ-ray spectrum from the prompt window gated on beam particles is shown in Figure 4.10. It should be noted that this spectrum is not Doppler-corrected.

The random γ-ray spectrum is subtracted from the resulting prompt spectrum and Doppler correction is applied. The final γ-ray spectrum is particularly clean from background radiation and mostly contains transitions caused by CE. Figure 4.11 shows the beam-gated background-subtracted spectrum for the ^{196}Pt target. Figure 4.12 shows the final beam-gated background-subtracted spectrum after applying Doppler correction, where the first 2^+ transition of ^{66}Ge at 956 keV can be clearly seen.
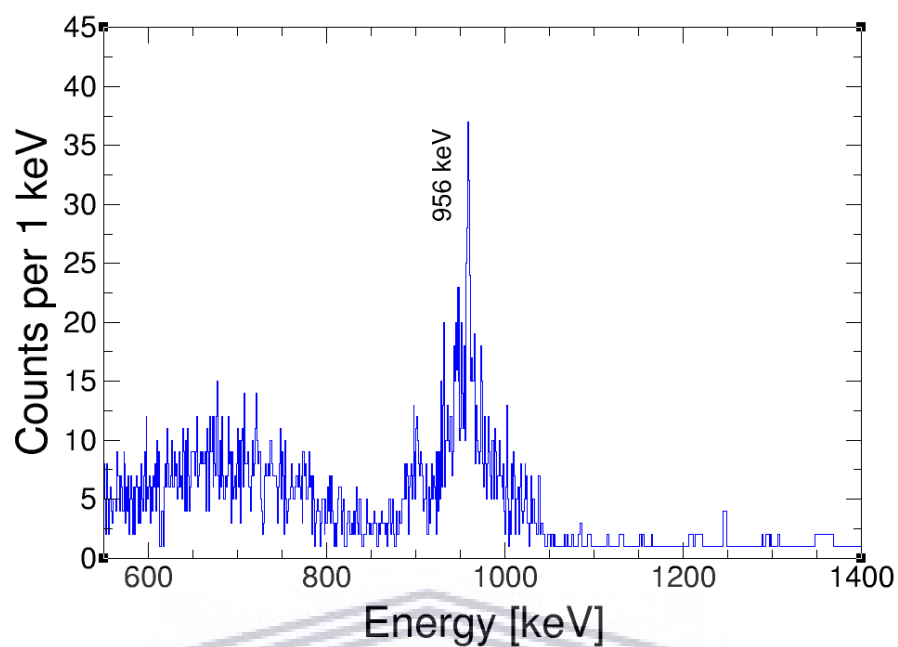
FIGURE 4.10: γ-ray spectrum from the prompt time window. The range of this spectrum was decreased to not include the 511 keV transition such that the first 2^+ state in ^{66}Ge can be seen.
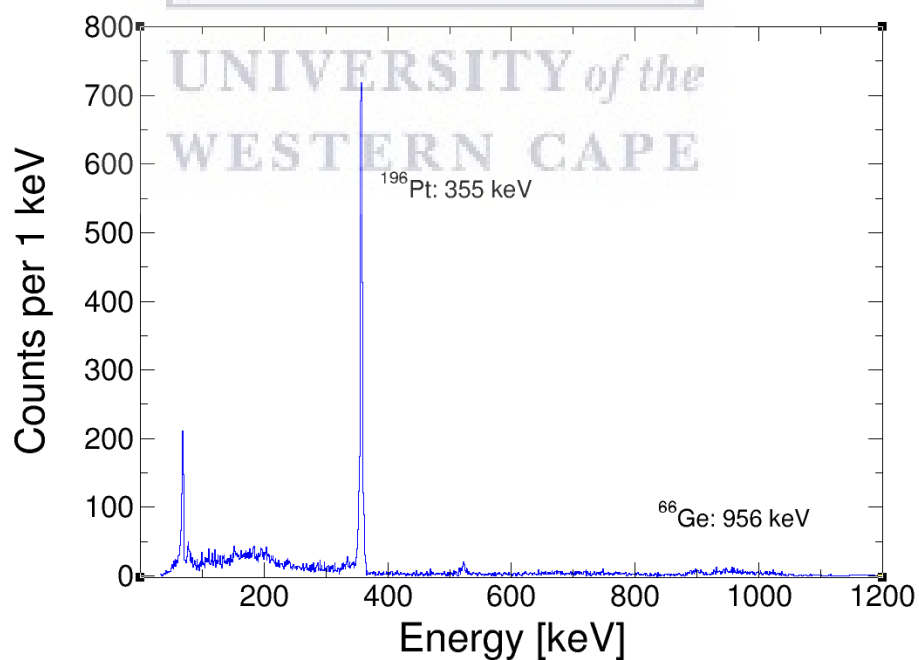
FIGURE 4.11: Beam-gated γ-ray spectrum after background subtraction. The first 2^+ state in ^{196}Pt is marked.
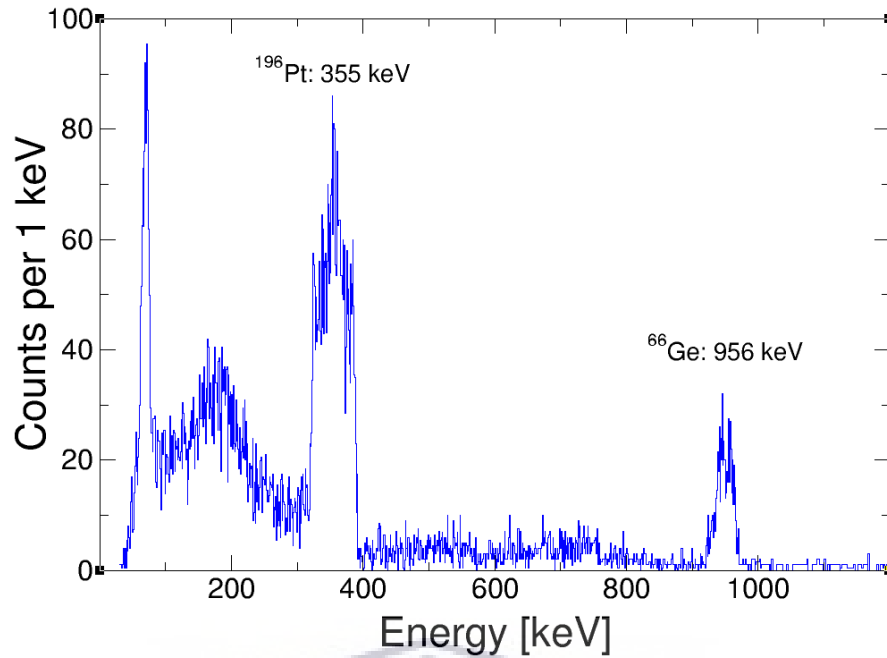
FIGURE 4.12: γ-ray spectrum after Doppler correction and background subtraction. The first 2^+ state in ^{66}Ge can clearly be seen.

4.4   Beam Composition

As previously mentioned in Section 3.1.1, the final beam used for the experiment contained both ^{66}Ge and ^{70}Se. To determine an accurate spectroscopic quadrupole moment for ^{66}Ge, the ratio of selenium to germanium has to be known precisely. As shown in Figure 4.13, potential beam contaminants are possible along the isobaric chains $A = 66$ as well as $A = 70$ since the mass separators are only selective to mass-over-charge ratio.

FIGURE 4.13: Nuclei along the isobaric chains $A = 66$ and $A = 70$ that could potentially contribute to the beam composition are marked with red squares.

The primary ISOLDE beam is extracted as a singly-charged molecule beam. In this case, ^{66}Ge^{32}S molecules and ^{70}Se^{12}C^{16}O molecules were produced resulting in possible contaminants from ions with $A = 98$. The transport from REXTRAP to REXEBIS is managed by an electrostatic steer-er and therefore, no A/q separation is possible at this stage. Mass $A = 66$ ions were charge bred in REXEBIS and extracted with charge state $q = 16^+$, which results in $A/q = 4.125$. Mass $A = 70$ ions were charge bred and extracted with charge state $q = 17^+$, resulting in $A/q = 4.118$. An ionisation chamber was set up before the experiment to estimate the target thickness as well as the beam composition. The ionisation chamber however was not biased properly and thus could not be used. A β-decay study of the beam had to be performed to determine the beam composition.

4.4.1 β-decay Investigation

After the experiment, an aluminium stopper foil was placed in the target wheel and bombarded with the beam for 5.5 hours and left to decay for 2 hours. The data acquisition was running during the entire 7.5 hour period. The first step to determine the beam composition is to identify the transition lines of the β-decay spectrum. Figure 4.14 shows the recorded single spectrum when bombarding the beam onto the stopper foil. The observed transition energies and the corresponding β decays are listed in Table 4.2. The majority of the observed transitions are known lines from the decays of ^{66}Ge $\rightarrow$ ^{66}Ga, ^{66}Ga $\rightarrow$ ^{66}Zn, ^{70}Se $\rightarrow$ ^{70}As, and ^{70}As $\rightarrow$ ^{70}Ge.

The fact that lines from the potassium decay ^{40}K $\rightarrow$ ^{40}Ar are observed indicates that transitions with intensities down to the natural background radiation are also identified. In addition, no transitions corresponding to the decay of mass $A = 98$ ions were observed. In order to deduce how much of the target excitation was induced by ^{66}Ge, the amount of ^{70}Se relative to ^{66}Ge has to be determined. This is required for the proper normalisation of the measured transition strength. The measured intensity of a transition N_γ is given by

$$N_\gamma = \frac{A_\gamma}{\epsilon_\gamma I_\gamma}, \tag{4.6}$$

where A_γ is the area of a peak in a γ-ray singles spectrum, ϵ_γ is the detection efficiency at the energy of the transition and I_γ is the published intensity of the transition. For the determination of the β-decay ratio, the dominant transitions at 381.85 keV (^{66}Ge $\rightarrow$ ^{66}Ga) and 426.15 keV (^{70}Se $\rightarrow$ ^{70}As) were used. The ^{66}Ga transition at 381.85 keV from the β decay of ^{66}Ge has an intensity of 28% [1]. Since this transition intensity
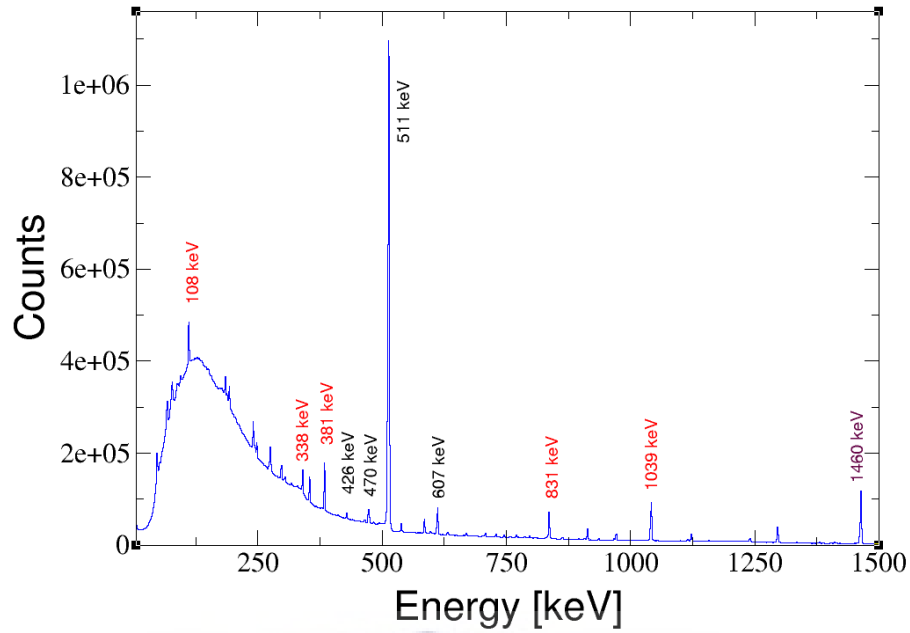
FIGURE 4.14: β-decay spectrum when bombarding the beam onto an aluminium stopper foil. γ-ray transitions with energies up to 1.5 MeV are observed.

was published without uncertainty, the maximum uncertainty reported for this decay of 0.8% is assumed. The ^{70}As transition at 426.15 keV from the β-decay of ^{70}Se has an intensity of 29% [1]. Since this transition intensity was published without uncertainty, the maximum uncertainty reported of 0.6% is assumed. The detection efficiency is determined from the curve in Figure 4.3. During the implantation at a rate R, the number of nuclei N grows as a function of time t, with the initial condition $N(0) = 0$ as follows:

$$\frac{dN}{dt} = R - \lambda N(t), \tag{4.7a}$$

$$N(t) = \frac{R}{\lambda}(1 - e^{-\lambda t}), \tag{4.7b}$$

where λ is the decay constant equal to $\ln(2)/t_{1/2}$. The activity A is then defined as

$$A(t) = \lambda N(t) = R(1 - e^{-\lambda t}). \tag{4.8}$$

TABLE 4.2: Observed γ-ray transition energies following the corresponding β decay.

E_γ [keV]	β-decay	E_γ [keV]	β-decay	E_γ [keV]	β-decay
44	^{66}Ge $\to$ ^{66}Ga	743	^{70}As $\to$ ^{70}Ge	1508	^{66}Ga $\to$ ^{66}Zn
65	^{66}Ge $\to$ ^{66}Ga	757	^{66}Ge $\to$ ^{66}Ga	1522	^{70}As $\to$ ^{70}Ge
108	^{66}Ge $\to$ ^{66}Ga	796	^{66}Ga $\to$ ^{66}Zn	1539	^{70}As $\to$ ^{70}Ge
182	^{66}Ge $\to$ ^{66}Ga	833	^{66}Ga $\to$ ^{66}Zn	1587	^{70}As $\to$ ^{70}Ge
190	^{66}Ge $\to$ ^{66}Ga	858	^{70}Se $\to$ ^{70}As	1707	^{70}As $\to$ ^{70}Ge
244	^{70}Se $\to$ ^{70}As	893	^{70}As $\to$ ^{70}Ge	1780	^{70}As $\to$ ^{70}Ge
272	^{66}Ge $\to$ ^{66}Ga	906	^{70}As $\to$ ^{70}Ge	1872	^{66}Ga $\to$ ^{66}Zn
293	^{70}Se $\to$ ^{70}As	935	^{66}Ge $\to$ ^{66}Ga	1898	^{66}Ga $\to$ ^{66}Zn
302	^{66}Ge $\to$ ^{66}Ga	963	^{66}Ga $\to$ ^{66}Zn	1918	^{66}Ga $\to$ ^{66}Zn
338	^{66}Ge $\to$ ^{66}Ga	1039	^{66}Ga $\to$ ^{66}Zn	2019	^{70}As $\to$ ^{70}Ge
381	^{66}Ge $\to$ ^{66}Ga	1114	^{70}As $\to$ ^{70}Ge	2189	^{66}Ga $\to$ ^{66}Zn
426	^{70}Se $\to$ ^{70}As	1120	^{66}Ge $\to$ ^{66}Ga	2292	^{66}Ga $\to$ ^{66}Zn
470	^{66}Ge $\to$ ^{66}Ga	1232	^{66}Ga $\to$ ^{66}Zn	2422	^{66}Ga $\to$ ^{66}Zn
536	^{66}Ge $\to$ ^{66}Ga	1333	^{66}Ga $\to$ ^{66}Zn	2449	^{70}As $\to$ ^{70}Ge
595	^{70}As $\to$ ^{70}Ge	1338	^{70}As $\to$ ^{70}Ge	2751	^{66}Ga $\to$ ^{66}Zn
607	^{70}As $\to$ ^{70}Ge	1356	^{66}Ga $\to$ ^{66}Zn	2933	^{66}Ga $\to$ ^{66}Zn
639	^{66}Ge $\to$ ^{66}Ga	1387	^{66}Ga $\to$ ^{66}Zn	3229	^{66}Ga $\to$ ^{66}Zn
662	^{66}Ge $\to$ ^{66}Ga	1411	^{70}As $\to$ ^{70}Ge	3256	^{66}Ga $\to$ ^{66}Zn
668	^{70}As $\to$ ^{70}Ge	1418	^{66}Ga $\to$ ^{66}Zn	3380	^{66}Ga $\to$ ^{66}Zn
705	^{66}Ge $\to$ ^{66}Ga	1460	^{40}K $\to$ ^{40}Ar	3422	^{66}Ga $\to$ ^{66}Zn
719	^{66}Ga $\to$ ^{66}Zn	1495	^{70}As $\to$ ^{70}Ge		

After the beam delivery is stopped at $t = t_{off}$, the number of nuclei decays as

$$dN = -\lambda N(t)dt, \tag{4.9a}$$

$$N(t) = N(t = t_{off})e^{-\lambda t}. \tag{4.9b}$$

The duty factor is defined as the ratio of the number of nuclei which have decayed to the number of nuclei which have been delivered as a function of time. From Equations 4.7b and 4.9b, the duty factors for the implantation and decay periods are given, respectively, by

$$DF_{t_{on}} = \frac{N_{decay}}{N_{delivered}} = \frac{N(t = t_{on}) - N(t)}{N(t = t_{on})} = 1 - \frac{1}{\lambda t}(1 - e^{-\lambda t_{on}}), \tag{4.10}$$

$$DF_{t_{off}} = \frac{N_{decay}}{N_{delivered}} = \frac{N(t = t_{on}) - N(t)}{N(t = t_{on})} = 1 - e^{-\lambda t_{off}}. \tag{4.11}$$
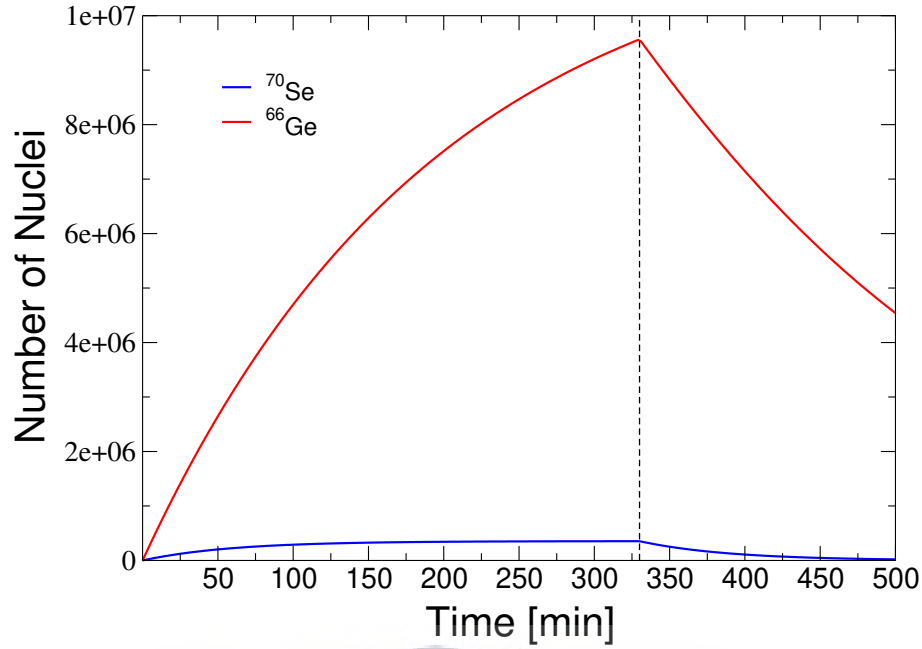
FIGURE 4.15: Number of nuclei as a function of time for ^{66}Ge ($t_{1/2} = 2.26$ h) and ^{70}Se ($t_{1/2} = 41$ min) for beam intensity $R = 1000$ and $N_{Ge}(t = 0) = N_{Se}(t = 0) = 0$. The beam is on from $t = 0$ to 330 min.

The total duty factor is the sum of the duty factors for the implantation and decay periods, corrected for the decays during the implantation period:

$$DF = DF_{t_{on}} + (1 - DF_{t_{on}})DF_{t_{off}}.$$ (4.12)

The ratio of ^{66}Ge to ^{70}Se nuclei in the beam is then defined as

$$\frac{f_{Ge}}{f_{Se}} = \frac{N_{\lambda,Ge}/DF_{Ge}}{N_{\lambda,Se}/DF_{Se}}.$$ (4.13)

From this ratio, the fraction of ^{66}Ge in the beam can be extracted as

$$f_{Ge} = 1 - \frac{1}{1 + (f_{Ge}/f_{Se})} = 0.91 \pm 0.12.$$ (4.14)

This number is in agreement with the ^{66}Ge:^{70}Se ratio of 10:1 ($\sim 90\%$) measured at the tape station at ISOLDE during the experiment.

4.5   Extracting Nuclear Structure Information

In CE experiments, the γ-ray intensities corresponding to the scattering of the collision partners are a direct observable. The matrix elements that couple these transitions are not a direct observable and occur as correlated parameters when fitting γ-ray intensity data. The integrated yields for the $2_1^+ \rightarrow 0_1^+$ transitions in ^{66}Ge and ^{196}Pt were calculated using the semi-classical couple-channel Coulomb-excitation least-squares code GOSIA. The calculation was performed using known spectroscopic information such as level lifetimes, branching ratios and matrix elements. The GOSIA files used in the calculation are shown in Appendix A. The level scheme of ^{66}Ge which was used to perform the GOSIA calculations is shown in Figure 4.16.
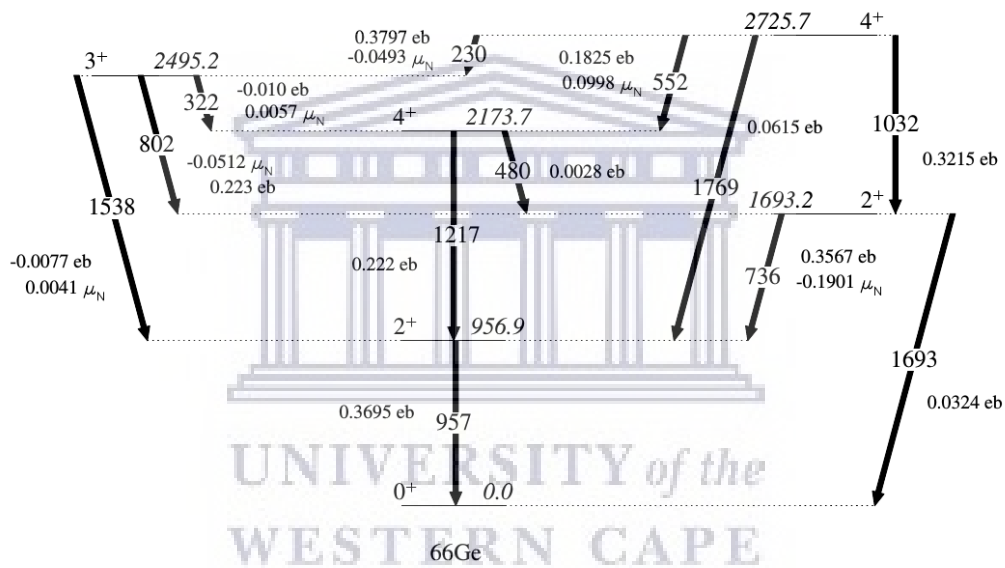
FIGURE 4.16: Level scheme used in the GOSIA calculations for ^{66}Ge along with the γ-ray energies and matrix elements used in the calculation. See text for more details.

For ^{66}Ge, the $\langle 2_1^+ || E2 || 0_1^+ \rangle$, $\langle 2_2^+ || E2 || 2_1^+ \rangle$, $\langle 2_2^+ || M1 || 2_1^+ \rangle$ and $\langle 2_2^+ || E2 || 0_1^+ \rangle$ matrix element was determined from the adopted $B(E2)$ values reported in the NNDC. The remaining E2 matrix elements were determined using Equation 1.6. The M1 matrix element from the 3^+ state at 2495.2 keV to the 2^+ at 1693.2 keV was determined using the rotor model E2 value along with reported mixing ratio of -2.91 and the mixing ratio value expression given by,

$$\delta(\frac{E2}{M1}) = 0.835 E_\gamma (MeV) = \frac{\langle I_f || M(E2) || I_i \rangle}{\langle I_f || M(M1) || I_i \rangle}. \tag{4.15}$$

The diagonal matrix elements and the M1 matrix elements, for which a mixing ratio has not been reported, were allowed to vary over a large range in GOSIA and the values giving the lowest χ^2 value were used. Although only the first 2^+ state in ^{66}Ge was observed during this experiment, the known levels and matrix elements up to the 4^+ level at 2725.7 keV was implemented in GOSIA. The 4^+ level serves as a buffer state to ensure a proper excitation and de-excitation mechanism by avoiding non-physical population and feeding of the underlying levels. The level scheme of ^{196}Pt that was used to perform the GOSIA calculations is shown in Figure 4.17. The matrix elements are given in TABLE 4.3.
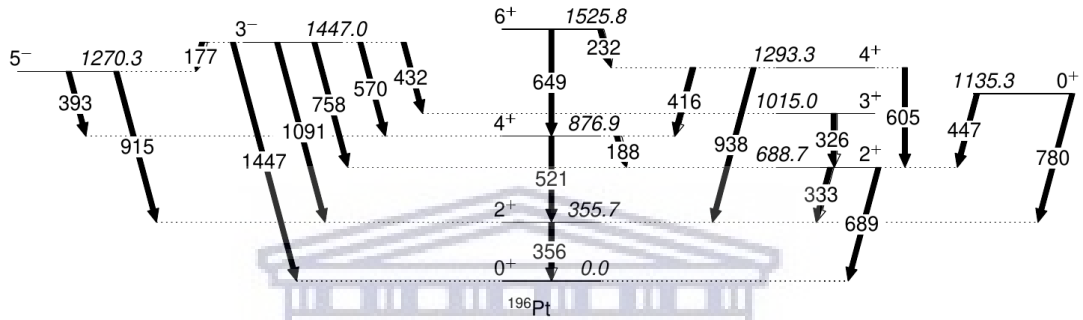
FIGURE 4.17: Level scheme used in the GOSIA calculations for ^{196}Pt along with the known γ-ray energies. See text for more details.

The $\langle 2_1^+ || E2 || 0_1^+ \rangle$, $\langle 2_1^+ || E2 || 2_1^+ \rangle$ and $\langle 4_1^+ || E2 || 4_1^+ \rangle$ matrix elements were taken from Ref [67]. The $\langle 4_2^+ || E2 || 4_1^+ \rangle$ matrix element is taken from Ref [68] and the $\langle 4_2^+ || M1 || 4_1^+ \rangle$ matrix element is calculated using Equation 4.15 with a mixing ratio of $\delta = -3.3$ [68]. The remaining E2 as well as the E3 and E1 matrix elements are calculated using the $B(E\lambda)$ values determined by the authors of Ref [69] with Equation 1.6. The $\langle 2_2^+ || M1 || 2_1^+ \rangle$ matrix element along with a mixing ratio of $\delta = -5.2$ is known from Ref [69], and was used to determine the $\langle 2_2^+ || E2 || 2_1^+ \rangle$ matrix element. The M2 matrix elements are determined using the $B(M2)$ values reported for the 3^- state at 1447.3 keV given in the NNDC [1].

The effects of higher-lying states in ^{66}Ge were estimated using GOSIA by varying the $\langle 2_1^+ || E2 || 2_1^+ \rangle$ matrix element and checking the percentage difference on the $B(E2)$ and $Q_s(2^+)$ values. The percentage difference was determined to be 1% and is considered in the error analysis. Figure 4.18 shows the experimental and theoretical beam-gated heavy-ion angular distributions integrated per 4 rings for the $2_1^+ \rightarrow 0_1^+$ transition for ^{66}Ge (left) and ^{196}Pt (right). Figure 4.19 shows the experimental and theoretical target-gated angular distributions integrated per 3 rings for the same transition.

The theoretical yields were calculated using $\langle 0_1^+ || E2 || 2_1^+ \rangle = 0.4826$ eb and $\langle 2_1^+ || E2 || 2_1^+ \rangle = 0.562$ eb, which were determined during this experiment. The theoretical yields were
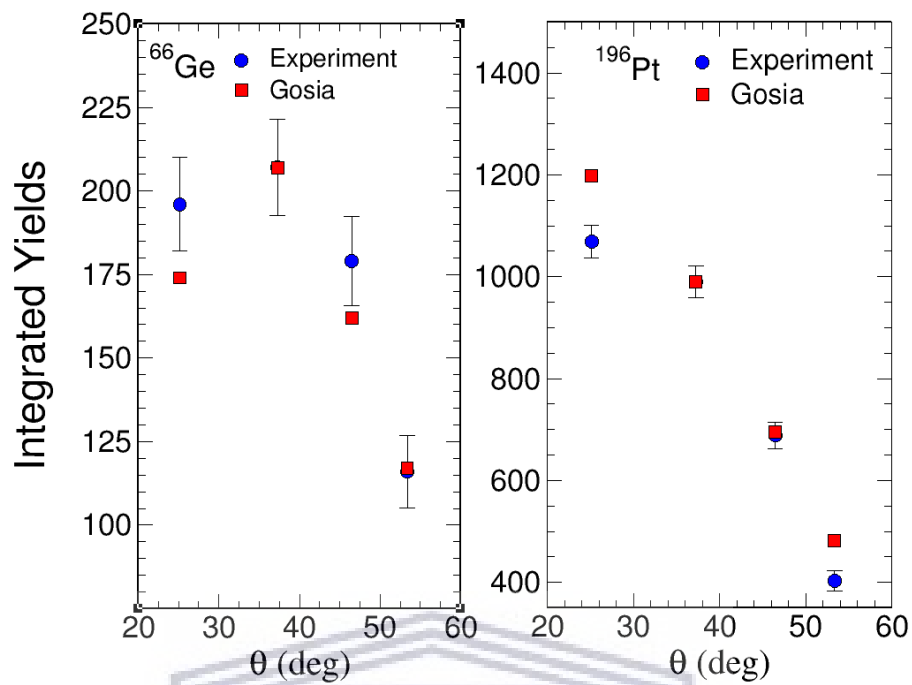
FIGURE 4.18: Beam-gated heavy-ion angular distributions showing experimental and calculated γ-ray yield integrated per 4 rings as a function of laboratory scattering angle θ for the de-excitation of the 2^+ states in ^{66}Ge (left) and ^{196}Pt (right).
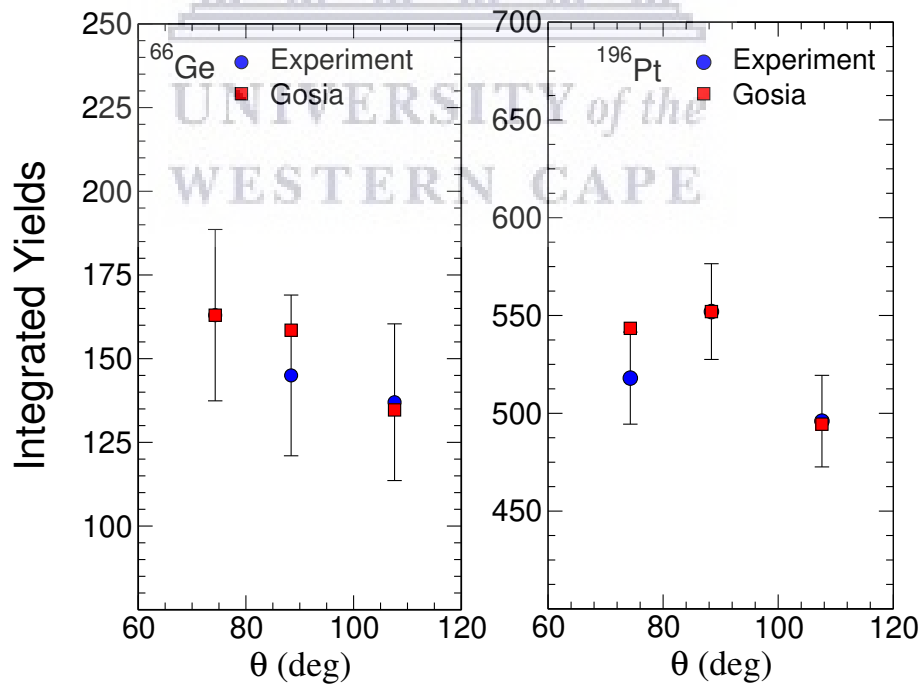
FIGURE 4.19: Target-gated heavy-ion angular distributions showing experimental and calculated γ-ray yield integrated per 3 rings as a function of laboratory scattering angle θ for the de-excitation of the 2^+ states in ^{66}Ge (left) and ^{196}Pt (right).

TABLE 4.3: Table presenting the matrix elements for ^{196}Pt used in the GOSIA2 calculations. See text for more details.

Multipolarity					
E1	E_i [keV]	E_f [keV]	J_i^π	J_f^π	$\langle J_i^\pi||E1||J_f^\pi\rangle$ [eb$^{1/2}$]
	1447.0	355.7	3^-	2^+	1.52×10^{-4}
	1447.0	688.7	3^-	2^+	1.17×10^{-4}
	1447.0	876.9	3^-	4^+	8.72×10^{-5}
	1270.3	876.9	5^-	4^+	1.8×10^{-4}
E2	E_i [keV]	E_f [keV]	J_i^π	J_f^π	$\langle J_i^\pi||E2||J_f^\pi\rangle$ [eb]
	355.7	gs	2^+	0^+	1.1697
	688.7	gs	2^+	0^+	3.7×10^{-4}
	355.7	355.7	2^+	2^+	0.8179
	688.7	355.7	2^+	2^+	1.3522
	876.9	355.7	4^+	2^+	1.9109
	1135.3	355.7	0^+	2^+	0.1381
	1293.3	355.7	4^+	2^+	0.1846
	688.7	688.7	2^+	2^+	0.5146
	1015.0	688.7	3^+	2^+	0.4960
	1135.3	688.7	0^+	2^+	0.3472
	1293.3	688.7	4^+	2^+	1.3406
	876.9	876.9	4^+	4^+	0.084
	1293.3	876.9	4^+	4^+	1.0121
	1525.8	876.9	6^+	4^+	2.5333
	1447.3	1270.3	3^-	5^-	1.3406
E3	E_i [keV]	E_f [keV]	J_i^π	J_f^π	$\langle J_i^\pi||E3||J_f^\pi\rangle$ [eb$^{3/2}$]
	1447.3	gs	3^-	0^+	0.307
	1270.3	355.7	5^-	2^+	0.2603
M1	E_i [keV]	E_f [keV]	J_i^π	J_f^π	$\langle J_i^\pi||M1||J_f^\pi\rangle$ [$\mu_N b^{-1/2}$]
	688.7	355.7	2^+	2^+	-0.072
	1015.0	355.7	3^+	2^+	-0.00968
	1015.0	876.9	3^+	4^+	-0.02925
	1293.3	876.9	4^+	4^+	-0.34382
M2	E_i [keV]	E_f [keV]	J_i^π	J_f^π	$\langle J_i^\pi||M2||J_f^\pi\rangle$ [$\mu_N b^{1/2}$]
	1447.3	876.9	3^-	4^+	1.184
	1447.3	1015.0	3^-	3^+	3.18

normalised to the experimental yields using a common normalisation factor. As can be seen in the figures, the trend of the angular distribution produced by GOSIA is in agreement with the experimental yields.

The normalisation procedure used in Refs [70, 71] was applied to determine the $\langle 2_1^+||E2||2_1^+\rangle$ matrix element. Coulomb excitation curves are determined in the $\langle 2_1^+||E2||2_1^+\rangle - \langle 2_1^+||E2||0_1^+\rangle$ plane by fixing $\langle 2_1^+||E2||2_1^+\rangle$ in steps of 0.01 eb, and varying $\langle 2_1^+||E2||0_1^+\rangle$ until converging with the experimental intensity ratio between the target and the projectile. The intensity ratio is given by

$$\frac{I_\gamma^T}{I_\gamma^P} = \frac{\sigma_{E2}^T W(\vartheta)^T}{\sigma_{E2}^P W(\vartheta)^P} = 0.915 \frac{N_\gamma^T \varepsilon_\gamma^P}{N_\gamma^P \varepsilon_\gamma^T}, \tag{4.16}$$

where ε_γ^P and ε_γ^T are the relative detection efficiencies for the target and projectile, respectively, $W(\vartheta)$ is the integrated angular distribution of the de-excited γ rays in coincidence with the inelastic scattered particle, and the factor 0.915 accounts for the 97.25% enrichment of the ^{196}Pt target chosen for normalisation and the beam composition of 89% between ^{66}Ge and ^{70}Se. The normalisation of the cross sections in ^{66}Ge to the cross sections in the target nucleus minimises systematic effects such as dead time and pile up. Section 4.5.1 details how the $B(E2)$ value was extracted and Section 4.5.2 discusses the determination of Q_S.

4.5.1 Determination of the $\langle 2_1^+||E2||0_1^+ \rangle$ transitional matrix element and the $B(E2; 2_1^+ \to 0_1^+)$ value

The $\langle 2_1^+||E2||0_1^+ \rangle$ matrix element was determined using the beam-gated data at forward angles (18.2° to 56.2°). The angular range is safe from nuclear interaction contributions with a separation between nuclear surfaces of more than 5 fm as given by Cline's criterion. Figure 4.20 shows the Coulomb cross section and excitation probability over the range of angles covered by the DSSSD in the laboratory frame.

This range of angles is not sensitive to the quadrupole moment. The difference in $Q_S(2^+)$ between 0.0 and 0.5 eb amounts to a 5% difference in the value of the $B(E2)$ which was taken into account during the error analysis. Figure 4.21 depicts the beam-gated non-Doppler-corrected spectra from which the yields of the ^{196}Pt were determined. Figure 4.22 shows the beam-gated Doppler-corrected spectra from which the yields for the scattered ^{66}Ge particles were determined.

The relative efficiencies, $\varepsilon_\gamma^P = 733(50)$ and $\varepsilon_\gamma^T = 1431(33)$, and total counts of $N_\gamma^P = 707(26)$ and $N_\gamma^T = 3313(57)$ for the beam-gated 355- and 956.9-keV transitions, yield an intensity ratio $\frac{I_\gamma^T}{I_\gamma^P} = 2.19(5)$. A value of $Q_S(2^+) = 0.33$ eb was calculated from the currently accepted $B(E2; 2_1^+ \to 0_1^+) = 16.9(14)$ W.u. This yields $\langle 2_1^+||E2||2_1^+ \rangle = 0.435$ eb, which was used in the GOSIA calculations. The $\langle 2_1^+||E2||2_1^+ \rangle$ matrix element was kept constant while incrementing $\langle 2_1^+||E2||0_1^+ \rangle$ in steps of 0.05 eb until the intensity ratio in Equation 4.16 converged. This yields $\langle 2_1^+||E2||0_1^+ \rangle = 0.483(15)$ eb giving a $B(E2; 2_1^+ \to 0_1^+) = 29.4(30)$ W.u. The quoted error on this measurement comes from the 1σ loci limits which is a 5% contribution, the quadrupole moments dependence on $B(E2; 2_1^+ \to 0_1^+)$ which is a 3% contribution, and the effects of higher-lying states on $B(E2; 2_1^+ \to 0_1^+)$ accounting for 1%, all added in quadrature.
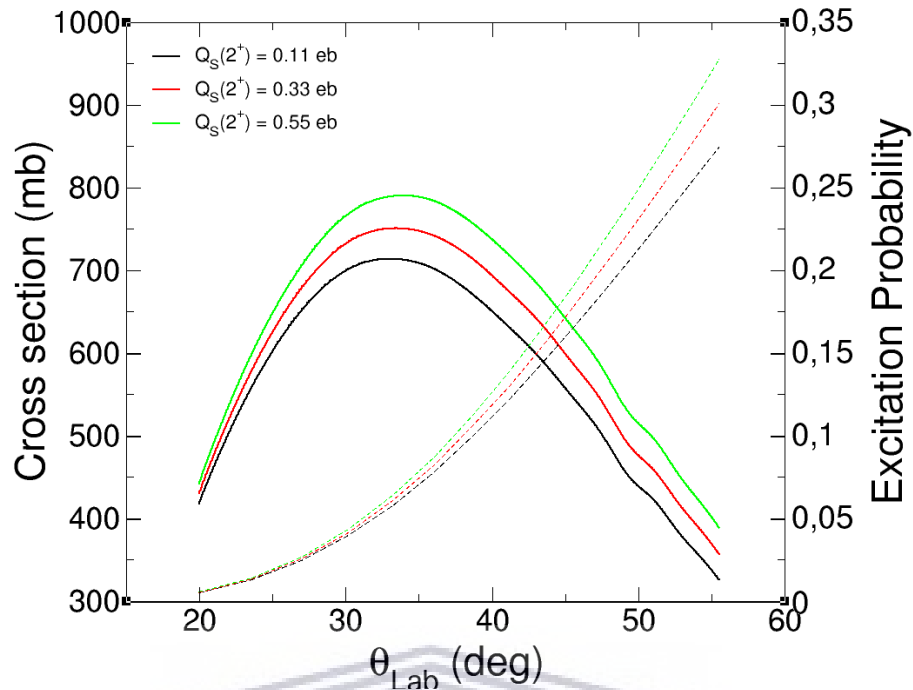
FIGURE 4.20: Coulomb cross section and excitation probability versus the laboratory angles covered by the DSSSD. The cross section and excitation probability were calculated using GOSIA.

4.5.2 Determination of the $\langle 2_1^+||E2||2_1^+\rangle$ diagonal matrix element and the $Q_S(2_1^+)$ value

The spectroscopic quadrupole moment $Q_s(2^+)$ was determined using the target-gated data at the recoil angles. The angular range covered by the recoiling target particles was determined by the kinematics of the reaction. Figure 4.23 shows the scattered projectile angles as a function of the recoiling target particle angles for ^{66}Ge bombarding a ^{196}Pt target at 290.07 MeV.

In the Laboratory frame, The recoiling ^{196}Pt target nuclei in the 18.2° to 56.2° range correspond to scattered ^{66}Ge projectiles in the 52.1° to 128.1° range. Since there are no detectors at backward angles with MINIBALL, the backwards angles can be inferred from the detection of the recoil and the knowledge of the kinematics. The separation of nuclear surfaces was verified using Cline's criterion up to 128.1° and was found to be not safe with a separation of nuclear surfaces of 4.81 fm. The first ring of the DSSSD, that corresponds to 128.1° to 119.5°, was omitted from the analysis resulting in Cline's criterion giving 4.92 fm separation between nuclear surfaces. Figure 4.24 shows the Coulomb cross section and excitation probability as a function of the recoil angles covered by the DSSSD in the laboratory frame.
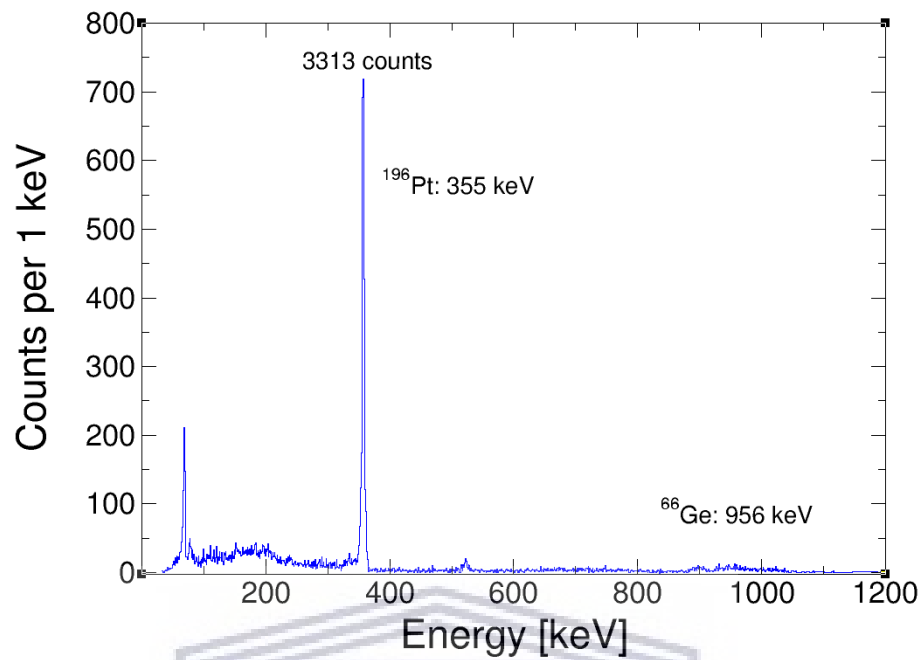
FIGURE 4.21:   Beam-gated non-Doppler-corrected spectra showing the number of counts for the 355-keV peak in ^{196}Pt.
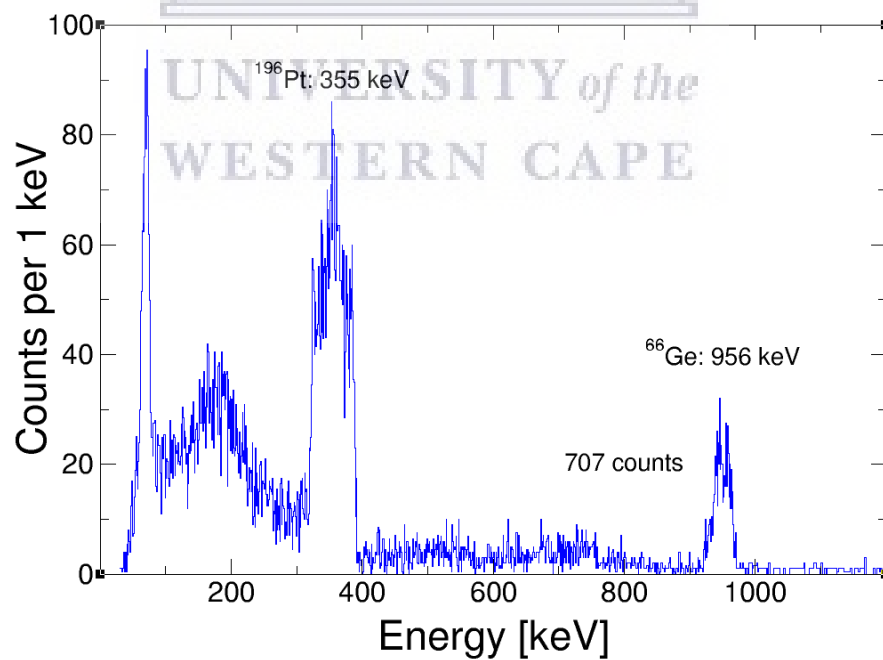
FIGURE 4.22:   Beam-gated Doppler-corrected spectra showing the counts for the 956-keV peak in ^{66}Ge.
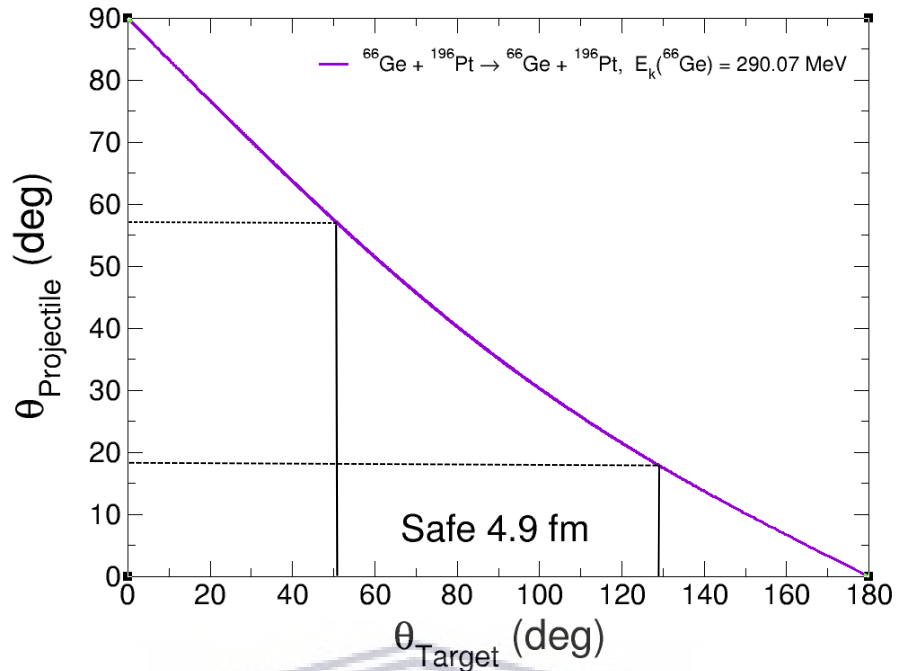
FIGURE 4.23: Kinematics plot of the scattered projectile angles as a function of the recoiling target particle angles for ^{66}Ge bombarding a ^{196}Pt target at 290.07 MeV. The kinematics curve was calculated using LISE++.

The first six rings of the DSSSD were not sensitive to $Q_S(2^+)$ in the recoil angles and were not used in the normalisation, giving a final angular range of $68.6°$ to $119.1°$. Figure 4.25 shows the target-gated non-Doppler spectra from which the yields of ^{196}Pt was determined. Figure 4.26 shows the target-gated Doppler corrected spectra from which the yields of ^{66}Ge was determined.

A total of $N_\gamma^P = 489(22)$ and $N_\gamma^T = 1656(57)$ counts for the target-gated 355- and 956.9-keV transitions were observed, yielding an intensity ratio $\frac{I_\gamma^T}{I_\gamma^P} = 1.58(5)$. The normalisation technique described in Section 4.5 was used, resulting in the Coulomb excitation diagonal band shown in Figure 4.27.

The dashed line represents the central value of the $\langle 2_1^+ ||E2||2_1^+ \rangle$ matrix element and the solid black lines represent the 1σ loci limits. The horizontal band represents the $B(E2; 2_1^+ \to 0_1^+) = 29.4(30)$ W.u. determined during this experiment. A positive $\langle 2_1^+ ||E2||2_1^+ \rangle = 0.546(60)$ eb is obtained from the intersection of the two bands, corresponding to $Q_S(2^+) = +0.41(12)$ eb. The error of $\langle 2_1^+ ||E2||2_1^+ \rangle$ is determined by the overlap region of the two bands assuming central values for the $\langle 2_1^+ ||E2||0_1^+ \rangle$, ± 0.073 eb, and the CE diagonal curve, ± 0.096 eb.
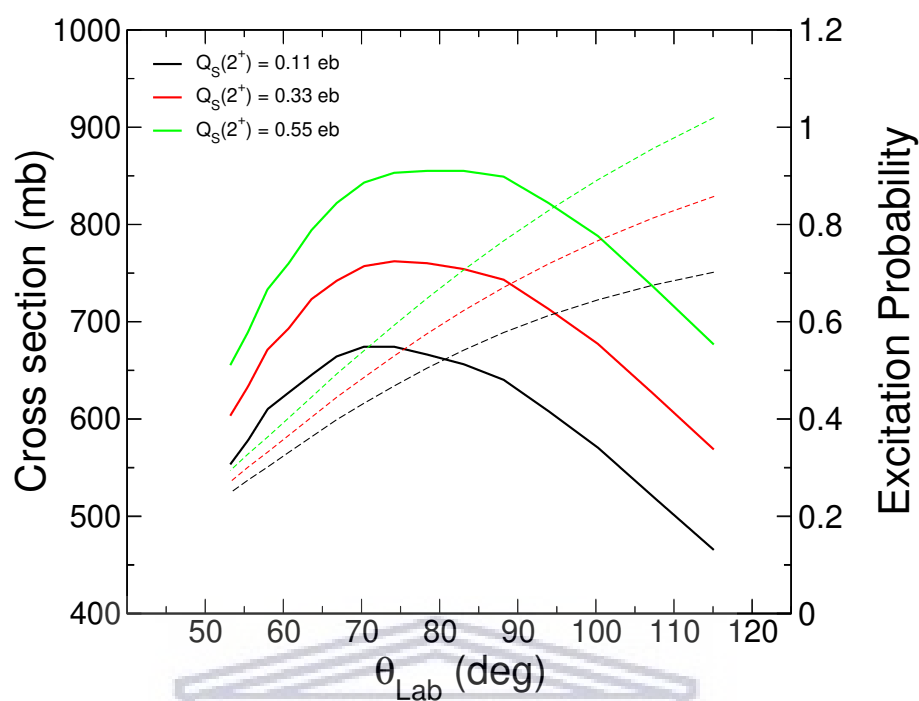
FIGURE 4.24: Coulomb cross section and excitation probability as a function of the scattering angles of the projectile corresponding to the recoil detected in the DSSSD. The cross section and excitation probability were calculated using GOSIA.
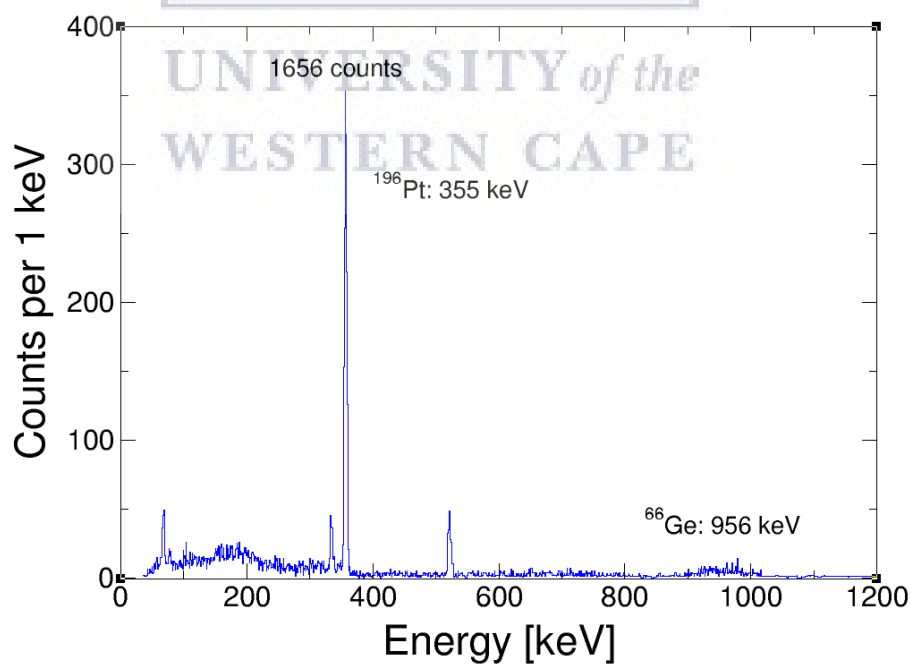
FIGURE 4.25: Target-gated non-Doppler-corrected spectra showing the number of counts for the 355-keV peak in ^{196}Pt.
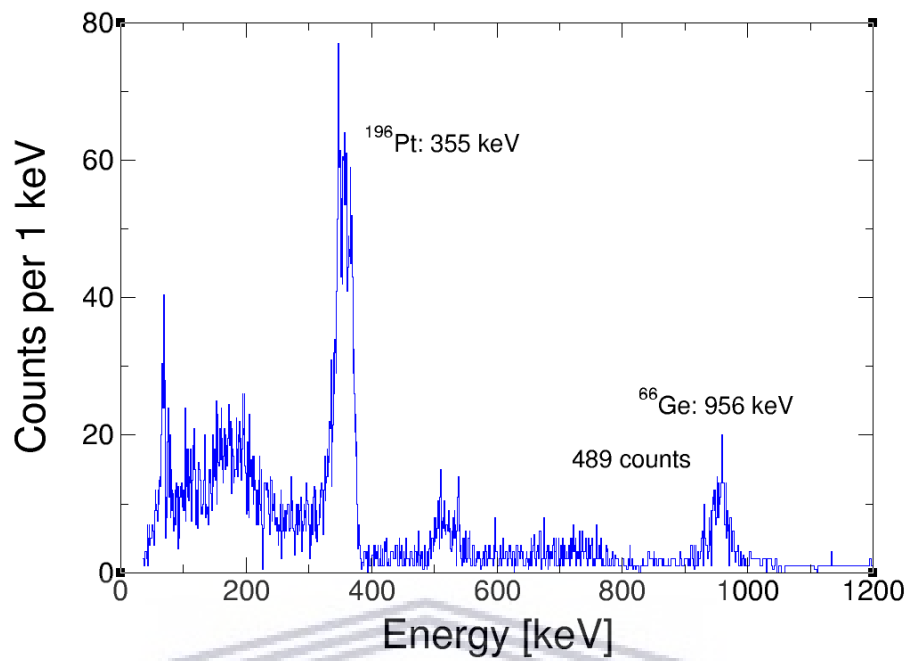
FIGURE 4.26: Target-gated Doppler-corrected spectra showing the number of counts for the 956-keV peak in ^{66}Ge.
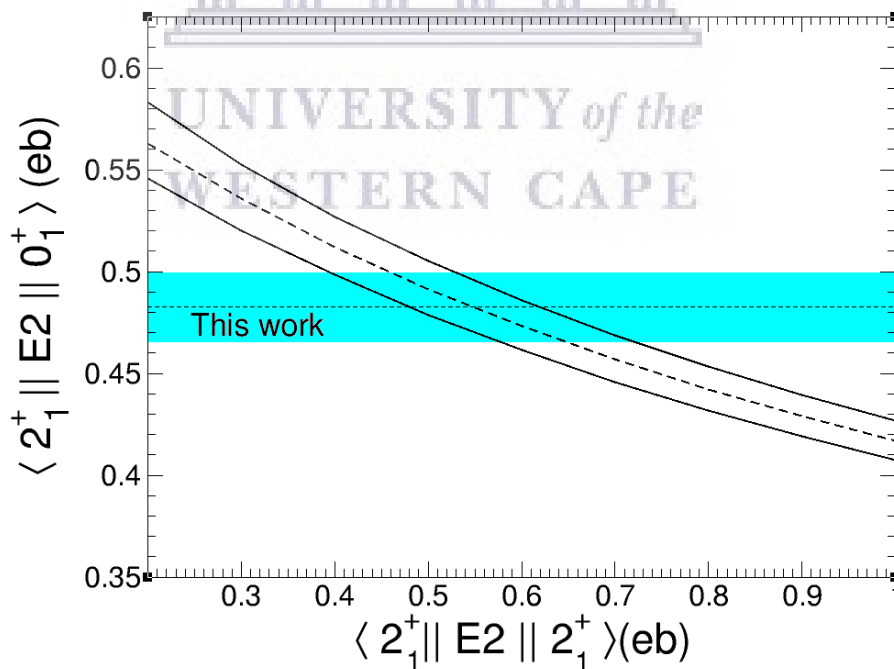
FIGURE 4.27: Variation of $\langle 2_1^+||E2||2_1^+\rangle$ as a function of $\langle 2_1^+||E2||0_1^+\rangle$ in ^{66}Ge. The solid black lines represent the loci from the upper and lower limits of the intensity ratio. The horizontal band represents the 1σ boundary for $\langle 2_1^+||E2||0_1^+\rangle = 0.483(15)$ eb.

4.5.3 χ^2 minimization using GOSIA2

The couple-channel code GOSIA2 [56] is able to extract electromagnetic matrix elements by a least-square fit to CE data. The experimental yields of the $2_1^+ \rightarrow 0_1^+$ transitions for ^{66}Ge and ^{196}Pt are used as data points. To account for the 9% of ^{70}Se present in the beam, the yields from the target were corrected for beam contaminants using the following expression [72]:

$$F = \frac{1}{1 + \sum_c \left(r_c \frac{\sigma_t(Z_c, A)}{\sigma_t(Z_X, A)} \right)},$$
<div align="right">(4.17)</div>

where $\sigma_t(Z, A)$ is the cross section of the target, excited by a beam with proton number Z and mass A. For every beam contaminant, c, with $Z = Z_c$, the ratio to the compound of interest, with $Z = Z_X$ can be expressed as $r_c = I_c/I_X$, where $I_{c,X}$ is the intensities of the respective components in the beam. Similarly, the yields from the beam needed to be corrected for impurities in the ^{196}Pt target. For this, knowledge of the isotopic impurity is required and was provided by the manufacturers of the target used in this experiment. Assuming only two components, a correction factor, F_i, can be calculated for each excited state i [73]:

$$F_i = \left(1 + \frac{1}{P} \cdot \frac{\sigma_i(Z', A')}{\sigma_i(Z, A)} \right),$$
<div align="right">(4.18)</div>

where $\sigma_i(Z, A)$ and $\sigma_i(Z', A')$ are the excitation cross sections of the state i in the projectile on the main target species and contaminant, respectively. The isotopic impurity, P, is expressed by

$$P = \frac{N_A}{N_{A'}}$$
<div align="right">(4.19)</div>

where N_A and $N_{A'}$ is the number of atoms in the main target species and contaminant, respectively. The level scheme shown in Fig 4.16 is implemented in the input file of GOSIA2. The 4_1^+ state at 2725.7 kev, which was not observed in the experiment, is a buffer state representative for all the higher excited states in ^{66}Ge. This is to ensure a proper excitation and deexcitation mechanism by avoiding unphysical population and feeding of the underlying states. Additional data points that were included in the least-square fit is the lifetime for the 2_1^+ state in ^{196}Pt and the diagonal matrix element $\langle 2_1^+||E2||2_1^+ \rangle = 0.86(10)$ eb in ^{196}Pt [67].

The $2_1^+ \rightarrow 0_1^+$ of ^{196}Pt was used for the normalization of the transition strength of ^{66}Ge relative to the target excitation of ^{196}Pt. A global minimum was obtained for all hypersurfaces and is presented within the 1σ range ($\chi^2 \leq \chi^2_{min} + 1$) in Figure 4.28.
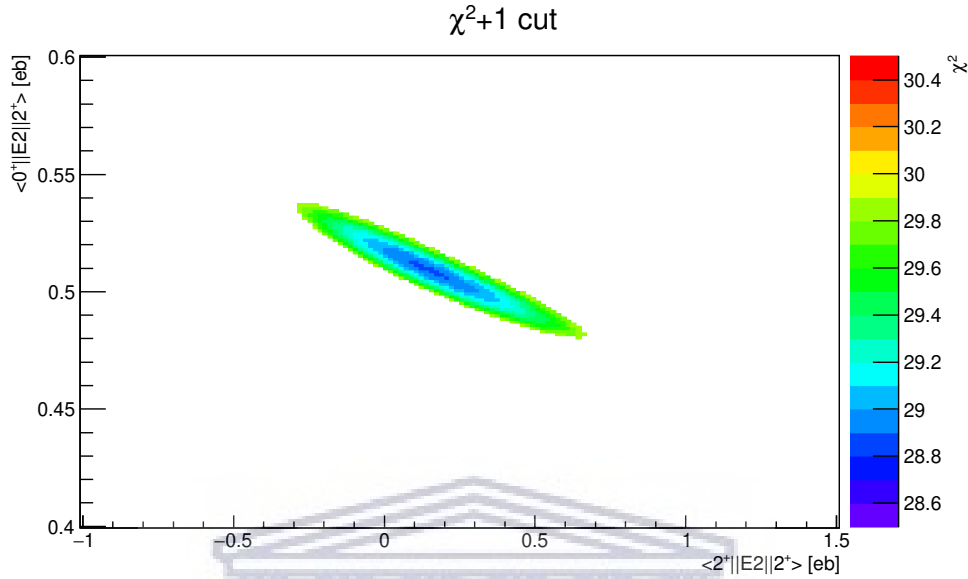
FIGURE 4.28: χ^2 values obtained within the 1σ range as a function of the $\langle 0_1^+||E2||2_1^+ \rangle$ and $\langle 2_1^+||E2||2_1^+ \rangle$ matrix elements.

The final value given by GOSIA2 is $\langle 0_1^+||E2||2_1^+ \rangle = 0.51(3)$ eb = 32.8(11) W.u.. This gives value is consistent with the value of $\langle 0_1^+||E2||2_1^+ \rangle = 0.483(15)$ eb determined in Section 4.5.1. The value of $\langle 2_1^+||E2||2_1^+ \rangle = 0.1409^{+0.528}_{-0.427}$ eb determined by GOSIA2 presents large 1σ loci limits ranging from -0.2861 eb to 0.6689 eb. This large uncertainty in the final value of $\langle 2_1^+||E2||2_1^+ \rangle$ is attributed to the low statistics obtained in the experimental yields of the 2_1^+ state of ^{66}Ge during the experiment.

Chapter 5

Discussion

It has been argued that there is a significant change in the structure of the germanium isotopes between neutron-deficient ($N < 40$) and neutron-rich ($N > 40$) nuclides. Supported by shell-model calculations [24], this has been interpreted as a shape transition from a spherical (or oblate) deformation to a prolate deformation [74]. A relatively large $B(E2; 2_1^+ \rightarrow 0_1^+)$ value of 29.4(30) W.u has been determined for ^{66}Ge in the present work, as compared with the adopted value of $B(E2; 2_1^+ \rightarrow 0_1^+) = 16.9(7)$ W.u. Figure 5.1 shows a comparison of the $B(E2; 2_1^+ \rightarrow 0_1^+)$ value calculated from this work and the accepted values given by the NNDC [50].
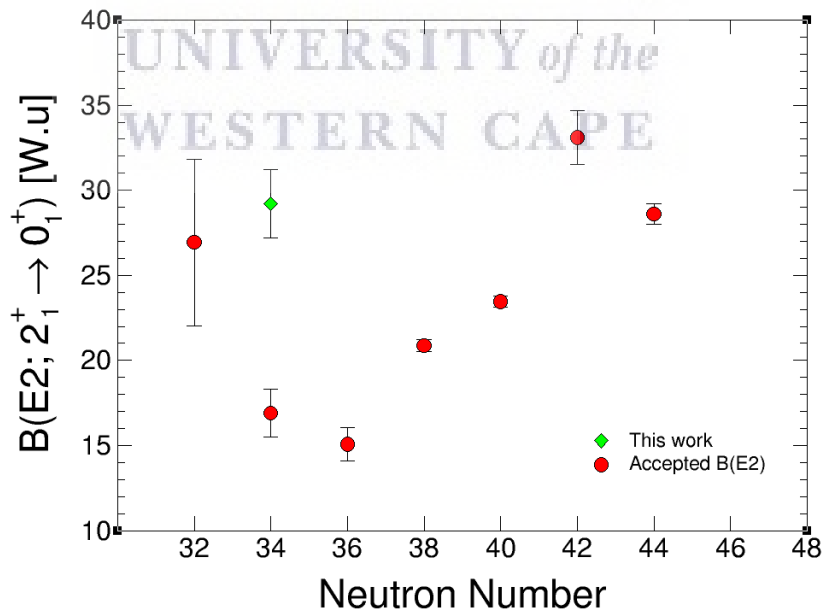
FIGURE 5.1: Adopted $B(E2; 2_1^+ \rightarrow 0_1^+)$ values for even-even germanium isotopes taken from the NNDC [2]. The $B(E2; 2_1^+ \rightarrow 0_1^+)$ for ^{64}Ge is taken from Ref. [3]. The $B(E2; 2_1^+ \rightarrow 0_1^+)$ value determined from this experiment is shown in comparison.

At first, this large $B(E2)$ value might seem strange, but our data show otherwise. The $\langle 2_1^+||E2||0_1^+\rangle$ matrix element extracted from the accepted $B(E2; 2_1^+ \to 0_1^+)$ value in ^{66}Ge has been used as the horizontal band in the normalisation method resulting in Figure 5.2. The intersection between the Coulomb-excitation curve and the horizontal band occurs at an extremely large value of $\langle 2_1^+||E2||2_1^+\rangle = 1.59$ eb. Assuming the rotor model, this gives a unphysical value of $Q_S(2_1^+) = 1.21$ eb.

Assuming again the rotor model, the value of $B(E2; 2_1^+ \to 0_1^+) = 29.4(30)$ W.u. extracted in this work yields an intrinsic quadrupole moment of $Q_0 = |1.53(8)|$ eb, which corresponds to $Q_S(2_1^+) = |0.44(2)|$ eb, in agreement with the newly-determined value of $Q_S(2^+) = +0.41(12)$ eb. It should be noted that the accepted $B(E2) = 16.9(7)$ W.u. also corresponds to a large $Q_S(2^+) = |0.33(2)|$ eb.
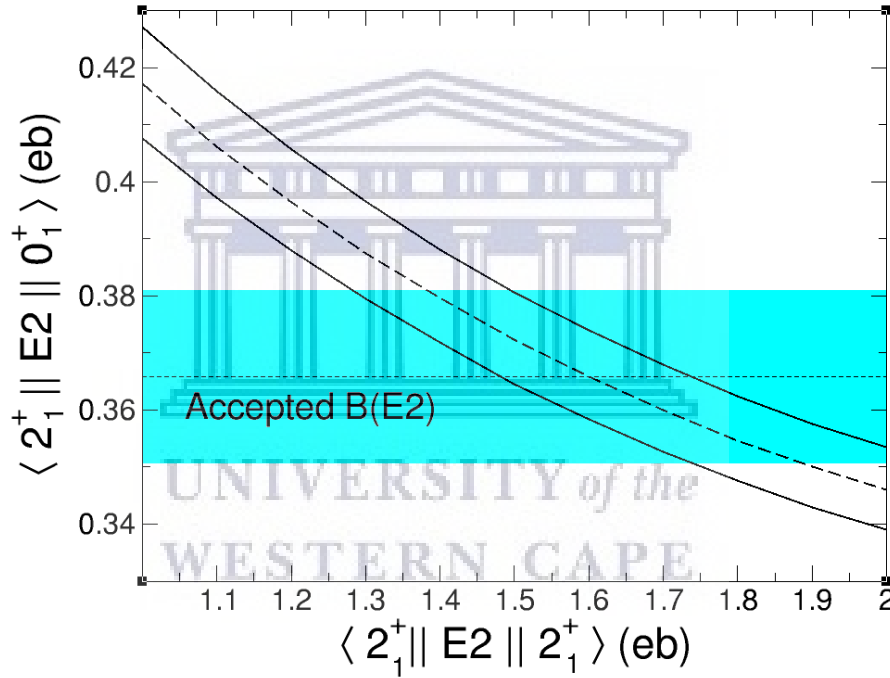
FIGURE 5.2: Variation of $\langle 2_1^+||E2||2_1^+\rangle$ as a function of $\langle 2_1^+||E2||0_1^+\rangle$ in ^{66}Ge for $\langle 2_1^+||E2||0_1^+\rangle = 0.366(15)$ eb.

For comparison, experimentally available $B(E2; 2_1^+ \to 0_1^+)$ and $Q_S(2_1^+)$ values and $E(4_1^+)/E(2_1^+)$ ratios in ^{66}Ge and other even-even nuclei in the region are listed in Table 5.1. The rotor model is assumed and neighbouring nuclei for which there is no value of $Q_S(2_1^+)$ known experimentally is inferred. It is interesting to note that these neutron-deficient nuclei in the $A \sim 60$ to 70 region present similar $E(4_1^+)/E(2_1^+)$ ratios, relatively large $B(E2)$ values and similar $Q_S(2_1^+)$ magnitudes. Moreover, Table 5.1 illustrates that the measured $B(E2)$ and $Q_S(2_1^+)$ values in the present work are comparable with those observed in neighbouring nuclei and that large $B(E2)$ values are not a rare occurrence in this region of the nuclear chart.

There is hardly any information on the sign of $Q_S(2_1^+)$ values, as these neutron-deficient nuclei are hardly accessible experimentally, and they are only known for a very few cases, such as ^{70}Se [28] (with a large uncertainty) and ^{74,76}Kr [26]. It should also be noted that this is the first time that the $Q_S(2^+)$ value in ^{66}Ge – and, for instance, in any neutron-deficient Ge isotope – has been experimentally determined.

TABLE 5.1: $B(E2; 2_1^+ \rightarrow 0_1^+)$ and $Q_S(2_1^+)$ values and $E(4_1^+)/E(2_1^+)$ ratios for even-even nuclei around ^{66}Ge. Data for ^{64}Ge are taken from Ref. [3] and the others from the NNDC adopted values [2]. Our measured values are shown in comparison. An asterisk indicates that Q_S was determined using the rotor model. Q_S for ^{64}Zn taken from Ref. [16].

Isotope	$B(E2; 2_1^+ \rightarrow 0_1^+)$ [W.u]	Q_S [eb]	$E(4_1^+)/E(2_1^+)$
^{64}Ge	27.4(43)	0.41(3)*	2.28
^{66}Ge	29.4(30)	+0.41(12)	2.27
^{68}Ge	15.07(67)	0.32(1)*	2.23
^{64}Zn	21.2(16)	−0.32(6)	2.28
^{68}Se	25.6(35)	0.42(3)*	2.27
^{70}Se	19.7(14)	0.37(1)*	2.16
^{62}Zn	16.79(81)	0.32(1)*	2.29

The $E(4_1^+)/E(2_1^+)$ values presented in TABLE 5.1 are very close to the values expected for triaxial or γ-soft nuclei according to the Wilets-Jean model [39]. In γ-soft nuclei, both prolate and oblate minima with energies very close to each other can coexist in the nuclear deformation curve as a function of quadrupole deformation. For ^{64}Ge, γ-softness has been proposed by various theoretical investigations based on collective and mean-field models [37, 75]. The authors of Ref [76] have reported that ^{68}Se exhibits similar properties to the triaxial ^{68}Ge and strong triaxiality in the ground state is predicted with a positive quadrupole moment. In TABLE 5.1, the $E(4_1^+)/E(2_1^+)$ ratio for ^{68}Ge, ^{68}Se and ^{66}Ge are very similar with comparable $B(E2; 2_1^+ \rightarrow 0_1^+)$ values, which might suggest that ^{66}Ge could exhibit similar triaxial properties as observed in ^{68}Ge and ^{68}Se. The Potential energy surface calculation for stable Zn nuclei presented in Ref [77] also suggests that ^{64}Zn is γ-soft and ^{66}Zn is triaxial.

Furthermore, the measured $B(E2)$ and $Q_S(2^+)$ values are compared to large-scale shell-model and beyond mean-field calculations presented in this work to investigate if the magnitude of the transition strength and deformation are predicted. Section 5.1 compares the measured $B(E2)$ value to previous shell-model calculations using various effective interactions. Section 5.2 compares the measured $B(E2)$ and $Q_S(2^+)$ values to beyond mean-field calculations presented in this work.

5.1 Comparison to Shell-model Calculations

Shell-model calculations using various effective interactions were compared with the measured $B(E2)$ value. Figure 5.3 shows our result compared to shell-model calculations and the adopted values of $B(E2; 2_1^+ \rightarrow 0_1^+)$ for the even-even germanium isotopes. The GXP1F interaction [14] performs shell-model calculations in the pf valence space, which includes the $f_{7/2}$, $p_{3/2}$, $f_{5/2}$ and $p_{1/2}$ orbitals. This calculation was performed with effective charges $e_\pi = 1.5$ for protons and $e_v = 0.5$ for neutrons. The GXP1F prediction for the $B(E2)$ value is in good agreement with the adopted values for $^{64-48}$Ge, but under-predicts our measured value. The $B(E2)$ of ^{70}Ge is significantly under-predicted by this interaction. This discrepancy is attributed to the $g_{9/2}$ orbital not being included in the valence space [14]. It should be noted from Ref. [14] that, in the pf-shell calculations, the ^{56}Ni core is most significantly broken at $N = 32 \sim 34$. The role of the $g_{9/2}$ orbital in the f_5pg_9-shell may explain the significant drop in collectivity for $^{66-68}$Ge.
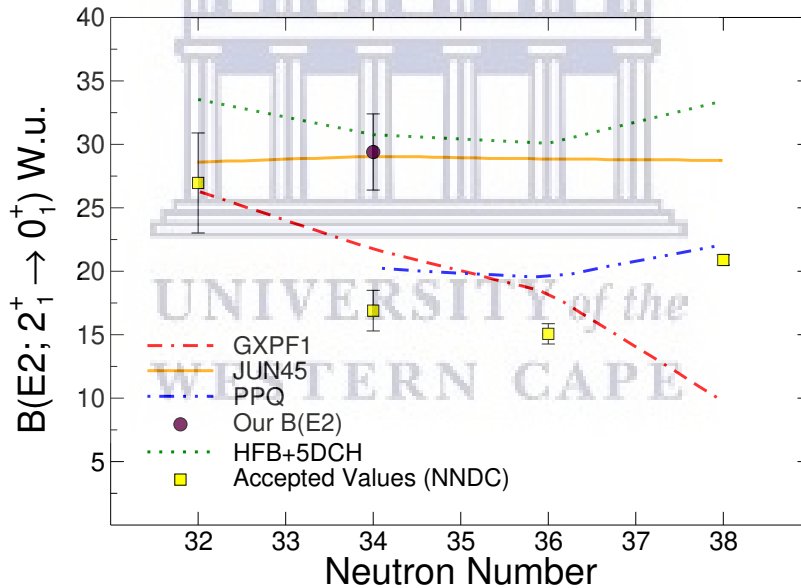
FIGURE 5.3: Shell-model calculations using various interactions are compared to the experimentally determined $B(E2)$ value for ^{66}Ge. The interactions used were JUN45 [12], PPQ [13], GXPF1 [14], and HFB+5DCH [15]. The adopted $B(E2)$ value of even-even germanium isotopes are shown in comparison with the shell-model calculations.

The extended pairing plus quadrupole (PPQ) Hamiltonian [13] was employed in the model space including the $p_{3/2}$, $f_{5/2}$, $p_{1/2}$, and $g_{9/2}$ orbitals [78]. PP+Q predicts $B(E2)$ values for $^{66-70}$Ge comparable to the accepted values when using the effective charges $e_\pi = 1.5$ and $e_v = 0.5$. The missing $f_{7/2}$ orbital has been attributed as the reason why the pf-shell calculations resulted in less collectivity being determined for $^{66-68}$Ge. The

PPQ calculation investigated the influence of the neutron effective charge and found that increasing it to $e_v = 0.97$ significantly increased the $B(E2)$ strengths of $^{66-68}$Ge. The JUN45 interaction was used to perform shell-model calculations in the $f_{5/2}pg_{9/2}$ model space [12]. The model space included the $p_{3/2}$, $p_{1/2}$, $f_{5/2}$, and $g_{9/2}$ orbitals. JUN45's prediction for the $B(E2)$ value of ^{66}Ge is in agreement with what we measured. Effective charges $e_\pi = 1.5$ and $e_v = 1.1$ were used in the calculation. The authors of Ref. [15] performed shell-model calculations for neutron-deficient germanium isotopes using the Hartree-Fock-Bogoluibov (HFB) interaction with configuration mixing performed via the generator coordinate method (GCM), treated in the Gaussian overlap approximation (GOA). The technique of five-dimensional collective Hamiltonian (5DCH) was used in the implementation of GCM. The effective interaction used in the calculations is Gogny D1S [79]. This calculation makes use of no effective charges and instead finds solutions to the constrained HFB while exploring all quadrupole degrees of freedom. Mass renormalisation [80], a technique for restoring minor symmetries specific to the 5DCH, was used, resulting in the green curve in Figure 5.3. The calculated $B(E2)$ value for ^{66}Ge is well in agreement with the value we measured.

5.2 Comparison to Beyond Mean-field Calculations

The measured nuclear deformation was compared with Particle Number Variation After Projection (PN-VAP) beyond mean-field calculations. The symmetry-conserving configuration mixing (SCCM) method was used, which is based on the GCM and includes particle number and angular momentum restoration, as well as shape mixing of axial and triaxial intrinsic states [81]. The underlying interaction used is the Gogny D1S. Calculations with 5DCH, in which quantum number restoration is not taken into account, could result in fictitious mixing of solutions with different particle numbers [81]. PN-VAP varies the shape and minimises the energy to predict the collective behaviour of a nucleus. The energy and collective wavefunctions for different states are obtained by solving the Schrödinger equation after projection onto angular momentum and configuration mixing. This method was applied to ^{66}Ge by Tomás Rodríguez via private communication [82], for which results of the potential energy surface are shown in Figure 5.4.

After projection onto angular momentum and configuration mixing, the shape for each state in ^{66}Ge is determined. Table 5.2 shows the $B(E2)$ value for the $0_1^+ \rightarrow 2_1^+$ and $2_1^+ \rightarrow 4_1^+$ transitions, along with the Q_S value predicted for these transitions. Figure 5.5 shows the results after projection for the first 0^+, 2^+ and 4^+ states.
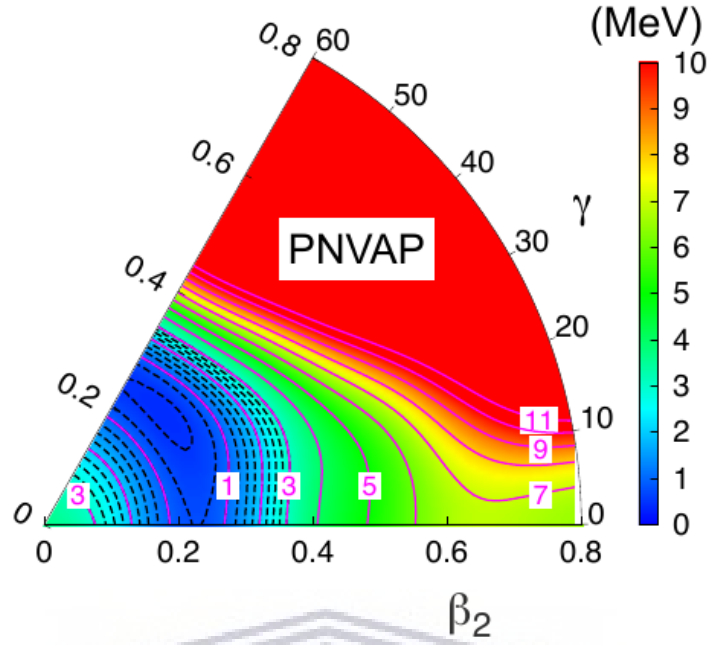
FIGURE 5.4: Potential energy surface for ^{66}Ge before angular momentum projection using the PN-VAP method.

TABLE 5.2: $B(E2)$ values from PN-VAP calculations for ^{66}Ge and Q_S.

J^π	Transition	$B(E2)\uparrow$ [e^{2}fm^4]	$B(E2)$ [W.u.]	Q_S [eb]
2^+	$0_1^+ \to 2_1^+$	3164.3	39.9	0.21
4^+	$2_1^+ \to 4_1^+$	1690.4	21.3	0.21
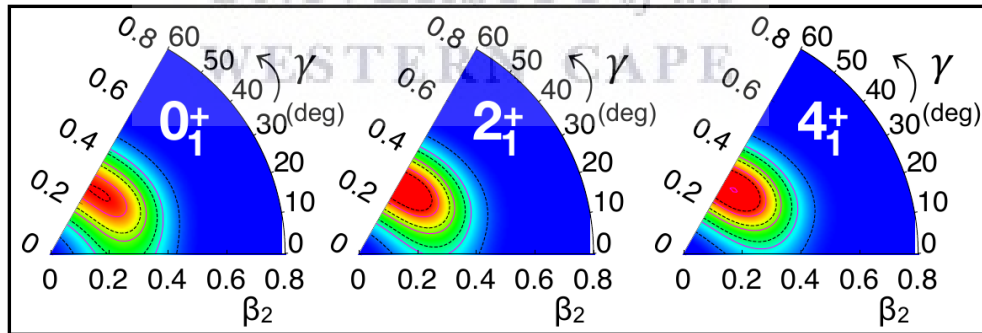
FIGURE 5.5: Wavefunction probability map for the first 0^+, 2^+ and 4^+ states in ^{66}Ge after angular momentum projection and configuration mixing.

Beyond mean-field calculations predict $Q_S(2_1^+) = +0.21$ eb with a deformation parameter $\beta_2 = -0.25 \sim -0.30$. The $Q_S(2^+) = +0.41(12)$ eb determined in the present work is a bit larger than the theoretical value, but yields a similar quadrupole deformation of $\beta_2 = -0.25$. The PN-VAP calculation determines $B(E2; 0_1^+ \to 2_1^+) = 3164.3$ e^{2}fm^4 = 39.9 W.u., which supports the fact that ^{66}Ge may be more collective than previous

experimental work anticipated. Figure 5.4 also supports the view that ^{66}Ge is a γ-soft nucleus as previously suggest by Nomura *et al.* [76].

Finally, although there is a large discrepancy with previous lifetime measurements, a longer lifetime measurement for the 2_1^+ state in ^{66}Ge could result from the contamination of a similar 953.8-keV transition depopulating the 2_1^+ state in ^{62}Zn – which is also populated in the fusion-evaporation reaction used to produce ^{66}Ge – with a relatively longer lifetime of $\tau(2_1^+) = 4.2(2)$ ps (a lifetime of $\tau(2_1^+) = 3.8(5)$ ps was measured by Lüttke and collaborators). Although for this to happen, the $\gamma - \gamma$ coincidence gate on the $4_1^+ \rightarrow 2_1^+$ transition in ^{66}Ge (1217 keV) should allow part of the $4_1^+ \rightarrow 2_1^+$ transition in ^{62}Zn (1232 keV).

Chapter 6

Conclusions

A successful CE experiment has been carried out at the HIE-ISOLDE facility at CERN. Beams of ^{66}Ge were accelerated for the first time at "safe" energies of 290.07 MeV and bombarded a 4-mg/cm^2 thick ^{196}Pt target. The de-excited γ rays were detected using eight cluster HPGe detectors and scattered particles were detected with DSSSD detectors placed 27.34 mm downstream from the target. A particle-γ coincidence condition was applied, and the $B(E2)$ and Q_S values for the first 2^+ state have been extracted from the beam-gated and target-gated data, respectively. The measured $B(E2; 2_1^+ \rightarrow 0_1^+) = 29.4(30)$ W.u. and $Q_S = +0.41(13)$ eb suggest that ^{66}Ge is more collective than previously determined. It should be noted this is the first time that the quadrupole deformation of ^{66}Ge has been experimentally determined. A χ^2 surface scan was also performed to determine the $B(E2)$ and Q_S values for the first 2^+ using GOSIA2. The determined $B(E2; 2_1^+ \rightarrow 0_1^+) = 31.18(9)$ W.u. is in good agreement with the measured $B(E2; 2_1^+ \rightarrow 0_1^+) = 29.4(30)$ W.u. An accurate value for the $\langle 2_1^+ ||E2|| 2_1^+ \rangle$ matrix element could not be determined with the χ^2 fit, as the uncertainty in the value ranged from -0.3055 eb to 0.6035 eb. This large uncertainty is attributed to the low statistics of the 2_1^+ state obtained during the experiment. In addition, various large-scale shell-model and beyond mean-field calculations were compared with the experimentally determined results. The experimentally determined $B(E2)$ is reproduced with the JUN45 interaction and using a 5DCH approach. The beyond mean-field calculations predict a nuclear deformation for ^{66}Ge, which is in agreement with the experimentally determined spectroscopic quadrupole moment.

6.1 Future Work

The experiment at CERN (IS569) was approved to study ^{70}Se bombarding onto a ^{208}Pt target; however, due to the primary target containing an excess amount of sulphur, ^{66}Ge was produced instead. The experimental setup was initially set up and optimised to run ^{70}Se. For example, the DSSSD was situated at a fixed distance away from the target which may have resulted in fewer yields in the outer rings. A future experiment could be proposed to study ^{66}Ge and optimising the experimental setup for the kinematics of the reaction in question. Large-scale shell model and beyond mean-field calculations predicts the existence of a 0_2^+ state that has never been observed before. The information gained by knockout reactions, CE and beta decay experiments, in conjunction with advancements to radioactive beam facilities such as HIE-ISOLDE, could shed light on the existence of the 0_2^+ state in ^{66}Ge.

The quadrupole sum rules method can also provide information regarding the charge distribution of ^{66}Ge in its specific states. It is based on the fact that the electrical quadrupole operator, E2, is a spherical tensor and thus its zero-coupled products are rotationally invariant. Such invariants can be linked to deformation parameters in the intrinsic frame of the nucleus, namely Q_0, the overall quadrupole deformation parameter (equivalent to the elongation parameter β in the Bohr model) and δ, which is related to the trixiality parameter γ.

Appendix A

GOSIA Files

The GOSIA2 input files for ^{66}Ge and ^{196}Pt is presented in this appendix. The purpose of this appendix is to provide the GOSIA file structure for the various operations performed during the analysis process of ^{66}Ge. The files are structured for a ^{66}Ge beam bombarding on a ^{196}Pt target at a beam energy of 290.07 MeV. Comments in the input file are preceded by an exclamation mark. For a detailed description of the operations used, the reader is referred to the GOSIA manual [56].

```
66Ge_on_196Pt_290.07MeV.inp
```

```
1
OP,FILE
22,3,1
66Ge_on_196Pt.out
25,3,1
66Ge_on_196Pt.inp
26,3,1
66Ge_on_196Pt_target.inp
9,3,1
miniball.f9
8,3,1
miniball.f8
3,3,1
66Ge.yie
4,3,1
66Ge.cor
7,3,1
66Ge.map
27,3,1
196Pt.map
12,3,1
66Ge.bst
32,3,1
196Pt.bst
28,3,1
66Ge.bricc
0,0,0
OP,TITL
 Beam Excitation of 66Ge on 196Pt @ 4.395 MeV/u
OP,GOSI      ! This operation is used to define the nucleus to be studied
LEVE         ! The level scheme used for the calculation is defined in this section
1,1,0,0.0
2,1,2,0.9569
3,1,4,2.1733
4,1,2,1.6932
```

```
5,1,3,2.4952
6,1,4,2.7257
0,0,0,0
ME            ! Construct the matrix elements between the levels defined in LEVE
2 0 0 0 0    ! E2 matrix elements
1 2 0.3096386425 -2 2
1 4 0.0323607234  2 2
2 2 -0.164706308 -2 2
2 3 0.2220533271  2 2
2 4 0.3567540469  2 2
2 5 -0.0077315189 2 2
2 6 0.0615164486  2 2
3 3 -0.1578064053 2 2
3 4 0.0028829197  1 1
3 5 -0.010786897  1 1
3 6 0.1824658127  1 1
4 4 0.3466872936  1 1
4 5 0.2231401085  2 2
4 6 0.3215931039  2 2
5 5 0.000001 2 2
5 6 0.3797772177  1 1
6 6 -0.1322215456 1 1
7 0 0 0 0
2 4 -0.1901859192 2 2
2 5 0.0041955488 2 2
3 5 0.00572 2 2
3 6 0.0998572105 2 2
4 5 -0.0512012986 2 2
5 6 -0.0493 2 2
0 0 0 0 0
EXPT      ! Experimental conditions of the experiments to be run
7,32,66
-78,196,290.07,24.93,5,1,0,0,360,1,1 !1
-78,196,290.07,37.05,5,1,0,0,360,1,1 !2
-78,196,290.07,46.30,5,1,0,0,360,1,1 !3
-78,196,290.07,53.24,5,1,0,0,360,1,1 !4
-78,196,290.07,-26.775,5,1,0,0,360,1,1 !5
-78,196,290.07,-35.855,5,1,0,0,360,1,1 !6
-78,196,290.07,-43.275,5,1,0,0,360,1,1 !7
CONT
SPL,1.    ! Cubic spline interpolation used instead of Lagrange
EFF,7.    ! Defines the efficiency curve from RADWARE parameters
1,4
2,4
3,4
4,4
5,4
6,4
7,4
INT,7.
1,1000
2,1000
3,1000
4,1000
5,1000
6,1000
7,1000
PRT,
1,-1
2,0
4,0
5,1
11,0
12,0
14,0
16,0
18,1
0,0
END,
              ! KEEP THIS LINE EMPTY
OP,BRIC        ! Get the internal conversion coefficients from BRICC database
/home/kenzo/Gosia/66Ge_Gosia2/frontback66Ge/BrIccFOV22.idx
/home/kenzo/Gosia/66Ge_Gosia2/frontback66Ge/BrIccFOV22.icc
OP,YIEL        ! Calculates the yields of de-exciting gamma rays after Coulomb Excitation
0
```

```
-1,0
0.010
24,24,24,24,24,24,24                    ! 7 experiments with 24 detectors for each
1,1,1,1,1,1,1,1,1,1,1,1,1,1,1,1,1,1,1,1,1,1,1,1
142.9,109.6,118.6,46.8,47.6,74.5,67.9,39.1,69.7,146.7,113.4,117,111.4,143.5,115.8,44.9,42.9,70.2,131.6,132.4,107.7,63.5,38.8,69.1        ! Theta angle
131.5,127.4,162.8,22.4,69.1,45.1,126.4,146.5,161.6,38,24.7,62.9,243.7,232.2,207.6,196.9,245.1,222.5,342.7,302.1,321.8,316.2,341.1,349.7 ! Phi angle
1,1,1,1,1,1,1,1,1,1,1,1,1,1,1,1,1,1,1,1,1,1,1,1
142.9,109.6,118.6,46.8,47.6,74.5,67.9,39.1,69.7,146.7,113.4,117,111.4,143.5,115.8,44.9,42.9,70.2,131.6,132.4,107.7,63.5,38.8,69.1
131.5,127.4,162.8,22.4,69.1,45.1,126.4,146.5,161.6,38,24.7,62.9,243.7,232.2,207.6,196.9,245.1,222.5,342.7,302.1,321.8,316.2,341.1,349.7
1,1,1,1,1,1,1,1,1,1,1,1,1,1,1,1,1,1,1,1,1,1,1,1
142.9,109.6,118.6,46.8,47.6,74.5,67.9,39.1,69.7,146.7,113.4,117,111.4,143.5,115.8,44.9,42.9,70.2,131.6,132.4,107.7,63.5,38.8,69.1
131.5,127.4,162.8,22.4,69.1,45.1,126.4,146.5,161.6,38,24.7,62.9,243.7,232.2,207.6,196.9,245.1,222.5,342.7,302.1,321.8,316.2,341.1,349.7
1,1,1,1,1,1,1,1,1,1,1,1,1,1,1,1,1,1,1,1,1,1,1,1
142.9,109.6,118.6,46.8,47.6,74.5,67.9,39.1,69.7,146.7,113.4,117,111.4,143.5,115.8,44.9,42.9,70.2,131.6,132.4,107.7,63.5,38.8,69.1
131.5,127.4,162.8,22.4,69.1,45.1,126.4,146.5,161.6,38,24.7,62.9,243.7,232.2,207.6,196.9,245.1,222.5,342.7,302.1,321.8,316.2,341.1,349.7
1,1,1,1,1,1,1,1,1,1,1,1,1,1,1,1,1,1,1,1,1,1,1,1
142.9,109.6,118.6,46.8,47.6,74.5,67.9,39.1,69.7,146.7,113.4,117,111.4,143.5,115.8,44.9,42.9,70.2,131.6,132.4,107.7,63.5,38.8,69.1
131.5,127.4,162.8,22.4,69.1,45.1,126.4,146.5,161.6,38,24.7,62.9,243.7,232.2,207.6,196.9,245.1,222.5,342.7,302.1,321.8,316.2,341.1,349.7
1,1,1,1,1,1,1,1,1,1,1,1,1,1,1,1,1,1,1,1,1,1,1,1
142.9,109.6,118.6,46.8,47.6,74.5,67.9,39.1,69.7,146.7,113.4,117,111.4,143.5,115.8,44.9,42.9,70.2,131.6,132.4,107.7,63.5,38.8,69.1
131.5,127.4,162.8,22.4,69.1,45.1,126.4,146.5,161.6,38,24.7,62.9,243.7,232.2,207.6,196.9,245.1,222.5,342.7,302.1,321.8,316.2,341.1,349.7
1,1,1,1,1,1,1,1,1,1,1,1,1,1,1,1,1,1,1,1,1,1,1,1
142.9,109.6,118.6,46.8,47.6,74.5,67.9,39.1,69.7,146.7,113.4,117,111.4,143.5,115.8,44.9,42.9,70.2,131.6,132.4,107.7,63.5,38.8,69.1
131.5,127.4,162.8,22.4,69.1,45.1,126.4,146.5,161.6,38,24.7,62.9,243.7,232.2,207.6,196.9,245.1,222.5,342.7,302.1,321.8,316.2,341.1,349.7
2,1   ! Transition for normalization of the gamma yields
1     ! 1
1000
1
1     !2
1000
1
1     !3
1000
1
1     !4
1000
1
1     !5
1000
1
1     !6
1000
1
1     !7
1000
1
4     ! This variable determines which file contains the gamma ray yields. 0 means no file is needed.
0,0
0,0
0,0
0,0
OP,RAW               ! Defines the efficiency curve for the gamma ray yields
1                                          !Experiment 1
1.0 7.895 -0.475 0.0 6.99 -0.76 1.1 15.0
1.0 7.895 -0.475 0.0 6.99 -0.76 1.1 15.0
1.0 7.895 -0.475 0.0 6.99 -0.76 1.1 15.0
1.0 7.895 -0.475 0.0 6.99 -0.76 1.1 15.0
1.0 7.895 -0.475 0.0 6.99 -0.76 1.1 15.0
1.0 7.895 -0.475 0.0 6.99 -0.76 1.1 15.0
1.0 7.895 -0.475 0.0 6.99 -0.76 1.1 15.0
1.0 7.895 -0.475 0.0 6.99 -0.76 1.1 15.0
1.0 7.895 -0.475 0.0 6.99 -0.76 1.1 15.0
1.0 7.895 -0.475 0.0 6.99 -0.76 1.1 15.0
1.0 7.895 -0.475 0.0 6.99 -0.76 1.1 15.0
1.0 7.895 -0.475 0.0 6.99 -0.76 1.1 15.0
1.0 7.895 -0.475 0.0 6.99 -0.76 1.1 15.0
1.0 7.895 -0.475 0.0 6.99 -0.76 1.1 15.0
1.0 7.895 -0.475 0.0 6.99 -0.76 1.1 15.0
1.0 7.895 -0.475 0.0 6.99 -0.76 1.1 15.0
1.0 7.895 -0.475 0.0 6.99 -0.76 1.1 15.0
1.0 7.895 -0.475 0.0 6.99 -0.76 1.1 15.0
1.0 7.895 -0.475 0.0 6.99 -0.76 1.1 15.0
1.0 7.895 -0.475 0.0 6.99 -0.76 1.1 15.0
1.0 7.895 -0.475 0.0 6.99 -0.76 1.1 15.0
1.0 7.895 -0.475 0.0 6.99 -0.76 1.1 15.0
```

```
1.0 7.895 -0.475 0.0 6.99 -0.76 1.1 15.0
1.0 7.895 -0.475 0.0 6.99 -0.76 1.1 15.0
1
24
1,2,3,4,5,6,7,8,9,10,11,12,13,14,15,16,17,18,19,20,21,22,23,24
2                                    !Experiment 2
1.0 7.895 -0.475 0.0 6.99 -0.76 1.1 15.0
1.0 7.895 -0.475 0.0 6.99 -0.76 1.1 15.0
1.0 7.895 -0.475 0.0 6.99 -0.76 1.1 15.0
1.0 7.895 -0.475 0.0 6.99 -0.76 1.1 15.0
1.0 7.895 -0.475 0.0 6.99 -0.76 1.1 15.0
1.0 7.895 -0.475 0.0 6.99 -0.76 1.1 15.0
1.0 7.895 -0.475 0.0 6.99 -0.76 1.1 15.0
1.0 7.895 -0.475 0.0 6.99 -0.76 1.1 15.0
1.0 7.895 -0.475 0.0 6.99 -0.76 1.1 15.0
1.0 7.895 -0.475 0.0 6.99 -0.76 1.1 15.0
1.0 7.895 -0.475 0.0 6.99 -0.76 1.1 15.0
1.0 7.895 -0.475 0.0 6.99 -0.76 1.1 15.0
1.0 7.895 -0.475 0.0 6.99 -0.76 1.1 15.0
1.0 7.895 -0.475 0.0 6.99 -0.76 1.1 15.0
1.0 7.895 -0.475 0.0 6.99 -0.76 1.1 15.0
1.0 7.895 -0.475 0.0 6.99 -0.76 1.1 15.0
1.0 7.895 -0.475 0.0 6.99 -0.76 1.1 15.0
1.0 7.895 -0.475 0.0 6.99 -0.76 1.1 15.0
1.0 7.895 -0.475 0.0 6.99 -0.76 1.1 15.0
1.0 7.895 -0.475 0.0 6.99 -0.76 1.1 15.0
1.0 7.895 -0.475 0.0 6.99 -0.76 1.1 15.0
1.0 7.895 -0.475 0.0 6.99 -0.76 1.1 15.0
1.0 7.895 -0.475 0.0 6.99 -0.76 1.1 15.0
1
24
1,2,3,4,5,6,7,8,9,10,11,12,13,14,15,16,17,18,19,20,21,22,23,24
3                                    !Experiment 3
1.0 7.895 -0.475 0.0 6.99 -0.76 1.1 15.0
1.0 7.895 -0.475 0.0 6.99 -0.76 1.1 15.0
1.0 7.895 -0.475 0.0 6.99 -0.76 1.1 15.0
1.0 7.895 -0.475 0.0 6.99 -0.76 1.1 15.0
1.0 7.895 -0.475 0.0 6.99 -0.76 1.1 15.0
1.0 7.895 -0.475 0.0 6.99 -0.76 1.1 15.0
1.0 7.895 -0.475 0.0 6.99 -0.76 1.1 15.0
1.0 7.895 -0.475 0.0 6.99 -0.76 1.1 15.0
1.0 7.895 -0.475 0.0 6.99 -0.76 1.1 15.0
1.0 7.895 -0.475 0.0 6.99 -0.76 1.1 15.0
1.0 7.895 -0.475 0.0 6.99 -0.76 1.1 15.0
1.0 7.895 -0.475 0.0 6.99 -0.76 1.1 15.0
1.0 7.895 -0.475 0.0 6.99 -0.76 1.1 15.0
1.0 7.895 -0.475 0.0 6.99 -0.76 1.1 15.0
1.0 7.895 -0.475 0.0 6.99 -0.76 1.1 15.0
1.0 7.895 -0.475 0.0 6.99 -0.76 1.1 15.0
1.0 7.895 -0.475 0.0 6.99 -0.76 1.1 15.0
1.0 7.895 -0.475 0.0 6.99 -0.76 1.1 15.0
1.0 7.895 -0.475 0.0 6.99 -0.76 1.1 15.0
1.0 7.895 -0.475 0.0 6.99 -0.76 1.1 15.0
1.0 7.895 -0.475 0.0 6.99 -0.76 1.1 15.0
1.0 7.895 -0.475 0.0 6.99 -0.76 1.1 15.0
1.0 7.895 -0.475 0.0 6.99 -0.76 1.1 15.0
1.0 7.895 -0.475 0.0 6.99 -0.76 1.1 15.0
1
24
1,2,3,4,5,6,7,8,9,10,11,12,13,14,15,16,17,18,19,20,21,22,23,24
4                                    !Experiment 4
1.0 7.895 -0.475 0.0 6.99 -0.76 1.1 15.0
1.0 7.895 -0.475 0.0 6.99 -0.76 1.1 15.0
1.0 7.895 -0.475 0.0 6.99 -0.76 1.1 15.0
1.0 7.895 -0.475 0.0 6.99 -0.76 1.1 15.0
1.0 7.895 -0.475 0.0 6.99 -0.76 1.1 15.0
1.0 7.895 -0.475 0.0 6.99 -0.76 1.1 15.0
1.0 7.895 -0.475 0.0 6.99 -0.76 1.1 15.0
1.0 7.895 -0.475 0.0 6.99 -0.76 1.1 15.0
1.0 7.895 -0.475 0.0 6.99 -0.76 1.1 15.0
1.0 7.895 -0.475 0.0 6.99 -0.76 1.1 15.0
1.0 7.895 -0.475 0.0 6.99 -0.76 1.1 15.0
1.0 7.895 -0.475 0.0 6.99 -0.76 1.1 15.0
1.0 7.895 -0.475 0.0 6.99 -0.76 1.1 15.0
```

```
1.0 7.895 -0.475 0.0 6.99 -0.76 1.1 15.0
1.0 7.895 -0.475 0.0 6.99 -0.76 1.1 15.0
1.0 7.895 -0.475 0.0 6.99 -0.76 1.1 15.0
1.0 7.895 -0.475 0.0 6.99 -0.76 1.1 15.0
1.0 7.895 -0.475 0.0 6.99 -0.76 1.1 15.0
1.0 7.895 -0.475 0.0 6.99 -0.76 1.1 15.0
1.0 7.895 -0.475 0.0 6.99 -0.76 1.1 15.0
1.0 7.895 -0.475 0.0 6.99 -0.76 1.1 15.0
1.0 7.895 -0.475 0.0 6.99 -0.76 1.1 15.0
1.0 7.895 -0.475 0.0 6.99 -0.76 1.1 15.0
1.0 7.895 -0.475 0.0 6.99 -0.76 1.1 15.0
1
24
1,2,3,4,5,6,7,8,9,10,11,12,13,14,15,16,17,18,19,20,21,22,23,24
5                                    !Experiment 5
1.0 7.895 -0.475 0.0 6.99 -0.76 1.1 15.0
1.0 7.895 -0.475 0.0 6.99 -0.76 1.1 15.0
1.0 7.895 -0.475 0.0 6.99 -0.76 1.1 15.0
1.0 7.895 -0.475 0.0 6.99 -0.76 1.1 15.0
1.0 7.895 -0.475 0.0 6.99 -0.76 1.1 15.0
1.0 7.895 -0.475 0.0 6.99 -0.76 1.1 15.0
1.0 7.895 -0.475 0.0 6.99 -0.76 1.1 15.0
1.0 7.895 -0.475 0.0 6.99 -0.76 1.1 15.0
1.0 7.895 -0.475 0.0 6.99 -0.76 1.1 15.0
1.0 7.895 -0.475 0.0 6.99 -0.76 1.1 15.0
1.0 7.895 -0.475 0.0 6.99 -0.76 1.1 15.0
1.0 7.895 -0.475 0.0 6.99 -0.76 1.1 15.0
1.0 7.895 -0.475 0.0 6.99 -0.76 1.1 15.0
1.0 7.895 -0.475 0.0 6.99 -0.76 1.1 15.0
1.0 7.895 -0.475 0.0 6.99 -0.76 1.1 15.0
1.0 7.895 -0.475 0.0 6.99 -0.76 1.1 15.0
1.0 7.895 -0.475 0.0 6.99 -0.76 1.1 15.0
1.0 7.895 -0.475 0.0 6.99 -0.76 1.1 15.0
1.0 7.895 -0.475 0.0 6.99 -0.76 1.1 15.0
1.0 7.895 -0.475 0.0 6.99 -0.76 1.1 15.0
1.0 7.895 -0.475 0.0 6.99 -0.76 1.1 15.0
1.0 7.895 -0.475 0.0 6.99 -0.76 1.1 15.0
1.0 7.895 -0.475 0.0 6.99 -0.76 1.1 15.0
1
24
1,2,3,4,5,6,7,8,9,10,11,12,13,14,15,16,17,18,19,20,21,22,23,24
6                                    !Experiment 6
1.0 7.895 -0.475 0.0 6.99 -0.76 1.1 15.0
1.0 7.895 -0.475 0.0 6.99 -0.76 1.1 15.0
1.0 7.895 -0.475 0.0 6.99 -0.76 1.1 15.0
1.0 7.895 -0.475 0.0 6.99 -0.76 1.1 15.0
1.0 7.895 -0.475 0.0 6.99 -0.76 1.1 15.0
1.0 7.895 -0.475 0.0 6.99 -0.76 1.1 15.0
1.0 7.895 -0.475 0.0 6.99 -0.76 1.1 15.0
1.0 7.895 -0.475 0.0 6.99 -0.76 1.1 15.0
1.0 7.895 -0.475 0.0 6.99 -0.76 1.1 15.0
1.0 7.895 -0.475 0.0 6.99 -0.76 1.1 15.0
1.0 7.895 -0.475 0.0 6.99 -0.76 1.1 15.0
1.0 7.895 -0.475 0.0 6.99 -0.76 1.1 15.0
1.0 7.895 -0.475 0.0 6.99 -0.76 1.1 15.0
1.0 7.895 -0.475 0.0 6.99 -0.76 1.1 15.0
1.0 7.895 -0.475 0.0 6.99 -0.76 1.1 15.0
1.0 7.895 -0.475 0.0 6.99 -0.76 1.1 15.0
1.0 7.895 -0.475 0.0 6.99 -0.76 1.1 15.0
1.0 7.895 -0.475 0.0 6.99 -0.76 1.1 15.0
1.0 7.895 -0.475 0.0 6.99 -0.76 1.1 15.0
1.0 7.895 -0.475 0.0 6.99 -0.76 1.1 15.0
1.0 7.895 -0.475 0.0 6.99 -0.76 1.1 15.0
1.0 7.895 -0.475 0.0 6.99 -0.76 1.1 15.0
1.0 7.895 -0.475 0.0 6.99 -0.76 1.1 15.0
1.0 7.895 -0.475 0.0 6.99 -0.76 1.1 15.0
1
24
1,2,3,4,5,6,7,8,9,10,11,12,13,14,15,16,17,18,19,20,21,22,23,24
7                                    !Experiment 7
1.0 7.895 -0.475 0.0 6.99 -0.76 1.1 15.0
1.0 7.895 -0.475 0.0 6.99 -0.76 1.1 15.0
1.0 7.895 -0.475 0.0 6.99 -0.76 1.1 15.0
1.0 7.895 -0.475 0.0 6.99 -0.76 1.1 15.0
```

```
1.0 7.895 -0.475 0.0 6.99 -0.76 1.1 15.0
1.0 7.895 -0.475 0.0 6.99 -0.76 1.1 15.0
1.0 7.895 -0.475 0.0 6.99 -0.76 1.1 15.0
1.0 7.895 -0.475 0.0 6.99 -0.76 1.1 15.0
1.0 7.895 -0.475 0.0 6.99 -0.76 1.1 15.0
1.0 7.895 -0.475 0.0 6.99 -0.76 1.1 15.0
1.0 7.895 -0.475 0.0 6.99 -0.76 1.1 15.0
1.0 7.895 -0.475 0.0 6.99 -0.76 1.1 15.0
1.0 7.895 -0.475 0.0 6.99 -0.76 1.1 15.0
1.0 7.895 -0.475 0.0 6.99 -0.76 1.1 15.0
1.0 7.895 -0.475 0.0 6.99 -0.76 1.1 15.0
1.0 7.895 -0.475 0.0 6.99 -0.76 1.1 15.0
1.0 7.895 -0.475 0.0 6.99 -0.76 1.1 15.0
1.0 7.895 -0.475 0.0 6.99 -0.76 1.1 15.0
1.0 7.895 -0.475 0.0 6.99 -0.76 1.1 15.0
1.0 7.895 -0.475 0.0 6.99 -0.76 1.1 15.0
1.0 7.895 -0.475 0.0 6.99 -0.76 1.1 15.0
1.0 7.895 -0.475 0.0 6.99 -0.76 1.1 15.0
1.0 7.895 -0.475 0.0 6.99 -0.76 1.1 15.0
1
24
1,2,3,4,5,6,7,8,9,10,11,12,13,14,15,16,17,18,19,20,21,22,23,24
0
OP,REST              ! Restart at this point reading the matrix elements from .me file
0,0
OP,MINI              ! Operation used to perform the Chi^2 minimiazation in GOSIA2
2110,2,99999999,.00001,1.1,0,20,1,0,0.0001
OP,EXIT

! The minimization part of the GOSIA file is replaced with the following operation for integration

OP,INTI   ! Calculates accurate yields of de-exciting gamma rays after Coulomb Excitation
14,14,229.03,290.07,18.17,31.7                                  ! Energy and Theta range for Experiment 1
227,232,237,242,247,252,257,262,267,272,277,282,287,292         ! Energy meshpoints
18.17,19.21,20.25,21.29,22.33,23.37,24.41,25.46,26.50,27.54,28.58,29.62,30.66,31.70   ! Theta meshpoints
14,14,229.03,290.07,31.75,42.3                                  ! Experiment 2
227,232,237,242,247,252,257,262,267,272,277,282,287,292
31.75,32.56,33.37,34.18,35.00,35.81,36.62,37.43,38.24,39.05,39.87,40.68,41.49,42.30
14,14,229.03,290.07,42.35,50.26                                 ! Experiment 3
227,232,237,242,247,252,257,262,267,272,277,282,287,292
42.35,42.96,43.57,44.18,44.78,45.39,46.00,46.61,47.22,47.83,48.43,49.04,49.65,50.26
14,14,229.03,290.07,50.27,56.21                                 ! Experiment 4
227,232,237,242,247,252,257,262,267,272,277,282,287,292
50.27,50.73,51.18,51.64,52.10,52.55,53.01,53.47,53.93,54.38,54.84,55.30,55.75,56.21
14,14,229.03,290.07,21.88,31.67                                 ! Experiment 5
227,232,237,242,247,252,257,262,267,272,277,282,287,292
21.70,22.47,23.24,24.01,24.78,25.55,26.32,27.08,27.85,28.62,29.39,30.16,30.93,31.70
14,14,229.03,290.07,31.82,39.89                                 ! Experiment 6
227,232,237,242,247,252,257,262,267,272,277,282,287,292
31.75,32.38,33.01,33.64,34.26,34.89,35.52,36.15,36.78,37.41,38.03,38.66,39.29,39.92
14,14,229.03,290.07,40.02,46.53                                 ! Experiment 7
227,232,237,242,247,252,257,262,267,272,277,282,287,292
39.95,40.46,40.97,41.48,42.00,42.51,43.02,43.53,44.04,44.55,45.07,45.58,46.09,46.60
14                                                    ! Experiment 1 stopping powers
227,232,237,242,247,252,257,262,267,272,277,282,287,292
15.46,15.44,15.41,15.38,15.35,15.32,15.28,15.25,15.21,15.18,15.14,15.11,15.07,15.03
50,50
14                                                    ! Experiment 2 stopping powers
227,232,237,242,247,252,257,262,267,272,277,282,287,292
15.46,15.44,15.41,15.38,15.35,15.32,15.28,15.25,15.21,15.18,15.14,15.11,15.07,15.03
50,50
14                                                    ! Experiment 3 stopping powers
227,232,237,242,247,252,257,262,267,272,277,282,287,292
15.46,15.44,15.41,15.38,15.35,15.32,15.28,15.25,15.21,15.18,15.14,15.11,15.07,15.03
50,50
14                                                    ! Experiment 4 stopping powers
227,232,237,242,247,252,257,262,267,272,277,282,287,292
15.46,15.44,15.41,15.38,15.35,15.32,15.28,15.25,15.21,15.18,15.14,15.11,15.07,15.03
50,50
14                                                    ! Experiment 5 stopping powers
227,232,237,242,247,252,257,262,267,272,277,282,287,292
15.46,15.44,15.41,15.38,15.35,15.32,15.28,15.25,15.21,15.18,15.14,15.11,15.07,15.03
50,50
14                                                    ! Experiment 6 stopping powers
```

```
227,232,237,242,247,252,257,262,267,272,277,282,287,292
15.46,15.44,15.41,15.38,15.35,15.32,15.28,15.25,15.21,15.18,15.14,15.11,15.07,15.03
50,50
14                                                              ! Experiment 7 stopping powers
227,232,237,242,247,252,257,262,267,272,277,282,287,292
15.46,15.44,15.41,15.38,15.35,15.32,15.28,15.25,15.21,15.18,15.14,15.11,15.07,15.03
50,50
OP,CORR
OP,EXIT
```

66Ge_on_196Pt_target_290.07MeV.inp

```
2
OP,FILE
22,3,1
66Ge_on_196Pt_target.out
25,3,1
66Ge_on_196Pt.inp
26,3,1
66Ge_on_196Pt_target.inp
9,3,1
miniball.f9
8,3,1
miniball.f8
3,3,1
196Pt.yie
4,3,1
196Pt.cor
7,3,1
66Ge.map
27,3,1
196Pt.map
12,3,1
66Ge.bst
32,3,1
196Pt.bst
29,3,1
196Pt.bricc
0,0,0
OP,TITL
        Target Excitation of 196Pt with 66Ge beam @ 4.395 MeV/u
OP,GOSI              ! This operation is used to define the nucleus to be studied
LEVE                ! The level scheme used for the calculation is defined in this section
1,1,0,0.0
2,1,2,0.3557
3,1,2,0.6887
4,1,4,0.8769
5,1,3,1.015
6,1,0,1.1353
7,1,4,1.2933
8,-1,3,1.4470
9,1,6,1.5258
10,-1,5,1.2703
0,0,0,0
ME                  ! Construct the matrix elements between the levels defined in LEVE
1,0,0,0,0           ! E1 matrix elements
2,8,0.000152,0.002,0.002
3,8,0.000117,0.002,0.002
4,8,0.0000872,0.002,0.002
4,10,0.000839,0.002,0.002
5,8,0.000180,0.002,0.002
2,0,0,0,0           ! E2 matrix elements
1,2,1.1697,-2,2
1,3,0.00037,1,1
2,2,0.8179,-2,2
2,3,1.3522,2,2
```

```
2,4,1.9109,3,3
2,6,0.1381,2,2
2,7,0.1846,2,2
3,3,0.5146,2,2
3,4,0.002,2,2
3,5,0.49608,2,2
3,6,0.3472,2,2
3,7,1.3406,3,3
4,4,0.084,2,2
4,7,1.0121,3,3
4,9,2.5333,1,1
5,5,0.002,2,2
7,7,0.002,2,2
7,9,0.002,2,2
8,8,0.002,2,2
8,10,0.4407,2,2
9,9,0.002,2,2
10,10,0.002,2,2
3,0,0,0,0              ! E3 matrix elements
1,8,0.307,2,2
2,10,0.2603,2,2
7,0,0,0,0             ! M1 matrix elements
2,3,-0.072,2,2
2,5,-0.00968,2,2
4,5,-0.02925,2,2
4,7,-0.34382,2,2
8,0,0,0,0             ! M2 matrix elements
4,8,1.184,4,4
5,8,3.18,4,4
0,0,0,0,0
EXPT                 ! Experimental conditions of the experiments to be run
7,78,196
32,66,290.07,24.93,5,1,0,0,360,1,1 !1
32,66,290.07,37.05,5,1,0,0,360,1,1 !2
32,66,290.07,46.30,5,1,0,0,360,1,1 !3
32,66,290.07,53.24,5,1,0,0,360,1,1 !4
32,66,290.07,-26.775,5,1,0,0,360,1,1 !5
32,66,290.07,-35.855,5,1,0,0,360,1,1 !6
32,66,290.07,-43.275,5,1,0,0,360,1,1 !7
CONT
SPL,1.          ! Cubic spline interpolation used instead of Lagrange
EFF,7.          ! Defines the efficiency curve from RADWARE parameters
1,4
2,4
3,4
4,4
5,4
6,4
7,4
INT,7.
1,1000
2,1000
3,1000
4,1000
5,1000
6,1000
7,1000
PRT,
1,-1
2,0
4,0
5,1
11,0
12,0
14,0
16,0
18,1
0,0
END,
                 ! KEEP THIS LINE EMPTY
OP,BRIC          ! Get the internal conversion coefficients from BRICC database
/home/kenzo/Gosia/66Ge_Gosia2/frontback66Ge/BrIccFOV22.idx
/home/kenzo/Gosia/66Ge_Gosia2/frontback66Ge/BrIccFOV22.icc
OP,YIEL          ! Calculates the yields of de-exciting gamma rays after Coulomb Excitation
0
```

```
-1,0
0.010
24,24,24,24,24,24,24                          ! 7 experiments with 24 detectors for each
1,1,1,1,1,1,1,1,1,1,1,1,1,1,1,1,1,1,1,1,1,1,1,1
142.9, 109.6, 118.6, 46.8, 47.6, 74.5, 67.9, 39.1, 69.7,146.7,113.4,117,111.4,143.5,115.8,44.9,42.9,70.2,131.6,132.4,107.7,63.5,38.8,69.1  ! Theta angle
131.5,127.4,162.8,22.4,69.1,45.1,126.4,146.5,161.6,38,24.7,62.9,243.7,232.2,207.6,196.9,245.1,222.5,342.7,302.1,321.8,316.2,341.1,349.7    ! Phi angle
1,1,1,1,1,1,1,1,1,1,1,1,1,1,1,1,1,1,1,1,1,1,1,1
142.9,109.6,118.6,46.8,47.6,74.5,67.9,39.1,69.7,146.7,113.4,117,111.4,143.5,115.8,44.9,42.9,70.2,131.6,132.4,107.7,63.5,38.8,69.1
131.5,127.4,162.8,22.4,69.1,45.1,126.4,146.5,161.6,38,24.7,62.9,243.7,232.2,207.6,196.9,245.1,222.5,342.7,302.1,321.8,316.2,341.1,349.7
1,1,1,1,1,1,1,1,1,1,1,1,1,1,1,1,1,1,1,1,1,1,1,1
142.9,109.6,118.6,46.8,47.6,74.5,67.9,39.1,69.7,146.7,113.4,117,111.4,143.5,115.8,44.9,42.9,70.2,131.6,132.4,107.7,63.5,38.8,69.1
131.5,127.4,162.8,22.4,69.1,45.1,126.4,146.5,161.6,38,24.7,62.9,243.7,232.2,207.6,196.9,245.1,222.5,342.7,302.1,321.8,316.2,341.1,349.7
1,1,1,1,1,1,1,1,1,1,1,1,1,1,1,1,1,1,1,1,1,1,1,1
142.9,109.6,118.6,46.8,47.6,74.5,67.9,39.1,69.7,146.7,113.4,117,111.4,143.5,115.8,44.9,42.9,70.2,131.6,132.4,107.7,63.5,38.8,69.1
131.5,127.4,162.8,22.4,69.1,45.1,126.4,146.5,161.6,38,24.7,62.9,243.7,232.2,207.6,196.9,245.1,222.5,342.7,302.1,321.8,316.2,341.1,349.7
1,1,1,1,1,1,1,1,1,1,1,1,1,1,1,1,1,1,1,1,1,1,1,1
142.9,109.6,118.6,46.8,47.6,74.5,67.9,39.1,69.7,146.7,113.4,117,111.4,143.5,115.8,44.9,42.9,70.2,131.6,132.4,107.7,63.5,38.8,69.1
131.5,127.4,162.8,22.4,69.1,45.1,126.4,146.5,161.6,38,24.7,62.9,243.7,232.2,207.6,196.9,245.1,222.5,342.7,302.1,321.8,316.2,341.1,349.7
1,1,1,1,1,1,1,1,1,1,1,1,1,1,1,1,1,1,1,1,1,1,1,1
142.9,109.6,118.6,46.8,47.6,74.5,67.9,39.1,69.7,146.7,113.4,117,111.4,143.5,115.8,44.9,42.9,70.2,131.6,132.4,107.7,63.5,38.8,69.1
131.5,127.4,162.8,22.4,69.1,45.1,126.4,146.5,161.6,38,24.7,62.9,243.7,232.2,207.6,196.9,245.1,222.5,342.7,302.1,321.8,316.2,341.1,349.7
1,1,1,1,1,1,1,1,1,1,1,1,1,1,1,1,1,1,1,1,1,1,1,1
142.9,109.6,118.6,46.8,47.6,74.5,67.9,39.1,69.7,146.7,113.4,117,111.4,143.5,115.8,44.9,42.9,70.2,131.6,132.4,107.7,63.5,38.8,69.1
131.5,127.4,162.8,22.4,69.1,45.1,126.4,146.5,161.6,38,24.7,62.9,243.7,232.2,207.6,196.9,245.1,222.5,342.7,302.1,321.8,316.2,341.1,349.7
2,1              ! Transition for normalization of the gamma yields
1               !1
10000000000.0
1
1               !2
10000000000.0
1
1               !3
10000000000.0
1
1               !4
10000000000.0
1
1               !5
10000000000.0
1
1               !6
10000000000.0
1
1               !7
10000000000.0
1
4               ! This variable determines which file contains the gamma ray yields. 0 means no file is needed.
0,0
1,1                                              ! Defines the half-life of a state
2,49.27,0.22    ! life-time for index 2, life-time in ps, uncertainty in life-time
0,0
1,1             ! Defines a matrix element as a data point
2,2,2,0.82,0.10 !
OP,RAW          ! Defines the efficiency curve for the gamma ray yields
1                                    !Experiment 1
1.0 7.895 -0.475 0.0 6.99 -0.76 1.1 15.0
1.0 7.895 -0.475 0.0 6.99 -0.76 1.1 15.0
1.0 7.895 -0.475 0.0 6.99 -0.76 1.1 15.0
1.0 7.895 -0.475 0.0 6.99 -0.76 1.1 15.0
1.0 7.895 -0.475 0.0 6.99 -0.76 1.1 15.0
1.0 7.895 -0.475 0.0 6.99 -0.76 1.1 15.0
1.0 7.895 -0.475 0.0 6.99 -0.76 1.1 15.0
1.0 7.895 -0.475 0.0 6.99 -0.76 1.1 15.0
1.0 7.895 -0.475 0.0 6.99 -0.76 1.1 15.0
1.0 7.895 -0.475 0.0 6.99 -0.76 1.1 15.0
1.0 7.895 -0.475 0.0 6.99 -0.76 1.1 15.0
1.0 7.895 -0.475 0.0 6.99 -0.76 1.1 15.0
1.0 7.895 -0.475 0.0 6.99 -0.76 1.1 15.0
1.0 7.895 -0.475 0.0 6.99 -0.76 1.1 15.0
1.0 7.895 -0.475 0.0 6.99 -0.76 1.1 15.0
1.0 7.895 -0.475 0.0 6.99 -0.76 1.1 15.0
1.0 7.895 -0.475 0.0 6.99 -0.76 1.1 15.0
1.0 7.895 -0.475 0.0 6.99 -0.76 1.1 15.0
1.0 7.895 -0.475 0.0 6.99 -0.76 1.1 15.0
1.0 7.895 -0.475 0.0 6.99 -0.76 1.1 15.0
```

```
1.0 7.895 -0.475 0.0 6.99 -0.76 1.1 15.0
1.0 7.895 -0.475 0.0 6.99 -0.76 1.1 15.0
1.0 7.895 -0.475 0.0 6.99 -0.76 1.1 15.0
1.0 7.895 -0.475 0.0 6.99 -0.76 1.1 15.0
1
24
1,2,3,4,5,6,7,8,9,10,11,12,13,14,15,16,17,18,19,20,21,22,23,24
2                                         !Experiment 2
1.0 7.895 -0.475 0.0 6.99 -0.76 1.1 15.0
1.0 7.895 -0.475 0.0 6.99 -0.76 1.1 15.0
1.0 7.895 -0.475 0.0 6.99 -0.76 1.1 15.0
1.0 7.895 -0.475 0.0 6.99 -0.76 1.1 15.0
1.0 7.895 -0.475 0.0 6.99 -0.76 1.1 15.0
1.0 7.895 -0.475 0.0 6.99 -0.76 1.1 15.0
1.0 7.895 -0.475 0.0 6.99 -0.76 1.1 15.0
1.0 7.895 -0.475 0.0 6.99 -0.76 1.1 15.0
1.0 7.895 -0.475 0.0 6.99 -0.76 1.1 15.0
1.0 7.895 -0.475 0.0 6.99 -0.76 1.1 15.0
1.0 7.895 -0.475 0.0 6.99 -0.76 1.1 15.0
1.0 7.895 -0.475 0.0 6.99 -0.76 1.1 15.0
1.0 7.895 -0.475 0.0 6.99 -0.76 1.1 15.0
1.0 7.895 -0.475 0.0 6.99 -0.76 1.1 15.0
1.0 7.895 -0.475 0.0 6.99 -0.76 1.1 15.0
1.0 7.895 -0.475 0.0 6.99 -0.76 1.1 15.0
1.0 7.895 -0.475 0.0 6.99 -0.76 1.1 15.0
1.0 7.895 -0.475 0.0 6.99 -0.76 1.1 15.0
1.0 7.895 -0.475 0.0 6.99 -0.76 1.1 15.0
1.0 7.895 -0.475 0.0 6.99 -0.76 1.1 15.0
1.0 7.895 -0.475 0.0 6.99 -0.76 1.1 15.0
1.0 7.895 -0.475 0.0 6.99 -0.76 1.1 15.0
1
24
1,2,3,4,5,6,7,8,9,10,11,12,13,14,15,16,17,18,19,20,21,22,23,24
3                                         !Experiment 3
1.0 7.895 -0.475 0.0 6.99 -0.76 1.1 15.0
1.0 7.895 -0.475 0.0 6.99 -0.76 1.1 15.0
1.0 7.895 -0.475 0.0 6.99 -0.76 1.1 15.0
1.0 7.895 -0.475 0.0 6.99 -0.76 1.1 15.0
1.0 7.895 -0.475 0.0 6.99 -0.76 1.1 15.0
1.0 7.895 -0.475 0.0 6.99 -0.76 1.1 15.0
1.0 7.895 -0.475 0.0 6.99 -0.76 1.1 15.0
1.0 7.895 -0.475 0.0 6.99 -0.76 1.1 15.0
1.0 7.895 -0.475 0.0 6.99 -0.76 1.1 15.0
1.0 7.895 -0.475 0.0 6.99 -0.76 1.1 15.0
1.0 7.895 -0.475 0.0 6.99 -0.76 1.1 15.0
1.0 7.895 -0.475 0.0 6.99 -0.76 1.1 15.0
1.0 7.895 -0.475 0.0 6.99 -0.76 1.1 15.0
1.0 7.895 -0.475 0.0 6.99 -0.76 1.1 15.0
1.0 7.895 -0.475 0.0 6.99 -0.76 1.1 15.0
1.0 7.895 -0.475 0.0 6.99 -0.76 1.1 15.0
1.0 7.895 -0.475 0.0 6.99 -0.76 1.1 15.0
1.0 7.895 -0.475 0.0 6.99 -0.76 1.1 15.0
1.0 7.895 -0.475 0.0 6.99 -0.76 1.1 15.0
1.0 7.895 -0.475 0.0 6.99 -0.76 1.1 15.0
1.0 7.895 -0.475 0.0 6.99 -0.76 1.1 15.0
1.0 7.895 -0.475 0.0 6.99 -0.76 1.1 15.0
1.0 7.895 -0.475 0.0 6.99 -0.76 1.1 15.0
1
24
1,2,3,4,5,6,7,8,9,10,11,12,13,14,15,16,17,18,19,20,21,22,23,24
4                                         !Experiment 4
1.0 7.895 -0.475 0.0 6.99 -0.76 1.1 15.0
1.0 7.895 -0.475 0.0 6.99 -0.76 1.1 15.0
1.0 7.895 -0.475 0.0 6.99 -0.76 1.1 15.0
1.0 7.895 -0.475 0.0 6.99 -0.76 1.1 15.0
1.0 7.895 -0.475 0.0 6.99 -0.76 1.1 15.0
1.0 7.895 -0.475 0.0 6.99 -0.76 1.1 15.0
1.0 7.895 -0.475 0.0 6.99 -0.76 1.1 15.0
1.0 7.895 -0.475 0.0 6.99 -0.76 1.1 15.0
1.0 7.895 -0.475 0.0 6.99 -0.76 1.1 15.0
1.0 7.895 -0.475 0.0 6.99 -0.76 1.1 15.0
1.0 7.895 -0.475 0.0 6.99 -0.76 1.1 15.0
```
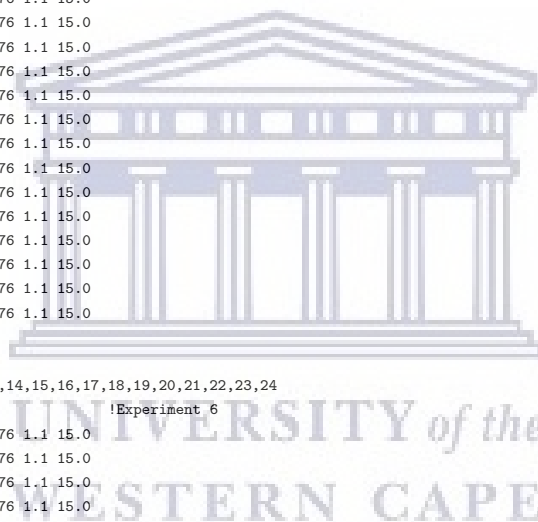
```
1.0 7.895 -0.475 0.0 6.99 -0.76 1.1 15.0
1.0 7.895 -0.475 0.0 6.99 -0.76 1.1 15.0
1.0 7.895 -0.475 0.0 6.99 -0.76 1.1 15.0
1.0 7.895 -0.475 0.0 6.99 -0.76 1.1 15.0
1.0 7.895 -0.475 0.0 6.99 -0.76 1.1 15.0
1.0 7.895 -0.475 0.0 6.99 -0.76 1.1 15.0
1.0 7.895 -0.475 0.0 6.99 -0.76 1.1 15.0
1.0 7.895 -0.475 0.0 6.99 -0.76 1.1 15.0
1.0 7.895 -0.475 0.0 6.99 -0.76 1.1 15.0
1.0 7.895 -0.475 0.0 6.99 -0.76 1.1 15.0
1.0 7.895 -0.475 0.0 6.99 -0.76 1.1 15.0
1.0 7.895 -0.475 0.0 6.99 -0.76 1.1 15.0
1.0 7.895 -0.475 0.0 6.99 -0.76 1.1 15.0
1
24
1,2,3,4,5,6,7,8,9,10,11,12,13,14,15,16,17,18,19,20,21,22,23,24
5                                       !Experiment 5
1.0 7.895 -0.475 0.0 6.99 -0.76 1.1 15.0
1.0 7.895 -0.475 0.0 6.99 -0.76 1.1 15.0
1.0 7.895 -0.475 0.0 6.99 -0.76 1.1 15.0
1.0 7.895 -0.475 0.0 6.99 -0.76 1.1 15.0
1.0 7.895 -0.475 0.0 6.99 -0.76 1.1 15.0
1.0 7.895 -0.475 0.0 6.99 -0.76 1.1 15.0
1.0 7.895 -0.475 0.0 6.99 -0.76 1.1 15.0
1.0 7.895 -0.475 0.0 6.99 -0.76 1.1 15.0
1.0 7.895 -0.475 0.0 6.99 -0.76 1.1 15.0
1.0 7.895 -0.475 0.0 6.99 -0.76 1.1 15.0
1.0 7.895 -0.475 0.0 6.99 -0.76 1.1 15.0
1.0 7.895 -0.475 0.0 6.99 -0.76 1.1 15.0
1.0 7.895 -0.475 0.0 6.99 -0.76 1.1 15.0
1.0 7.895 -0.475 0.0 6.99 -0.76 1.1 15.0
1.0 7.895 -0.475 0.0 6.99 -0.76 1.1 15.0
1.0 7.895 -0.475 0.0 6.99 -0.76 1.1 15.0
1.0 7.895 -0.475 0.0 6.99 -0.76 1.1 15.0
1.0 7.895 -0.475 0.0 6.99 -0.76 1.1 15.0
1.0 7.895 -0.475 0.0 6.99 -0.76 1.1 15.0
1.0 7.895 -0.475 0.0 6.99 -0.76 1.1 15.0
1.0 7.895 -0.475 0.0 6.99 -0.76 1.1 15.0
1.0 7.895 -0.475 0.0 6.99 -0.76 1.1 15.0
1.0 7.895 -0.475 0.0 6.99 -0.76 1.1 15.0
1.0 7.895 -0.475 0.0 6.99 -0.76 1.1 15.0
1
24
1,2,3,4,5,6,7,8,9,10,11,12,13,14,15,16,17,18,19,20,21,22,23,24
6                                       !Experiment 6
1.0 7.895 -0.475 0.0 6.99 -0.76 1.1 15.0
1.0 7.895 -0.475 0.0 6.99 -0.76 1.1 15.0
1.0 7.895 -0.475 0.0 6.99 -0.76 1.1 15.0
1.0 7.895 -0.475 0.0 6.99 -0.76 1.1 15.0
1.0 7.895 -0.475 0.0 6.99 -0.76 1.1 15.0
1.0 7.895 -0.475 0.0 6.99 -0.76 1.1 15.0
1.0 7.895 -0.475 0.0 6.99 -0.76 1.1 15.0
1.0 7.895 -0.475 0.0 6.99 -0.76 1.1 15.0
1.0 7.895 -0.475 0.0 6.99 -0.76 1.1 15.0
1.0 7.895 -0.475 0.0 6.99 -0.76 1.1 15.0
1.0 7.895 -0.475 0.0 6.99 -0.76 1.1 15.0
1.0 7.895 -0.475 0.0 6.99 -0.76 1.1 15.0
1.0 7.895 -0.475 0.0 6.99 -0.76 1.1 15.0
1.0 7.895 -0.475 0.0 6.99 -0.76 1.1 15.0
1.0 7.895 -0.475 0.0 6.99 -0.76 1.1 15.0
1.0 7.895 -0.475 0.0 6.99 -0.76 1.1 15.0
1.0 7.895 -0.475 0.0 6.99 -0.76 1.1 15.0
1.0 7.895 -0.475 0.0 6.99 -0.76 1.1 15.0
1.0 7.895 -0.475 0.0 6.99 -0.76 1.1 15.0
1.0 7.895 -0.475 0.0 6.99 -0.76 1.1 15.0
1.0 7.895 -0.475 0.0 6.99 -0.76 1.1 15.0
1.0 7.895 -0.475 0.0 6.99 -0.76 1.1 15.0
1.0 7.895 -0.475 0.0 6.99 -0.76 1.1 15.0
1
24
1,2,3,4,5,6,7,8,9,10,11,12,13,14,15,16,17,18,19,20,21,22,23,24
7                                       !Experiment 7
1.0 7.895 -0.475 0.0 6.99 -0.76 1.1 15.0
1.0 7.895 -0.475 0.0 6.99 -0.76 1.1 15.0
```

```
1.0 7.895 -0.475 0.0 6.99 -0.76 1.1 15.0
1.0 7.895 -0.475 0.0 6.99 -0.76 1.1 15.0
1.0 7.895 -0.475 0.0 6.99 -0.76 1.1 15.0
1.0 7.895 -0.475 0.0 6.99 -0.76 1.1 15.0
1.0 7.895 -0.475 0.0 6.99 -0.76 1.1 15.0
1.0 7.895 -0.475 0.0 6.99 -0.76 1.1 15.0
1.0 7.895 -0.475 0.0 6.99 -0.76 1.1 15.0
1.0 7.895 -0.475 0.0 6.99 -0.76 1.1 15.0
1.0 7.895 -0.475 0.0 6.99 -0.76 1.1 15.0
1.0 7.895 -0.475 0.0 6.99 -0.76 1.1 15.0
1.0 7.895 -0.475 0.0 6.99 -0.76 1.1 15.0
1.0 7.895 -0.475 0.0 6.99 -0.76 1.1 15.0
1.0 7.895 -0.475 0.0 6.99 -0.76 1.1 15.0
1.0 7.895 -0.475 0.0 6.99 -0.76 1.1 15.0
1.0 7.895 -0.475 0.0 6.99 -0.76 1.1 15.0
1.0 7.895 -0.475 0.0 6.99 -0.76 1.1 15.0
1.0 7.895 -0.475 0.0 6.99 -0.76 1.1 15.0
1.0 7.895 -0.475 0.0 6.99 -0.76 1.1 15.0
1.0 7.895 -0.475 0.0 6.99 -0.76 1.1 15.0
1.0 7.895 -0.475 0.0 6.99 -0.76 1.1 15.0
1.0 7.895 -0.475 0.0 6.99 -0.76 1.1 15.0
1
24
1,2,3,4,5,6,7,8,9,10,11,12,13,14,15,16,17,18,19,20,21,22,23,24
0
OP,REST          ! Restart at this point reading the matrix elements from .me file
0,0
OP,MINI          ! Operation used to perform the Chi^2 minimiazation in GOSIA2
2110,10,.0001,.00001,1.1,0,20,1,0,0.0001
OP,EXIT


! The minimization part of the GOSIA file is replaced with the following operation for integration

OP,INTI                          ! Calculates accurate yields of de-exciting gamma rays after Coulomb Excitation
14,14,229.03,290.07,18.17,31.7                                          ! Energy and Theta range for Experiment 1
227,232,237,242,247,252,257,262,267,272,277,282,287,292                 ! Energy meshpoints
18.17,19.21,20.25,21.29,22.33,23.37,24.41,25.46,26.50,27.54,28.58,29.62,30.66,31.70   ! Theta meshpoints
14,14,229.03,290.07,31.75,42.3                                          ! Experiment 2
227,232,237,242,247,252,257,262,267,272,277,282,287,292
31.75,32.56,33.37,34.18,35.00,35.81,36.62,37.43,38.24,39.05,39.87,40.68,41.49,42.30
14,14,229.03,290.07,42.35,50.26                                         ! Experiment 3
227,232,237,242,247,252,257,262,267,272,277,282,287,292
42.35,42.96,43.57,44.18,44.78,45.39,46.00,46.61,47.22,47.83,48.43,49.04,49.65,50.26
14,14,229.03,290.07,50.27,56.21                                         ! Experiment 4
227,232,237,242,247,252,257,262,267,272,277,282,287,292
50.27,50.73,51.18,51.64,52.10,52.55,53.01,53.47,53.93,54.38,54.84,55.30,55.75,56.21
14,14,229.03,290.07,21.88,31.67                                         ! Experiment 5
227,232,237,242,247,252,257,262,267,272,277,282,287,292
21.70,22.47,23.24,24.01,24.78,25.55,26.32,27.08,27.85,28.62,29.39,30.16,30.93,31.70
14,14,229.03,290.07,31.82,39.89                                        ! Experiment 6
227,232,237,242,247,252,257,262,267,272,277,282,287,292
31.75,32.38,33.01,33.64,34.26,34.89,35.52,36.15,36.78,37.41,38.03,38.66,39.29,39.92
14,14,229.03,290.07,40.02,46.53                                        ! Experiment 7
227,232,237,242,247,252,257,262,267,272,277,282,287,292
39.95,40.46,40.97,41.48,42.00,42.51,43.02,43.53,44.04,44.55,45.07,45.58,46.09,46.60
14                                                                     ! Experiment 1 stopping powers
227,232,237,242,247,252,257,262,267,272,277,282,287,292
15.46,15.44,15.41,15.38,15.35,15.32,15.28,15.25,15.21,15.18,15.14,15.11,15.07,15.03
50,50
14                                                                     ! Experiment 2 stopping powers
227,232,237,242,247,252,257,262,267,272,277,282,287,292
15.46,15.44,15.41,15.38,15.35,15.32,15.28,15.25,15.21,15.18,15.14,15.11,15.07,15.03
50,50
14                                                                     ! Experiment 3 stopping powers
227,232,237,242,247,252,257,262,267,272,277,282,287,292
15.46,15.44,15.41,15.38,15.35,15.32,15.28,15.25,15.21,15.18,15.14,15.11,15.07,15.03
50,50
14                                                                     ! Experiment 4 stopping powers
227,232,237,242,247,252,257,262,267,272,277,282,287,292
15.46,15.44,15.41,15.38,15.35,15.32,15.28,15.25,15.21,15.18,15.14,15.11,15.07,15.03
50,50
14                                                                     ! Experiment 5 stopping powers
227,232,237,242,247,252,257,262,267,272,277,282,287,292
15.46,15.44,15.41,15.38,15.35,15.32,15.28,15.25,15.21,15.18,15.14,15.11,15.07,15.03
```

```
50,50
14                                                                    ! Experiment 6 stopping powers
227,232,237,242,247,252,257,262,267,272,277,282,287,292
15.46,15.44,15.41,15.38,15.35,15.32,15.28,15.25,15.21,15.18,15.14,15.11,15.07,15.03
50,50
14                                                                    ! Experiment 7 stopping powers
227,232,237,242,247,252,257,262,267,272,277,282,287,292
15.46,15.44,15.41,15.38,15.35,15.32,15.28,15.25,15.21,15.18,15.14,15.11,15.07,15.03
50,50
OP,CORR
OP,EXIT
```

Bibliography

[1] National Nuclear Data Center. National Nuclear Data Center, . Available: https://www.nndc.bnl.gov/.

[2] National Nuclear Data Center. Adopted B(E2) Values, . Available: https://www.nndc.bnl.gov/be2/adopted.jsp.

[3] K. Starosta, A. Dewald, A. Dunomes, P. Adrich, A. M. Amthor, T. Baumann, D. Bazin, M. Bowen, B. A. Brown, A. Chester, A. Gade, D. Galaviz, T. Glasmacher, T. Ginter, M. Hausmann, M. Horoi, J. Jolie, B. Melon, D. Miller, V. Moeller, R. P. Norris, T. Pissulla, M. Portillo, W. Rother, Y. Shimbara, A. Stolz, C. Vaman, P. Voss, D. Weisshaar, and V. Zelevinsky. Shape and Structure of $N = Z$ ^{64}Ge: Electromagnetic Transition Rates from the Application of the Recoil Distance Method to a Knockout Reaction. *Phys. Rev. Lett.*, 99:042503, 2007.

[4] E. Kugler, D. Fiander, B. Jonson, H. Haas, A. Przewloka, H. L. Ravn, D. J. Simon, and K. Zimmer. The new CERN-ISOLDE on-line mass-separator facility at the PS-Booster. *Nuclear Instruments and Methods in Physics Research B*, 70:41–49, 1992.

[5] Y Kadi, M A Fraser, and A Papageorgiou-Koufidou. *HIE-ISOLDE: technical design report for the energy upgrade.* CERN Yellow Reports: Monographs. CERN, Geneva, May 2018.

[6] M. Grieser, Y. A. Litvinov, R. Raabe, K. Blaum, et al. Storage ring at HIE-ISOLDE. *The European Physical Journal Special Topics*, 207:1–117, 2012.

[7] M. J. G. Borge and K. Riisager. HIE-ISOLDE, the project and the physics opportunities. *The European Physical Journal A*, 52, 2016.

[8] J. M. Ordan and CERN. ISOLDE Experiment July 2017. https://cds.cern.ch/record/2273290. Accessed: 2020-04-22.

[9] N. Warr, J. Van de Walle, M. Albers, et al. The Miniball Spectrometer. *European Physical Journal. A, Hadrons and Nuclei*, A49:40, 2013.

[10] J. Eberth and J. Simpson. From ge(li) detectors to gamma-ray tracking arrays–50 years of gamma spectroscopy with germanium detectors. *Progress in Particle and Nuclear Physics*, 60(2):283–337, 2008.

[11] R. Lutter, O. Schaile, K. Schoffel, K. Steinberger, P. Thirolf, and C. Broude. MAR_aBO_OU - a MBS and ROOT based online/offline utility. *Nuclear Science, IEEE Transactions on*, 47:280–283, 2000.

[12] M. Honma, T. Otsuka, T. Mizusaki, and M. Hjorth-Jensen. New effective interaction for f_5pg_9-shell nuclei. *Physics Review C*, 80:064323, 2009.

[13] M. Hasegawa, K. Kaneko, and T. Mizusaki. Proton-neutron alignment in the yrast states of ^{66}Ge and ^{68}Ge. *Physics Review C*, 70:031301, 2004.

[14] M. Honma, T. Otsuka, B. A. Brown, and T. Mizusaki. New effective interaction for pf-shell nuclei and its implications for the stability of the $N = Z = 28$ closed core. *Physics Review C*, 69:034335, 2004.

[15] J. P. Delaroche, M. Girod, J. Libert, H. Goutte, S. Hilaire, S. Péru, N. Pillet, and G. F. Bertsch. Structure of even-even nuclei using a mapped collective Hamiltonian and the D1S Gogny interaction. *Physics Review C*, 81:014303, 2010.

[16] S. Salém-Vasconcelos, M. J. Bechara, J. H. Hirata, and O. Dietzsch. Quadrupole moment of the first 2^+ excited state in ^{64}Zn. *Phys. Rev. C*, 38:2439–2442, 1988.

[17] J. de Boer and J. Eichler. *The Reorientation Effect.* Springer US, Boston, MA, 1968.

[18] A. de Shalit and H. Feshbach. *Theoretical Nuclear Physics Vol. 1: Nuclear Structure.* Wiley-Blackwell, 1974.

[19] A. Bohr and B. Mottelson. *Nuclear Structure II.* W.A. Benjamin, 1975.

[20] S. Yeager and L. Zamick. Relations Involving Static Quadrupole Moments of 2+ states and B(E2)'s, 2008. Available: https://arxiv.org/abs/0807.4679v2.

[21] P. Ring and P. Schuck. *The nuclear many-body problem.* Springer-Verlag, New York, 1980.

[22] K. Alder and A. Winther. *Electromagnetic Excitation: Theory of Coulomb Excitation with Heavy Ions.* North-Holland, New York, 1975.

[23] P. Cejnar, J. Jolie, and R.F. Casten. Quantum phase transitions in the shapes of atomic nuclei. *Reviews of Modern Physics*, 82:2155–2212, 2010.

[24] K. Heyde and J.L. Wood. Shape coexistence in atomic nuclei. *Reviews of Modern Physics*, 83:1467–1521, 2011.

[25] E. Bouchez, I. Matea, W. Korten, F. Becker, B. Blank, C. Borcea, A. Buta, A. Emsallem, G. de France, J. Genevey, F. Hannachi, K. Hauschild, A. Hürstel, Y. Le Coz, M. Lewitowicz, R. Lucas, F. Negoita, F. de Oliveira Santos, D. Pantelica, J. Pinston, P. Rahkila, M. Rejmund, M. Stanoiu, and Ch. Theisen. New Shape Isomer in the Self-Conjugate Nucleus ^{72}Kr. *Physics Review Letters*, 90:082502, 2003.

[26] E. Clément, A. Görgen, W. Korten, E. Bouchez, A. Chatillon, J.-P. Delaroche, M. Girod, H. Goutte, A. Hürstel, Y. Le Coz, A. Obertelli, S. Péru, Ch. Theisen, J. N. Wilson, M. Zielińska, C. Andreoiu, F. Becker, P. A. Butler, J. M. Casandjian, W. N. Catford, T. Czosnyka, G. de France, J. Gerl, R.-D. Herzberg, J. Iwanicki, D. G. Jenkins, G. D. Jones, P. J. Napiorkowski, G. Sletten, and C. N. Timis. Shape coexistence in neutron-deficient krypton isotopes. *Physics Review C*, 75:054313, 2007.

[27] A. M. Hurst, P. A. Butler, D. G. Jenkins, P. Delahaye, F. Wenander, F. Ames, C. J. Barton, T. Behrens, A. Bürger, J. Cederkäll, E. Clément, T. Czosnyka, T. Davinson, G. de Angelis, J. Eberth, A. Ekström, S. Franchoo, G. Georgiev, A. Görgen, R.-D. Herzberg, M. Huyse, O. Ivanov, J. Iwanicki, G. D. Jones, P. Kent, U. Köster, T. Kröll, R. Krücken, A. C. Larsen, M. Nespolo, M. Pantea, E. S. Paul, M. Petri, H. Scheit, T. Sieber, S. Siem, J. F. Smith, A. Steer, I. Stefanescu, N. U. H. Syed, J. Van de Walle, P. Van Duppen, R. Wadsworth, N. Warr, D. Weisshaar, and M. Zielińska. Measurement of the Sign of the Spectroscopic Quadrupole Moment for the 2_1^+ State in ^{70}Se: No Evidence for Oblate Shape. *Physics Review Letters*, 98, 2007.

[28] J. Ljungvall, A. Görgen, M. Girod, J.-P. Delaroche, A. Dewald, C. Dossat, E. Farnea, W. Korten, B. Melon, R. Menegazzo, A. Obertelli, R. Orlandi, P. Petkov, T. Pissulla, S. Siem, R. P. Singh, J. Srebrny, Ch. Theisen, C. A. Ur, J. J. Valiente-Dobón, K. O. Zell, and M. Zielińska. Shape Coexistence in Light Se Isotopes: Evidence for Oblate Shapes. *Physics Review Letters*, 100, 2008.

[29] J. Henderson, C. Y. Wu, J. Ash, P. C. Bender, B. Elman, A. Gade, M. Grinder, H. Iwasaki, E. Kwan, B. Longfellow, T. Mijatović, D. Rhodes, M. Spieker, and D. Weisshaar. Localizing the shape transition in neutron-deficient selenium. *Phys. Rev. Lett.*, 121:082502, 2018.

[30] M. Girod, J.-P. Delaroche, A. Görgen, and A. Obertelli. The role of triaxiality for the coexistence and evolution of shapes in light krypton isotopes. *Physics Letters B*, 676(1):39–43, 2009.

[31] K. Sato and N. Hinohara. Shape mixing dynamics in the low-lying states of proton-rich Kr isotopes. *Nuclear Physics A*, 849(1):53–71, 2011.

[32] M. Bender, P. Bonche, and P.-H. Heenen. Shape coexistence in neutron-deficient kr isotopes: Constraints on the single-particle spectrum of self-consistent mean-field models from collective excitations. *Phys. Rev. C*, 74:024312, 2006.

[33] M. Sugawara, Y. Toh, T. Czosnyka, M. Oshima, Takehito Hayakawa, H. Kusakari, Yuichi Hatsukawa, Jun-ichi Katakura, M. Matsuda, T. Morikawa, A. Seki, and F. Sakata. Multiple Coulomb excitation interpretation of the ^{70}Ge beam and the interpretation of the O$_2^+$ as a deformed intruder. *European Physical Journal A*, 16: 409–414, 01 2003.

[34] A.D. Ayangeakaa, R.V.F. Janssens, C.Y. Wu, J.M. Allmond, J.L. Wood, S. Zhu, M. Albers, S. Almaraz-Calderon, B. Bucher, M.P. Carpenter, C.J. Chiara, D. Cline, H.L. Crawford, H.M. David, J. Harker, A.B. Hayes, C.R. Hoffman, B.P. Kay, K. Kolos, A. Korichi, T. Lauritsen, A.O. Macchiavelli, A. Richard, D. Seweryniak, and A. Wiens. Shape coexistence and the role of axial asymmetry in 72ge. *Physics Letters B*, 754:254–259, 2016.

[35] A. D. Ayangeakaa, R. V. F. Janssens, S. Zhu, D. Little, J. Henderson, C. Y. Wu, D. J. Hartley, M. Albers, K. Auranen, B. Bucher, M. P. Carpenter, P. Chowdhury, D. Cline, H. L. Crawford, P. Fallon, A. M. Forney, A. Gade, A. B. Hayes, F. G. Kondev, Krishichayan, T. Lauritsen, J. Li, A. O. Macchiavelli, D. Rhodes, D. Seweryniak, S. M. Stolze, W. B. Walters, and J. Wu. Evidence for rigid triaxial deformation in ^{76}Ge from a model-independent analysis. *Phys. Rev. Lett.*, 123: 102501, 2019.

[36] Y. Toh, C. J. Chiara, E. A. McCutchan, W. B. Walters, R. V. F. Janssens, M. P. Carpenter, S. Zhu, R. Broda, B. Fornal, B. P. Kay, F. G. Kondev, W. Królas, T. Lauritsen, C. J. Lister, T. Pawłat, D. Seweryniak, I. Stefanescu, N. J. Stone, J. Wrzesiński, K. Higashiyama, and N. Yoshinaga. Evidence for rigid triaxial deformation at low energy in ^{76}ge. *Phys. Rev. C*, 87:041304, 2013.

[37] P.J. Ennis, C.J. Lister, W. Gelletly, H.G. Price, B.J. Varley, P.A. Butler, T. Hoare, S. Ćwiok, and W. Nazarewicz. Triaxiality and isospin-forbidden e1 decays in the n = z nucleus 64ge. *Nuclear Physics A*, 535(2):392–424, 1991.

[38] A. Obertelli, T. Baugher, D. Bazin, J. P. Delaroche, F. Flavigny, A. Gade, M. Girod, T. Glasmacher, A. Goergen, G. F. Grinyer, W. Korten, J. Ljungvall, S. McDaniel, A. Ratkiewicz, B. Sulignano, and D. Weisshaar. Shape evolution in self-conjugate nuclei, and the transitional nucleus ^{68}Se. *Phys. Rev. C*, 80:031304, 2009.

[39] Lawrence Wilets and Maurice Jean. Surface oscillations in even-even nuclei. *Phys. Rev.*, 102:788–796, 1956.

[40] D. J. Rowe, T. A. Welsh, and M. A. Caprio. Bohr model as an algebraic collective model. *Phys. Rev. C*, 79:054304, 2009.

[41] K. E. G. Löbner. Gamma-Ray Transition Probabilities in Deformed Nuclei. In L. Becker, Richard, C. D. Goodman, P. H. Stelson, and A. Zucker, editors, *International Nuclear Physics Conference*, page 406, January 1967.

[42] Y. Tokunaga, H. Seyfarth, O. W. B. Schult, H. G. Börner, Ch. Hofmeyr, G. Barreau, R. Brissot, U. Kaup, and Ch. Mönkemeyer. The ^{75}Se(n, γ)^{76}Se reaction and the low-lying level structure of ^{76}Se. *Nuclear Physics A*, 411(2):209 – 230, 1983.

[43] H. Dejbakhsh, T.M. Cormier, X. Zhao, A. V. Ramayya, L. Chaturvedi, S. Zhu, J. Kormicki, J. H. Hamilton, M. Satteson, I. Y. Lee, C. Baktash, F. K. McGowan, N. R. Johnson, J. D. Cole, and E. F. Zganjar. Signature of the shape coexistence in ^{72}Kr: discontinuities of the moment of inertia at low spin. *Physics Letters B*, 249 (2):195 – 199, 1990.

[44] D. M. Moltz, J. D. Robertson, E. B. Norman, J. Burde, and C. W. Beausang. Low-lying level structure of ^{73}Kr. *Nuclear Physics A*, 562(1):111 – 120, 1993.

[45] F. Becker, A. Petrovici, J. Iwanicki, N. Amzal, W. Korten, K. Hauschild, A. Hurstel, Ch. Theisen, P.A. Butler, R.A. Cunningham, T. Czosnyka, G. de France, J. Gerl, P. Greenlees, K. Helariutta, R.-D. Herzberg, P. Jones, R. Julin, S. Juutinen, H. Kankaanpää, M. Muikku, P. Nieminen, O. Radu, P. Rahkila, and Ch. Schlegel. Coulomb excitation of ^{78}Kr. *Nuclear Physics A*, 770(3):107 – 125, 2006.

[46] A. de Shalit and M. Goldhaber. Mixed Configurations in Nuclei. *Physics Review*, 92:1211–1218, 1953.

[47] R. Wadsworth, L. P. Ekstrom, G. D. Jones, F. Kearns, T. P. Morrison, O. M. Mustaffa, H. G. Price, P. J. Twin, and N. J. Ward. A study of the neutron-deficient isotope ^{66}Ge. *Journal of Physics G: Nuclear Physics*, 5(12):1761–1774, dec 1979.

[48] R. Lüttke, E. A. McCutchan, V. Werner, K. Aleksandrova, S. Atwater, H. Ai, R. J. Casperson, R. F. Casten, A. Heinz, A. F. Mertzand, J. Qian, B. Shoraka, J. R. Terry, E. Williams, and R. Winkler. Collectivity in ^{66}Ge and ^{68}Ge via lifetime measurements. *Physics Review C*, 85:017301, 2012.

[49] A. Corsi, J.-P. Delaroche, A. Obertelli, T. Baugher, D. Bazin, S. Boissinot, F. Flavigny, A. Gade, M. Girod, T. Glasmacher, G. F. Grinyer, W. Korten, J. Libert, J. Ljungvall, S. McDaniel, A. Ratkiewicz, A. Signoracci, R. Stroberg, B. Sulignano,

and D. Weisshaar. Collectivity of light Ge and As isotopes. *Physics Review C*, 88: 044311, 2013.

[50] B. Pritychenko, M. Birch, B. Singh, and M. Horoi. Tables of E2 transition probabilities from the first 2^+ states in even–even nuclei. *Atomic Data and Nuclear Data Tables*, 107:1 – 139, 2016.

[51] K. Alder, A. Bohr, T. Huus, B. Mottelson, and A. Winther. Study of Nuclear Structure by Electromagnetic Excitation with Accelerated Ions. *Reviews of Modern Physics*, 28:432–542, 1956.

[52] L. Biedenharn and P. Brussaard. *Coulomb Excitation.* Clarendon Press, Oxford Library of Physical Science, 1965.

[53] D. Cline. Nuclear Shapes Studied by Coulomb Excitation. *Annual Review of Nuclear and Particle Science*, 36:683–716, 1986.

[54] W. Nörenberg and H.A. Weidenmüller. *Introduction to the Theory of Heavy-Ion Collisions.* Springer-Verlag, Berlin Heidelberg GmbH, 1976.

[55] A. Winther and J. de Boer. A Computer Program for Multiple Coulomb Excitation. *Perspectives in Physics*, 19:303–374, 1966.

[56] D. Cline, T. Czosnyka, A.B. Hayes, P. Napiorkowski, N. Warr, and C.Y. Wu. *GOSIA User Manual for Simulation and Analysis of Coulomb Excitation Experiments.* GOSIA Steering Committee, 2012.

[57] J.F. Ziegler, J.P. Biersack, and M.D. Ziegler. SRIM – The stopping and range of ions in matter. *Nuclear Instruments and Methods in Physics Research B*, 268: 1818–1823, 2010.

[58] E. Kugler. The ISOLDE facility. *Hyperfine Interactions*, 129:23–42, 2000.

[59] A. Gustafsson, A. Herlert, and F. Wenander. Mass-selective operation with REX-TRAP. *Nuclear Instruments Methods in Physics, Research section A: Accelerators, Spectrometers, Detectors and Associated Equipment*, 626:8–15, 2011.

[60] F. Wenander, B. Jonson, L. Liljeby, and G.H. Nyman. REXEBIS the Electron Beam Ion Source for the REX-ISOLDE project. Technical Report CERN-OPEN-2000-320, CERN, Geneva, 1998. URL https://cds.cern.ch/record/478399.

[61] Y. Kadi, Y. Blumenfeld, W. Venturini Delsolaro, M. A. Fraser, M. Huyse, A. Papageorgiou Koufidou, J. A. Rodriguez, and F. Wenander. Post-accelerated beams at ISOLDE. *Journal of Physics G: Nuclear and Particle Physics*, 44(8), 2017.

[62] R. von Hahn, M. Grieser, D. Habs, E. Jaeschke, C.M. Kleffner, J. Liebmann, S. Papureanu, R. Repnow, D. Schwalm, and M. Stampfer. Development of seven-gap resonators for the Heidelberg high current injector. *Nuclear Instruments and Methods in Physics, Research section A: Accelerators, Spectrometers, Detectors and Associated Equipment*, 328:270–274, 1993.

[63] A. N. Ostrowskia, S. Cherubinib, T. Davinsona, D. Groombridgea, A. M. Lairda, A. Musumarrab, A. Ninaneb, A. di Pietroa, A. C. Shottera, and P. J. Woodsa. CD: A double sided silicon strip detector for radioactive nuclear beam experiments. *Nuclear Instruments and Methods in Physics Research A*, 480:448–455, 2002.

[64] R. Brun and F. Rademakers. ROOT – An object oriented data analysis framework. *Nuclear Instruments and Methods in Physics Research A*, 389(1):81, 1997.

[65] D. C. Radford. Notes on the use of the program gf3. Available: https://radware.phy.ornl.gov/gf3/.

[66] D. Bazin, O. Tarasov, M. Lewitowics, and O. Sorlin. The Program LISE: A Simulation of Fragment Separators. *Nuclear Instruments and Methods in Physics, Research section A: Accelerators, Spectrometers, Detectors and Associated Equipment*, 482: 307–327, 2002.

[67] C.S. Lim, R.H. Spear, M.P. Fewell, and G.J. Gyapong. Measurements of static electric quadrupole moments of the 2+1, 2+2, 4+1 and 6+1 states of 196pt. *Nuclear Physics A*, 548(2):308–330, 1992.

[68] A. Mauthofer, K. Stelzer, J. Idzko, Th. W. Elze, H. J. Wollersheim, H. Emling, P. Fuchs, E. Grosse, and D. Schwalm. Triaxiality and γ-softness in^{196}Pt. *Zeitschrift fur Physik A Hadrons and Nuclei*, 336(3):263–278, 1990.

[69] E. Tavukcu, L. A. Bernstein, K. Hauschild, J. A. Becker, P. E. Garrett, C. A. McGrath, D. P. McNabb, W. Younes, M. B. Chadwick, R. O. Nelson, G. D. Johns, and G. E. Mitchell. ^{196}Pt$(n, xny p\gamma)$ reactions using spallation neutrons from $E_n = 1$ to 250 mev. *Phys. Rev. C*, 64:054614, 2001.

[70] M. Kumar Raju, J.N. Orce, P. Navrátil, G.C. Ball, T.E. Drake, S. Triambak, G. Hackman, C.J. Pearson, K.J. Abrahams, E.H. Akakpo, H. Al Falou, R. Churchman, D.S. Cross, M.K. Djongolov, N. Erasmus, P. Finlay, A.B. Garnsworthy, P.E. Garrett, D.G. Jenkins, R. Kshetri, K.G. Leach, S. Masango, D.L. Mavela, C.V. Mehl, M.J. Mokgolobotho, C. Ngwetsheni, G.G. O'Neill, E.T. Rand, S.K.L. Sjue, C.S. Sumithrarachchi, C.E. Svensson, E.R. Tardiff, S.J. Williams, and J. Wong. Reorientation-effect measurement of the first 2^+ state in ^{12}C: Confirmation of oblate deformation. *Physics Letters B*, 777:250 – 254, 2018.

[71] J. N. Orce, T. E. Drake, M. K. Djongolov, P. Navrátil, S. Triambak, G. C. Ball, H. Al Falou, R. Churchman, D. S. Cross, P. Finlay, C. Forssén, A. B. Garnsworthy, P. E. Garrett, G. Hackman, A. B. Hayes, R. Kshetri, J. Lassen, K. G. Leach, R. Li, J. Meissner, C. J. Pearson, E. T. Rand, F. Sarazin, S. K. L. Sjue, M. A. Stoyer, C. S. Sumithrarachchi, C. E. Svensson, E. R. Tardiff, A. Teigelhoefer, S. J. Williams, J. Wong, and C. Y. Wu. Reorientation-effect measurement of the $\langle 2_1^+ \, \|\hat{E2}\| \, 2_1^+ \rangle$ matrix element in ^{10}Be. *Physics Review C*, 86:041303, 2012.

[72] J. Van de Walle, F. Aksouh, T. Behrens, V. Bildstein, A. Blazhev, J. Cederkäll, E. Clément, T. E. Cocolios, T. Davinson, P. Delahaye, J. Eberth, A. Ekström, D. V. Fedorov, V. N. Fedosseev, L. M. Fraile, S. Franchoo, R. Gernhauser, G. Georgiev, D. Habs, K. Heyde, G. Huber, M. Huyse, F. Ibrahim, O. Ivanov, J. Iwanicki, J. Jolie, O. Kester, U. Köster, T. Kröll, R. Krücken, M. Lauer, A. F. Lisetskiy, R. Lutter, B. A. Marsh, P. Mayet, O. Niedermaier, M. Pantea, R. Raabe, P. Reiter, M. Sawicka, H. Scheit, G. Schrieder, D. Schwalm, M. D. Seliverstov, T. Sieber, G. Sletten, N. Smirnova, M. Stanoiu, I. Stefanescu, J.-C. Thomas, J. J. Valiente-Dobón, P. Van Duppen, D. Verney, D. Voulot, N. Warr, D. Weisshaar, F. Wenander, B. H. Wolf, and M. Zielińska. Low-energy coulomb excitation of neutron-rich zinc isotopes. *Phys. Rev. C*, 79:014309, 2009.

[73] N. Kesteloot, B. Bastin, L. P. Gaffney, K. Wrzosek-Lipska, K. Auranen, C. Bauer, M. Bender, V. Bildstein, A. Blazhev, S. Bönig, N. Bree, E. Clément, T. E. Cocolios, A. Damyanova, I. Darby, H. De Witte, D. Di Julio, J. Diriken, C. Fransen, J. E. García-Ramos, R. Gernhäuser, T. Grahn, P.-H. Heenen, H. Hess, K. Heyde, M. Huyse, J. Iwanicki, U. Jakobsson, J. Konki, T. Kröll, B. Laurent, N. Lecesne, R. Lutter, J. Pakarinen, P. Peura, E. Piselli, L. Próchniak, P. Rahkila, E. Rapisarda, P. Reiter, M. Scheck, M. Seidlitz, M. Sferrazza, B. Siebeck, M. Sjodin, H. Tornqvist, E. Traykov, J. Van De Walle, P. Van Duppen, M. Vermeulen, D. Voulot, N. Warr, F. Wenander, K. Wimmer, and M. Zielińska. Deformation and mixing of coexisting shapes in neutron-deficient polonium isotopes. *Phys. Rev. C*, 92:054301, 2015.

[74] C. Lebrun, F. Guilbault, D. Ardouin, E. R. Flynn, D. L. Hanson, S. D. Orbesen, R. Rotbard, and M. N. Vergnes. Ge-72, Ge-74, Ge-76 by the (t, p) reaction. *Physics Review C*, 19:1224–1235, 1979. doi: 10.1103/PhysRevC.19.1224.

[75] Kazunari Kaneko, M. Hasegawa, and T. Mizusaki. Oblate-prolate coexistence in 68se. 831, 04 2006.

[76] K. Nomura, R. Rodríguez-Guzmán, and L. M. Robledo. Structural evolution in germanium and selenium nuclei within the mapped interacting boson model based on the gogny energy density functional. *Phys. Rev. C*, 95:064310, 2017.

[77] M. Rocchini, K. Hadyńska-Klęk, A. Nannini, A. Goasduff, M. Zielińska, D. Testov, T. R. Rodríguez, A. Gargano, F. Nowacki, G. De Gregorio, H. Naïdja, P. Sona, J. J. Valiente-Dobón, D. Mengoni, P. R. John, D. Bazzacco, G. Benzoni, A. Boso, P. Cocconi, M. Chiari, D. T. Doherty, F. Galtarossa, G. Jaworski, M. Komorowska, N. Marchini, M. Matejska-Minda, B. Melon, R. Menegazzo, P. J. Napiorkowski, D. Napoli, M. Ottanelli, A. Perego, L. Ramina, M. Rampazzo, F. Recchia, S. Riccetto, D. Rosso, and M. Siciliano. Onset of triaxial deformation in ^{66}Zn and properties of its first excited 0^+ state studied by means of coulomb excitation. *Phys. Rev. C*, 103:014311, 2021.

[78] M. Hasegawa, T. Mizusaki, K. Kaneko, and Y. Sun. Enhancement of B(E2)↑ and low excitation of the second 0^+ state near $N = 40$ in Ge isotopes. *Nuclear Physics A*, 789(1):46 – 54, 2007.

[79] J. F. Berger, M. Girod, and D. Gogny. Time-dependent quantum collective dynamics applied to nuclear fission. *Computer Physics Communications*, 63(1):365 – 374, 1991.

[80] J. Libert, J.-P. Delaroche, M. Girod, H. Goutte, S. Hilaire, S. Péru, N. Pillet, and G. F. Bertsch. Microscopic study of low energy collective states in even-even nuclei: A prospective analysis of dynamical corrections to vibrational mass parameters. *Journal of Physics: Conference Series*, 205:012007, 2010.

[81] T. R. Rodríguez. Structure of krypton isotopes calculated with symmetry-conserving configuration-mixing methods. *Physics Review C*, 90:034306, 2014.

[82] T. R. Rodríguez. ^{66}Ge first 2^+ state. private communication, 28 October 2020.